UNIVERSITÀ DI PARMA

UNIVERSITA' DEGLI STUDI DI PARMA

DOTTORATO DI RICERCA IN
Scienza e Tecnologia dei Materiali

CICLO XXXV

SURFACE-CONFINED CHEMISTRY OF HALOGENATED AROMATIC COMPOUNDS ON AG(110): SELF-ASSEMBLY AND POLYERIZATION

Coordinatore:
Chiar.mo Prof. Enrico Dalcanale

Tutore:
Dott.ssa Letizia Savio

Dottorando: Jose Eduardo A. Barcelon

Anni Accademici 2019/2020 – 2021/2022

ABSTRACT

Carbon-based nanostructures have been extensively studied over the years due to the interesting electronic, mechanical, and thermal properties of low dimension C-allotropes. Among this class of molecules, graphene derivatives have attracted particular attention due to the combination of excellent ballistic transport and structure-dependent properties. E.g., confinement in 1D leads to bad gap opening and edge effects. Therefore, it is possible to modify graphene to tune its properties for appropriate applications. Another way to modify the properties of C-based nanostructures is to couple them with either heteroatoms or transition metal (TM) atoms. Introduction of such dopants allows for the tuning of the electronic and chemical properties of the nanostructures. Cyclometallated complexes on surfaces, for example, could lead to the realization of a promising class of C-based nanostructures.

Several methods have been explored to grow these materials. Among them, bottom-up approaches exploiting the surface assisted synthesis of nanostructures from precursor molecules self-assembled and subsequently polymerized by Ullmann coupling was found to produce better ordered and uniform 1D/2D nanostructures.

In this dissertation, I present my work on the synthesis and characterization of different C-based nanostructures and self-assemblies supported on Ag(110). The experiments are performed under UHV conditions and the samples are characterized by LT-STM and XPS. High resolution XPS and NEXAFS data acquired at the Aloisa beamline of ELETTRA synchrotron radiation source and theoretical models based in DFT calculations performed by partners in UNIMIB complement my analysis to provide a complete description of the systems.

I will first describe my investigation of achiral GNRs synthesized from 1,6-dibromopyrene. Specifically, I will report on the stability of these GNRs showing that they react when exposed to oxygen under controlled conditions and that the morphology of the surface changes considerably under exposure. Furthermore, Ag-O complexes appear on the surface and in between the GNRs, effectively enlarging the gap between ribbons.

Then, I will discuss the interaction of the Pd cyclometallated complex [(5-bromo-2-phenylpyridine)Pd(μ-Cl)]$_2$ with Ag(110). I underline that these molecules are of large use in catalysis but their interaction with metal surfaces has not been explored so far. I found an unexpected chemistry induced by the interaction with Ag(110). Indeed, my data suggests the fragmentation of the molecule and, with the right conditions, cross coupling to form a new compound. More information can be retrieved from comparison between the behaviour of the brominated and hydrogenated versions of the same compound.

gli acronimi non sono definiti

1 TABLE OF CONTENTS

LIST OF ACRONYMS

1D	1-Dimensional
2D	2-Dimensional
AGNRs	Armchair graphene nanoribbons
Ar-X	Aromatic Halides
BR-STM	Bond-resolved scanning tunnelling microscopy
CN-chGNRs	Cyano-(chiral) graphene nanoribbons
CNTs	Carbon Nanotubes
CyPd	Cyclometallated Palladium complex (dibrominated)
CyPd_2	Cyclometallated Palladium complex
DBBA	10,10′ -dibromo-9,9′ -bianthracene
DBP	1,6-Dibromopyrene
DBT	Dibromotetracene
FETs	Field Effect Transistors
GNRs	Graphene Nanoribbons
GO	Graphene Oxide
LHe	Liquid Helium
LN_2	Liquid Nitrogen
LT-STM	Low Temperature Scanning Tunnelling Microscopy
ML	Monolayer
NEXAFS	Near-Edge X-ray Adsorption Fine Structure Spectroscopy
QMS	Quadropole Mass Spectrometer
STS	Scanning Tunnelling Spectroscopy
TSP	Titanium Sublimation Pump
XPS	X-ray Photoemission Spectroscopy

2 INTRODUCTION AND STATE OF THE ART

Carbon allotropes are a particularly interesting and thoroughly studied class of materials in a variety of fields like chemistry, materials science, and engineering. Allotropes like graphene, carbon nanotubes, nanoribbons, "bucky balls," etc... have properties that directly depend on their size, shape, and functionalization. Graphene is one of the most popular carbon allotropes; it consists of a single layer of sp^2 hybridized carbon atoms in a honeycomb lattice and it possesses mechanical, electronic, and optical properties that make it a promising material for several applications. Some of these properties include high intrinsic charge mobility, high electrical and thermal conductivity, high optical transparency, and high tensile strength. However, while some of these properties (including excellent ballistic transport of charge carriers) make graphene suitable for devices where high electrical conductivity is needed (e.g., electrodes), the absence of an electronic band gap prevents its use in nanoelectronics, for which a semiconducting behaviour is required.

For this reason, the attention moved to low-dimensional carbon-based nanostructures such as carbon nanotubes and graphene nanoribbons (GNRs). GNRs, as the name implies, are graphene-like, one-dimensional (1D) nanostructures narrower than 10 nm. [1–5] They are of particular interest because the quantum confinement of the electrons and the presence of different edge geometries (with possible associated electronic states) cause a bandgap opening, while still retaining the ballistic transport of charge carriers.

Another possibility to modify the properties of C-based nanostructures and many carbon allotropes in general is to couple the carbon-based species with other atoms. It is well-established that C-based nanostructures can be doped with hetero-atoms to tune their electronic and chemical properties [6]. Most studies concern doping carbon nanostructures with non-metal atoms (e.g., N, P, S, B). The introduction of transition metal (TM) atoms in the carbon network could be even more interesting, since TM containing C-networks are predicted to have interesting electronic and catalytic properties. Organometallic compounds, particularly complexes of the group 10 elements in solution, are already popular due to their widespread use in numerous applications such as catalytic synthetic processes [7–9], biochemistry [10–12] and materials science [13,14]. For example, many palladium complexes have been extensively studied as catalysts in several cross-coupling reactions [15,16]. While advancements have been made on the synthesis of transition metal (TM) complexes with specific properties, our understanding about their interactions with surfaces especially on metals is still limited. However, their coupling to a surface is challenging, since it could lead to a breakthrough in catalysis and sensoristics. These new and low-cost materials could, in principle, replace currently used catalysts based on precious transition metals, with interesting applications in sensoristics and nanocatalysis.

Multiple methods were developed to synthesize C-based nanostructures. GNRs, for example, can be synthesized using several top-down methods, which include sonication,[1] lithography[17] and unzipping of carbon nanotubes (CNTs).[18,19] These approaches allow for a relatively easy production of graphenic, low dimensional nanostructures. However, these products often have a relatively poor quality in terms of uniformity and defectivity at the edges. Since regularity of shape and size is required for a variety of applications, and in particular for nanoelectronics, an alternative on-surface bottom-up approach appears more promising. [20–23] It usually exploits the surface

assisted polymerization of a molecular precursor (often a halogenated aromatic compound) catalyzed by a metal surface. The process occurs in two steps since the so-called Ullman-coupling reaction is followed by cyclodehydrogenation and formation of new C-C bonds. [24–27] One of the first precursor molecules to be successfully employed specifically to synthesize GNRs was 10,10′-dibromo-9,9′-bianthracene (DBBA). DBBA polymerizes forming N=7 GNRs with armchair edges.[22] Eventually, a wide variety of halogenated and non-halogenated aromatic hydrocarbons [28,29] has been employed to synthesize GNRs with well-defined width and edge sites, either armchair, zig-zag,[30] mixed[23] or cove.[28] Chiral GNRs could also be produced starting from DBBA on Cu(111).[21]

Forming C nanostructures with an on-surface bottom-up approach does come with peculiarities. The final product is dependent on several factors, including the nature and geometry of the metallic substrate [22,31,32] and the structure of the precursor molecule.[21–23,28,33–35] The choice of the proper compound is essential, since not all possible candidates are suitable and/or stable enough on the surface to allow for the dehydrogenation and C-C coupling processes leading to the formation of extended graphenic nanostructures. Polymerization occurs via C-C coupling, with or without the formation of organometallic intermediates involving substrate atoms. In a common situation, the reactants present a C-halogen bond, which breaks at the metal surface. The unsaturated C atom can form either an organometallic intermediate with a metal atom of the surface (Ullmann coupling) or directly a new C-C bond with another dissociated precursor molecule, while the dissociated halogen atom binds to the surface. As an example, we mention the case of 1,5 di-bromo-tetracene (DBT) and 1,6 di-bromo-pyrene (DBP), two halogenated aromatic hydrocarbons with similar molecular weight and different geometry. We previously produced ordered arrays of GNRs on Ag(110) from DBP polymerization,[23] while desorption prevails for DBT on the same substrate.[36] On the other hand, the use of Br-corannulene on Ag(110) leads to the formation of C-based dimers which do not have the spectroscopic signature of graphene because of the non-planar geometry of the precursor molecule.[35] Indeed, with respect to chemical reactions in solution, the process can lead to different reaction steps, and possibly to different reaction products, due to 2D confinement and to the active role of the substrate.

My research enters this field since it involves the study of GNRs and metal-doped C-based layers supported on Ag(110).

In my first year, I investigated the stability of graphene nanoribbons synthesized from 1,6-dibromopyrene (1,6 DBP). The growth protocol was already well established by the research group. I started by characterizing these nanoribbons in terms of their morphology and electronic structure as well as their interaction with oxygen.[37] The possible chemical activity of these GNRs is important because of the potential applications of these GNRs, that need to be stable under operative conditions. While it is expected for our GNRs to be chemically inert due to the saturation of all edge sites with hydrogen, studies suggest that some edge site configurations, such as zigzag edges, can still be prone to attack by reactive species such as oxygen [38]. In addition, it should be possible to transfer GNRs from the native metal substrate to the suitable substrate for the desired application. Usually, they can be successfully transferred using techniques similar to those employed for graphene films but, if the nanostructures are produced under ultra-high vacuum (UHV) conditions, this implies exposure to

ambient pressure and to liquid solvents.[39] For 7- and 9-AGNRs, the transfer process does not modify the characteristics of the nanostructures. On the contrary, bottom-up synthesis of 7-AGNRs under less stringent vacuum conditions ($P=10^{-6}$ mbar)[40] is deeply affected by the presence of a residual partial pressure of water and oxygen. A detailed understanding of these processes is lacking but it is necessary to determine the structure and electronic properties of the nanoribbons after transfer onto the desired substrate and how these properties are affected by the substrate change. For the GNRs mentioned in this dissertation, I report on the effect of oxygen exposure on the GNRs as seen using scanning tunnelling microscopy (STM) and X-ray Photoemission Spectroscopy (XPS). The effects include an increase in the spacing between adjacent GNRs but also a partial modification of the Ag(110) substrate with the formation of Ag-O complexes and evidence of oxygen reacting with the GNRs along the edge sites.[37]

In a second step, I investigated the possibility to form extended carbon networks involving organometallic complexes. As precursor, I used a palladium cyclometallated complex, [(5-bromo-2-phenylpyridine)Pd(μ-Cl)]$_2$ (CyPd in the following), which I deposited on Ag(110). As mentioned earlier, the interaction of TM complexes with surfaces hasn't been extensively explored so far. 2D networks doped with TM atoms could be made by the reaction of suitable precursors on nanoporous carbon materials, which were then demonstrated to be efficient towards the oxygen oxidation reaction, for example [41]. Similarly, Pd(II)-based 2D mesoporous covalent organic frameworks have been recently synthesized and successfully employed as eco-friendly heterogeneous photocatalysts for CO_2 cycloaddition [42]. Much less experimental information is available for supported 2D and 1D nanostructures. TM atoms could be inserted *a posteriori* once the C-layer has already been produced. However, due to their high surface energy, they can be unstable and cluster together. Alternatively, TM atoms can be introduced in the network during its formation using suitable organometallic precursors. In this case, stabilization of the TM is achieved via the presence of other non-metallic elements, such as nitrogen (e.g. by N-TM-C bonds). Theoretical models of such hybrid metal/non-metal/carbon networks suggest promising results, while the development of such systems and their understanding at the fundamental level (including a detailed characterization of their morphological, electronic, and chemical properties) is still lacking.

To the best of my knowledge, I deposited a Pd cyclometallated compound on a metal substrate for the first time. The idea is to potentially observe the formation of uniform and extended self-assemblies because of the interaction between the molecules and the substrate. The dinuclear Pd complex was chosen for its planar structure and its high thermal stability, besides bearing two metal atoms/molecule. The organic ligand was brominated, aiming at a surface-assisted organization, as we previously observed for bromoarenes [23,43]. Since, as mentioned before, there is no previous literature on this topic, I focused my attention on the stability of the compound upon adsorption and on the change in molecular conformation, with the aim of evaluating if the system can be suitable as a model for catalytic studies.

I characterized the **CyPd**/Ag(110) system upon deposition of the molecules at room temperature (RT) and subsequent annealing up to 500°C by combining the morphological information provided by scanning tunnelling microscopy (STM) with the chemical one derived from X-ray photoemission spectroscopy (XPS) measurements. Based on density functional theory (DFT) calculations done by

our collaborators in UNIMIB, I propose a reaction mechanism and an adsorption model, which are then validated by simulated STM images and by a Near Edge Adsorption Fine Structure (NEXAFS) analysis. Results indicate a complex chemistry at the surface: the Ag surface promotes dissociation of **CyPd** in two phenyl-pyridine (phe-pyr) fragments. Each fragment is coordinated by an Ag adatom provided by the substrate, thus forming a network of organometallic compounds, while the Pd atoms migrate in the subsurface region. The dissociated halogen atoms are stabilized on the surface by Ag atoms. The final configuration is more complex than expected, giving rise to two very distinct systems for sub and full monolayer coverage of CyPd on Ag(110). This difference depends, most likely, on the adsorption kinetics, i.e. on the sublimation rate of the molecules. A full monolayer of CyPd molecules resulted in the formation of diphenyl-bipyridine units upon heating along with extensive surface reconstruction, while an ordered arrrangment of Phe-Pyr units saturated on Ag(110) is observed at sub-ML coverage.

I also included here studying CyPd on Ag(110) deposited at cryogenic temperatures as well as studying unbrominated CyPd ([(2-phenylpyridine)Pd(μ-Cl)]$_2$ or CyPd_2) and reporting on features in comparison with CyPd. The results I mention here give a deeper understanding of the chemistry between metal surfaces and Pd cyclometallated complexes and elucidate the electronic and chemical properties of this class of materials.

Finally, I end my dissertation with a brief mention of the work I did at the Centro de Fisica de Materiales in Donostia-San Sebastian, Spain, during my 10 weeks internship. The project was about the characterization of Co-coordinated cyano-functionalized chiral GNRs (Co+CN-chGNRs) on Au(111) and their reactivity with oxygen. The motivation behind the study is to determine the viability of using TM-coordinated GNRs in sensoristics. Characterization of the as synthesized GNRs and the same GNRs after oxygen exposure were also done using LT-STM and STS under UHV conditions like in my own projects mentioned earlier. The inclusion of the work we performed in Spain is very much warranted here because it is in line with the rest of the studies I have conducted on C-based nanostructures and fit the theme of my dissertation on the chemistry of such 2D systems.

3 EXPERIMENTAL METHODS

3.1 ULTRA-HIGH VACUUM (UHV) SYSTEMS OVERVIEW

All the apparatuses I used to conduct my experiments are housed in ultra-high vacuum chambers that are maintained at a pressure better than $2x10^{-9}$ mbar by using a variety of pumps. I worked with a UHV chamber that houses a low temperature scanning tunnelling microscope (LT-STM) and with another that houses an X-ray photoemission spectroscopy (XPS) system. Both chambers also contain the necessary tools and equipment for in *situ* manipulation, cleaning, and preparation of the sample (e.g., deposition of molecules, exposure to gases).

The LT-STM setup is schematically represented in Figure 1. The STM is manufactured by Createc. It can be separated into discrete sections by gate valves (marked by "X"), in order to perform sample preparation or insertion from the fast entry lock without affecting the rest of the system. A more detailed discussion of the LT-STM setup can be found in the next sections.

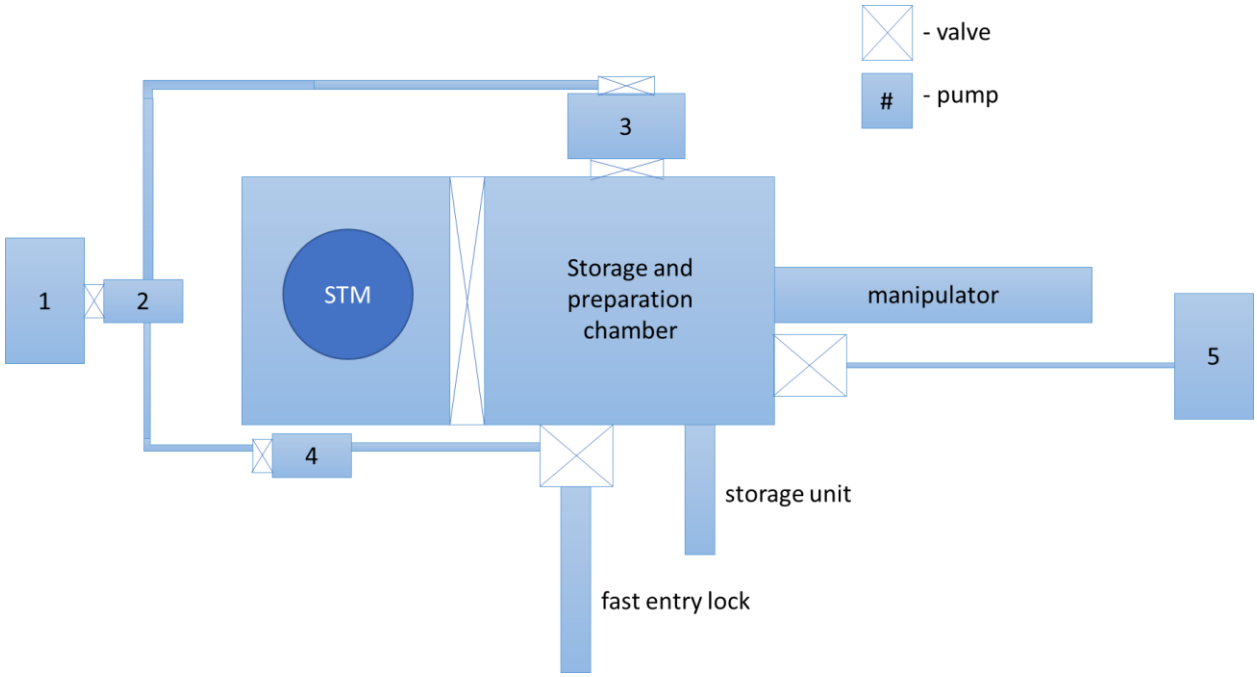

Figure 1. Schematic of the LT-STM chamber (Createc)- Top view.

The schematic of the XPS apparatus is shown in Figure 2.

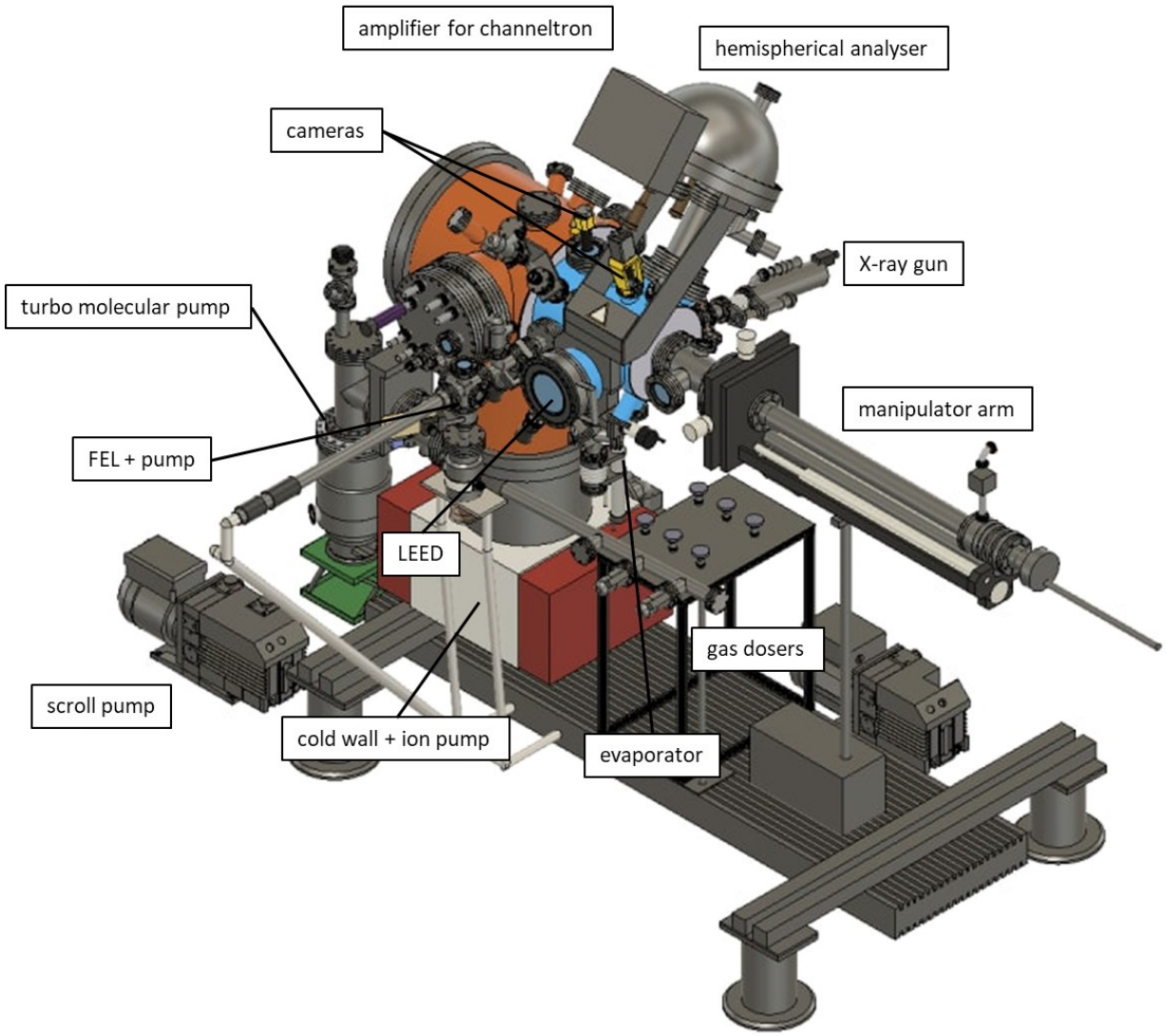

Figure 2. Schematic of the XPS chamber (Omicron) created in AutoCAD (c/o Simone Passaglia and Giovanni Carraro)

In the next section, I will explain ultra-high vacuum conditions and how to achieve them before discussing each experimental chambers (LT-STM, XPS) in more detail.

3.1.1 Ultra-high vacuum (UHV)

The tools and techniques that I need to conduct experiments in both the LT-STM and XPS chambers require the system to be in ultra-high vacuum to function properly and produce data reliably. UHV is defined as the pressure range from 10^{-7} to 10^{-12} mbar. This level of vacuum is achieved using a series of pumps. UHV makes it possible to do experiments that probe molecule-surface interactions like STM and XPS without the interference of other molecules in the atmosphere, that could impinge on and contaminate the surface. The level of vacuum or residual pressure inside the chamber determines the amount of time that a sample could stay relatively free of contaminants and therefore the length of any given experiment. For instance, one can derive the flux of particles on a surface defined by the number of collisions per unit area per unit time given the pressure, temperature, and mass of the gas particles in the chamber. This flux is described by the Hertz-Knudsen equation:

$$F = \frac{1}{4} n\bar{c} = \frac{P}{\sqrt{2\pi m k T}} \left[\frac{molecules}{m^2 \cdot s}\right]$$

where $n = \frac{N}{V} = \frac{P}{kT}$ is the molecular gas density, $\bar{c} = \sqrt{\frac{8kT}{m\pi}}$ is the molecular mean velocity coming from the Maxwell-Boltzmann distribution, m is the molecular mass, P is the partial pressure in the gas phase, T is the gas temperature, and k is Boltzmann's constant (k = 1.38 x 10^{-23} J/K). Using this equation, one can make an approximation of how much time the sample stays clean. For example, carbon monoxide (CO) is always present in trace quantities in the vacuum chamber, likely from the chamber walls. CO flux is $2.88 \cdot 10^{15} \frac{molecules}{m^2 \cdot s}$ when the residual pressure of the chamber is at $P = 1 \cdot 10^{-9} mbar$. Since the atomic surface density of Ag(110) $is\ 8.46 \cdot 10^{18} \frac{atoms}{m^2}$), this means that, on average, each surface unit cell of Ag(110) gets hit by a CO molecule once every hour. If CO had a sticking probability of 1, then the whole sample would be covered by a monolayer of CO in 1 hour. Therefore, it is important to maintain as high a vacuum as possible to produce reliably clean samples for instruments like STM and XPS.

Another reason for using UHV is the need to employ electron/ion/particle-based techniques, such as XPS. In this case, charged particles must have a mean free path long enough to run the distance between the source and the target/detector (i.e., tens of cm) without scattering against molecules of the atmosphere and getting absorbed. This is especially important for cleaning samples by sputtering ions or for collecting photoemission electrons coming from a sample.

3.1.2 Pumping systems

The combination of vacuum pumps (mechanical, chemical, etc.) utilized by both chambers (LT-STM and XPS) is optimized to achieve and maintain UHV. In the LT-STM chamber as seen in the scheme of Figure 1, initial vacuum is produced by a scroll pump (1) (Varian, pumping speed 4.2 m^3/h). Then ultra high vacuum is achieved using a molecular pump (2) (Alcatel 7.5 L/s) and a turbomolecular pump (3) (Leybold 330 L/s) connected directly to the preparation chamber. At this stage, the pressure inside the preparation chamber should reach $1 \cdot 10^{-9}$ mbar after a bake out. There is also a turbomolecular pump (4) (Agilent 70 L/s) connected to the fast entry lock (FEL), that is connected in parallel to (3). (4) is used to pump the side chamber for inserting items into the preparation chamber and to purge all the gas lines. Besides the mechanical pumps, the preparation chamber also houses an ion pump, a titanium sublimation pump, and a cryogenic panel (or cold trap) contained in (5) (see Figure 1). Since this section contains only capture pumps, which operate exclusively in the UHV regime, can be manually isolated from the rest of the chamber with a gate valve whenever the pressure in the preparation chamber needs to be increased above $5 \cdot 10^{-8}$ mbar. The pumps located in (5) are necessary to reach and maintain ultra-high vacuum (UHV) conditions in the chamber especially during STM measurements, when all mechanical pumps must be switched off.

The XPS chamber operates in a similar fashion as the STM chamber albeit without the internal separation between preparation and analysis chamber. Pumping the chamber to UHV also begins with a rotary pump (Leybold 25 m^3/h). UHV is achieved by a single turbomolecular pump (Varian 550 L/s). An additional small turbomolecular pump (Elettrorava 54 L/s) is used to pump the FEL and to purge the gas lines.

Describing the process to achieve UHV in more detail, one always starts with a rough pump (a scroll pump in my case). A scroll pump operates by compressing air between two interlocking scrolls (one stationary and one rotating) forcing the air out. This allows to lower the chamber pressure down to ~

10^{-2} mbar (medium vacuum). For our purposes, an initial low vacuum is required for the proper operation of the subsequent vacuum stages.

The turbomolecular pumps can be switched on once a medium vacuum is achieved. They force air in a preferred direction by momentum transfer. Alternating rotors and static blades at varying inclination compress the air and maintain a massive pressure gradient between intake and exhaust. In principle, turbomolecular pumps can achieve pressures as low as 10^{-10} or even 10^{-11} mbar. They contribute a considerable amount of mechanical noise, however. This is not an issue in some applications, but for probe microscopy as well as for achieving even better vacuum, static pumps like ion pumps and TSPs complement mechanical pumps such as by maintaining vacuum while the mechanical pumps are off during STM measurements.

Speaking of entrapment pumps, an ion pump works by, as the name suggests, ionizing molecules in the gas phase. High voltages (from 3 to 7 kV) are used to accelerate ions against a cathode. Strong magnetic fields then deflect the ionized gas through cells coated with a Ti film which the ions react to and prevent from returning into the rest of the chamber. The layout of the magnets is such that the path taken by the ions and electrons are long enough, increasing the probability of ionizing more molecules before getting adsorbed by the Ti film.

Another entrapment pump present in both the STM and XPS chambers is the titanium sublimation pump (TSP). It operates by sublimating titanium on a cold wall. The Ti film reacts with residual molecules in the chamber like how an ion pump operates. The Ti film is generated by resistively heating a Ti-Mo filament (~50 A), which sublimates titanium. This pump is particularly effective removing residual H_2, water, and other smaller molecules which is more difficult for the mechanical pumps to evacuate.

Lastly, it is worth mentioning that, the double walled cryostat of the LT-STM has the main purpose of cooling down the STM but it acts also as a cryopump.

3.1.3 UHV chambers specifics and attached instrumentation: LT-STM

The LT-STM hangs from a double-walled cryostat and is shielded by a double Al screen which is then in contact with the cryostat. The cryostat is composed of two coaxial thermally isolated cylinders. The outer part (12L) is filled with liquid nitrogen (LN_2) while the inner core is filled with either LN_2 or liquid helium (LHe). This configuration allows to cool down the STM to cryogenic temperatures during experiments – either to 77 K using LN_2 or to 5 K using LHe in the inner cryostat. For the experiments I have included in this dissertation, all STM results were taken at LN_2 temperature/77K. The LT-STM chamber is mounted on pneumatic feet that allow it to be decoupled from the floor and reduce vibrations and other mechanical noises that might affect measurements. The preparation and STM chambers can be isolated from each other using a gate valve to minimize contamination of the STM during sample preparation. The actual STM chamber I have used is shown in Figure 3 with notable components labelled/highlighted.

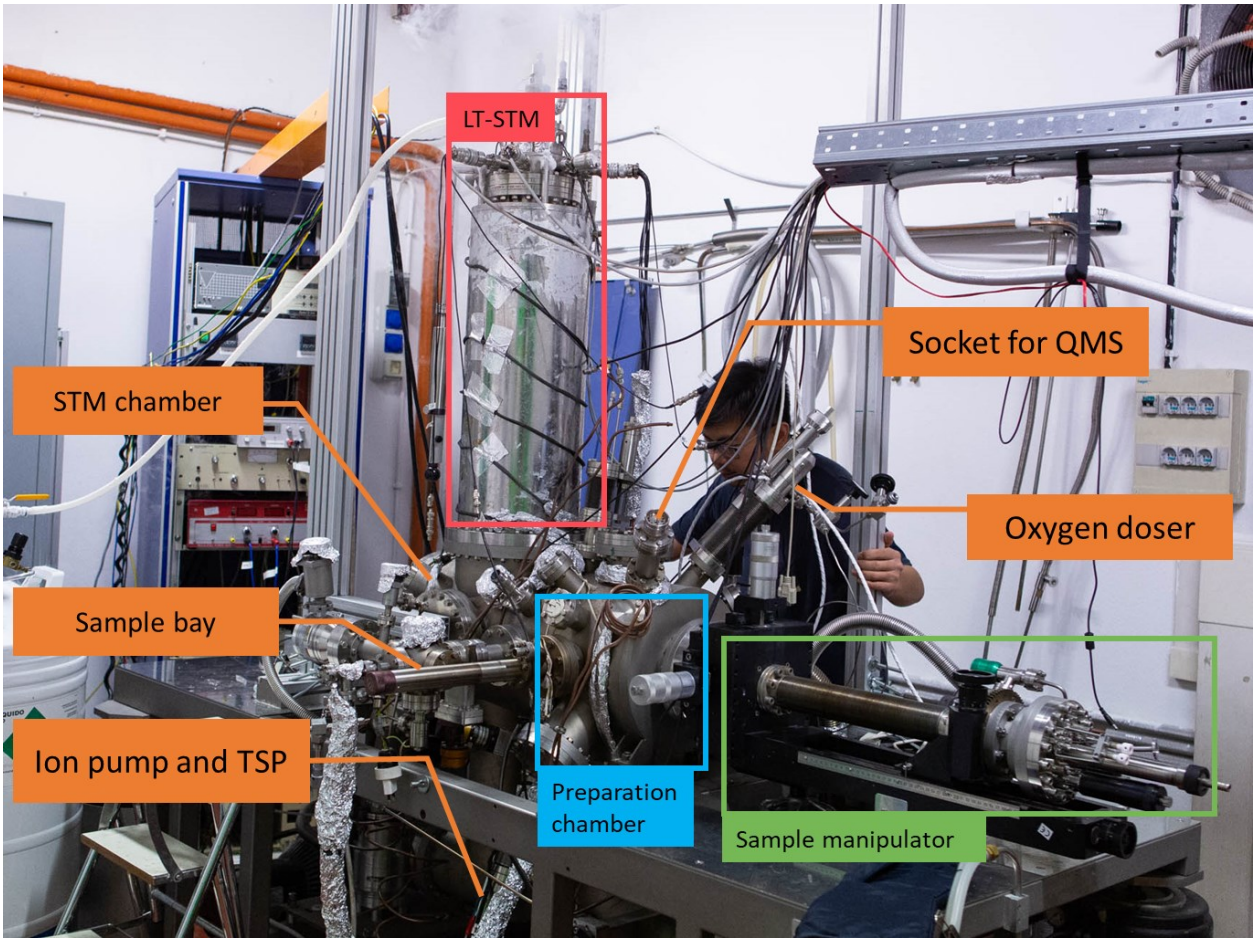

Figure 3 LT-STM with notable parts labelled and highlighted

In particular, I mention:

a. fast entry lock (FEL) which for this chamber is to the side of the preparation chamber and pumped by the small turbo. The transfer rod for this FEL is regularly dismounted and reattached only during introduction or extraction of samples or tips into the preparation chamber.
b. The leak valves and gas lines that serve to dose specific amounts of gases (ex. CO, O_2, Ne) for a variety of applications (sputtering, chemical reactions). In some cases, they are connected to a doser brough at 1 cm from the surface during exposure, in order to increase the local pressure of the specific gas at the sample.
c. The sputtering gun, used to clean samples by ion bombardment.
d. The storage unit inside the preparation chamber, which houses multiple sample holders and tips for convenient storage in the chamber when not in use.
e. The homemade evaporator that is used to sublimate organic molecules onto the sample (see Figure 4). It consists of a tantalum crucible which is resistively heated. The evaporator setup is differentially pumped and can be retracted and isolated with a gate valve. This allows for transfer of the evaporator from the LT-STM to the XPS chamber. The same evaporator was brought to the ALOISA beamline in Trieste, Italy.

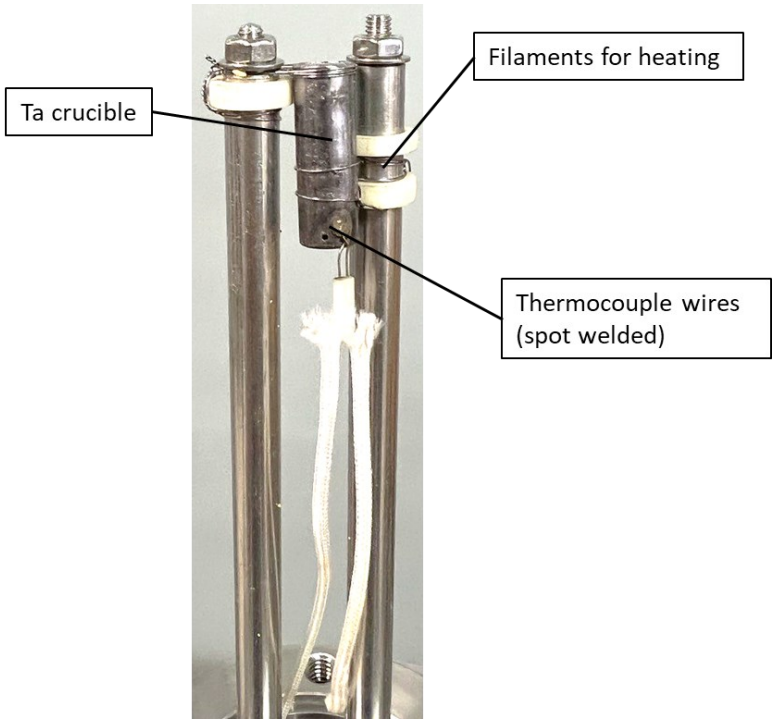

Figure 4. The molecular evaporator

f. The quadrupole mass spectrometer (QMS) (socket labelled), used to check the quality of residual gas, especially during outgassing of the molecules, and the purity of gases introduced into the preparation chamber. The QMS is internally mounted however the electronics are typically detached when not in use.
g. The four degrees of freedom manipulator (Figure 5), that serves several basic key functions such as:

1. Positioning the sample and sample holder in different parts of the preparation chamber depending on the operation required (such as sputtering, deposition, etc.),
2. Inserting and removing the sample holder from the STM,
3. Collecting and placing samples in the sample bay or on the FEL,
4. Providing electrical and thermal connections to the sample.

The manipulator arm terminates with a clamping mechanism shaped like a T (hence called a T-bar) which extends and retracts to grab a suitably designed sample holder (see Figure 5). These objects have a slot on the top side where the T bar can slide from above and clamp in place. 6 electrical contacts in the form of pins stick out from the underside of the manipulator arm. As mentioned earlier, these pins provide electrical connections for the heating element and the thermocouple when the sample is attached to the manipulator. There are also equivalent pins on the inside of the STM to provide electrical contact to the sample while inside the STM (grounding, setting the voltage bias).

Figure 5 manipulator arm with a sample of Ag(110)

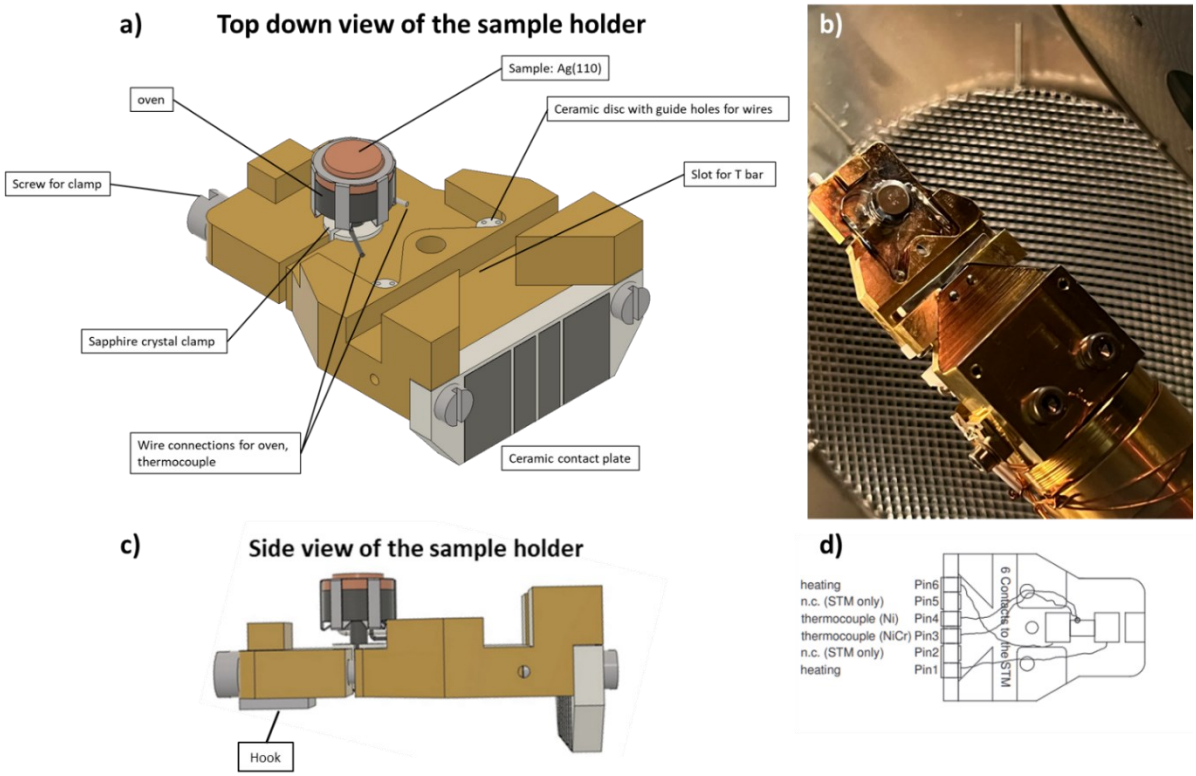

Figure 6. Schematics and actual image of the sample holder (Createc design) used by the LT-STM; a) is a top down view of the sample holder with the parts labelled, b) the sample holder clamped to the manipulator arm, c) is a side view of the sample holder showing the hook that helps position the sample holder inside the STM and d) is the connection layout on the ceramic contact plate connecting the sample to heating, thermocouple, and of course to bias the sample in STM.

The sample holder (see Figure 6a to d) has a special design specific to Createc hardware. It is made of copper and it is gold plated for better oxidation resistance. The sample, a hat-shaped disk 8 mm in diameter is clamped on a button heater. This pair is then fixed in the middle of the sample holder using two fitted sapphire crystals which provide thermal conduction and electrical insulation (Figure 6a). Finally, the filaments and thermocouple wires are bonded to the button heater/sample, respectively. On the other side, they are welded on the copper pads of a ceramic plate, which provide the electrical connection with the pins of the manipulator. These pins press against the contact pads on the sample holder. The specific connection layout and function of each pad and pin are mentioned in Figure 6d. Suitable ceramic parts ensure that the button heater and the sample are electrically isolated from the rest of the sample holder.

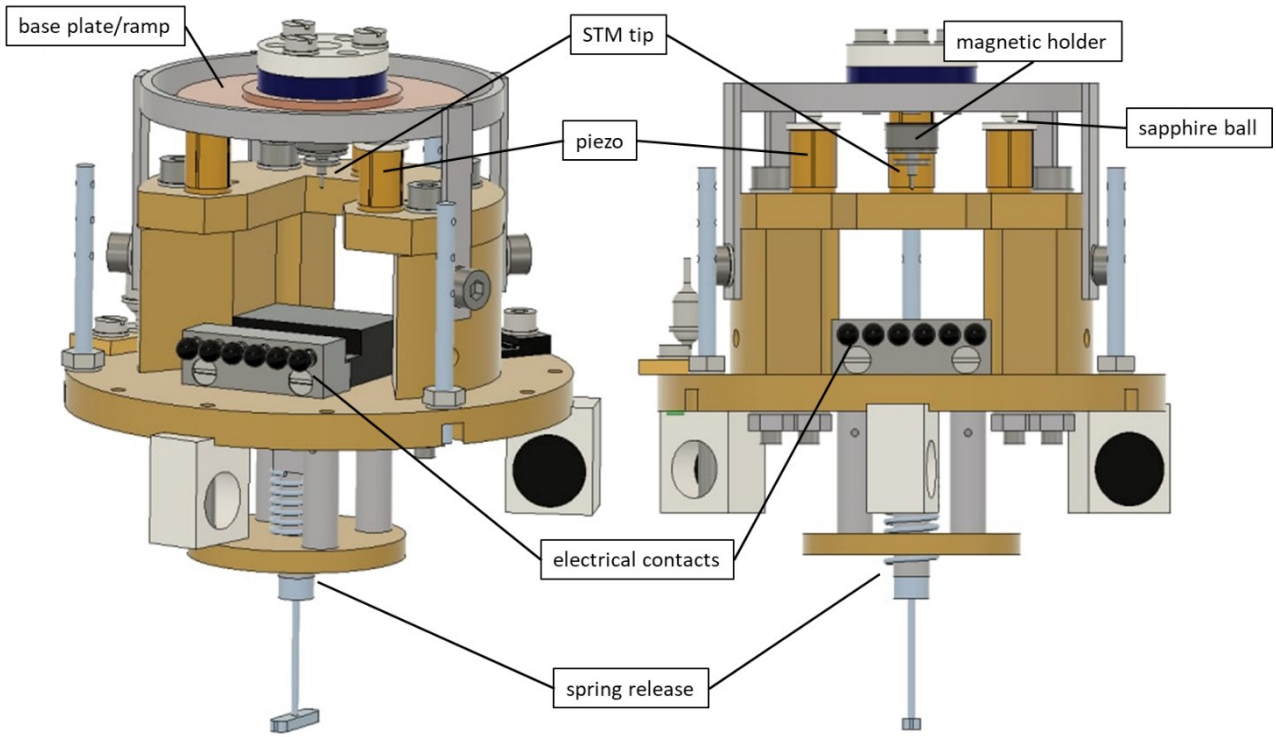

Figure 7. The internal STM scanner based on a modified Besocke type; left (L) is a view at an angle and right (R) is a front view of the STM with the tip, piezo elements, spring, and electrical contacts clearly visible. The housing receives the sample in the cavity in the middle with the electrical contacts aligning with the ones on the sample holder. When in operation, the tip is moved by piezo elements found on the periphery supporting a ceramic disk where the tip is in the center (large lateral movement) as well as the piezo on the tip itself (Z height).

The housing containing the STM tip or scanner can be seen in Figure 7. The scanner is manufactured by Createc and the layout of this scanner is based on an inverted Besocke Beetle type (Figure 7). In an inverted Besocke type layout, the STM tip hangs magnetically attached to a central piezo which in turn is mounted on a base plate. The base plate is supported by three piezoelectric legs while the sample is below. The three piezoelectric legs or pillars are responsible for the lateral displacement or coarse movement (X,Y) and approach (Z) of the tip to the sample. The base plate supporting the central piezo and tip is divided into three sectors. The thickness of each sector increases linearly as you rotate, forming a ramp. Movement is achieved by the piezos letting the base plate or ramp slip and rotate into the desired position. This slip-stick motion is possible because in between the ramp and the piezo legs are ceramic (sapphire) balls, providing enough slip for the base plate to move precisely and therefore to move the tip into the desired position. As the three outer piezos are responsible for larger tip movements, the central piezo governs fine displacement. When the tip has approached and in tunnelling mode, the central piezo typically governs the regulation of the tip height (Z; main scanning mode). The lateral (X,Y) and the Z movement is decoupled for this STM. For moving the tip in the X,Y plane, one can use either the main scanning mode like with the Z control (central piezo) or coarse scanning mode using the three outer piezos. For the experiments here I always used coarse scanning mode for X and Y and main scanning mode for Z. This setup is ideal due to the lower distortion induced by the coarse mode and the better response of the main scanning mode for fine height adjustment. The tunnelling current is measured at the tip while a bias voltage is applied to the sample. Control software for the STM, PSTMAFM, is provided by Createc. The signal chain for the STM goes from the tip → amplifier → A/D (analog to digital) converter → DSP (digital signal processor) → computer. Other electronics include a separate amplifier for piezo movement, an amplifier for the bias voltage, a lock-in amplifier for spectroscopy, and D/A (digital to analog) converters for the piezos and bias voltage.

Lastly, to achieve further mechanical stability, the entire scanner assembly/housing can be decoupled mechanically from the rest of the UHV chamber. It hangs from the bottom of the cryostat by three springs. Besides that, as mentioned earlier the whole chamber rests on pneumatic feet for more mechanical stability and that the STM can be cooled down to cryogenic temperatures. Operating at low temperatures has some obvious advantages. One, because of the cold screens, the pressure inside the STM is actually better than the rest of the chamber. This means that samples inside the STM stay uncontaminated for a longer period of time. Another advantage of scanning at low temperatures is the reduced thermal drift experienced by the system. The added stability allows one to scan a nanoscale area for extended periods, enabling one to acquire data such as bias dependence or dI/dV maps of the same spot for some time. Lastly, low temperatures allow one to investigate systems where adsorbates have low diffusion barriers. The setup effectively freezes surface diffusion of these adsorbates allowing them to be imaged.

3.1.4 Scanning Tunnelling Microscopy: Theory and Operation

In this section I would now briefly discuss the working operation and theory behind STM.

G. Binnig and H. Rohrer developed this technique in 1981, and it soon became a widely used tool in the field of surface science [44–46]. In STM, a conductive probe scans over the sample measuring the current over an electrically conductive or semiconductive surface (Figure 8). The measured tunnelling current depends on the surface electronic density. From this, information such as morphology (Z height), and local density of states (dI/dV) of the surface can be determined while scanning. The STM typically utilizes an atomically sharp tip made from a metal (usually Tungsten) or a metal alloy (usually Platinum/Iridium). The STM generates an image of the surface of the sample with the tip hovering only a few angstroms above the sample. The lateral and vertical movement of the tip is controlled by the piezoelectric elements of the STM. A voltage is applied to the relevant piezo to deflect the tip in the right direction. These piezos act as very precise actuators of the tip. The tunnelling current, which is governed by the quantum behaviour of the electrons (to be elaborated later), is strongly dependent on the physical distance between the tip and the sample and varies by roughly one order of magnitude per angstrom. Tunnelling currents are typically of tens of picoamps, therefore a femto amplifier is used to amplify the signal for measurement. This gives typical STM setups resolutions of up to 1 Å laterally (x,y) and 100 picometers vertically. Lastly, measurements can be done using the bare metal tip or the tip can also be functionalized by a small molecule such as CO to further “sharpen” the tip. The experiments I conducted in Spain on Co-coordinated GNRs were conducted specifically with a Co-functionalized tip. These experiments will be elaborated in the Appendix section of my dissertation.

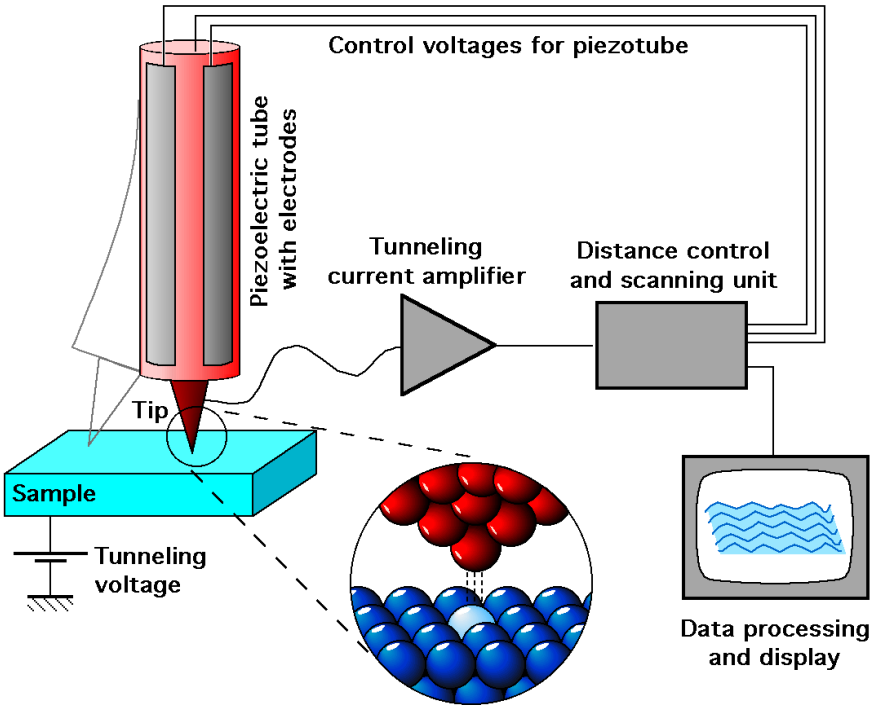

Figure 8 Visualization of how an STM works

3.1.4.1 Tunnelling effect

The tunnelling effect is a quantum phenomenon for which small particles such as electrons have a non-zero probability of crossing a potential energy barrier even though it is higher than the kinetic energy of the particle itself. In other words, electrons can cross regions that are physically speaking, classically forbidden for them to do so. An example of this barrier is the vacuum (gap) between the tip of and STM and the sample being measured. STM takes advantage of the quantum tunnelling effect since electrons can tunnel between two electrodes (the tip and the sample) at a few Angstroms distance. If the barrier is thin enough, the electronic wavefunctions of the tip and the sample can overlap and an effective current can be measured due to this tunnelling effect.

In a simplified model, we can describe the quantum tunnelling process using a 1D system with a potential barrier of width d and potential energy V_0. We split the model into three regions (see Figure 7, top panel) : regions I (the tip) and III (the sample), in which electrons are free particles, and region II (the vacuum in between), in which a barrier is present. An electron of mass m and energy E trying to cross the barrier (region I -> II -> III) can be described using a wavefunction Ψ. Ψ_I is the wavefunction of the electron in region I (see Figure 9). Then, we solve the Schrödinger equations located in the three regions I, II and III to determine the propagation of the wavefunction and calculate the probability of the electron to tunnel into region III.

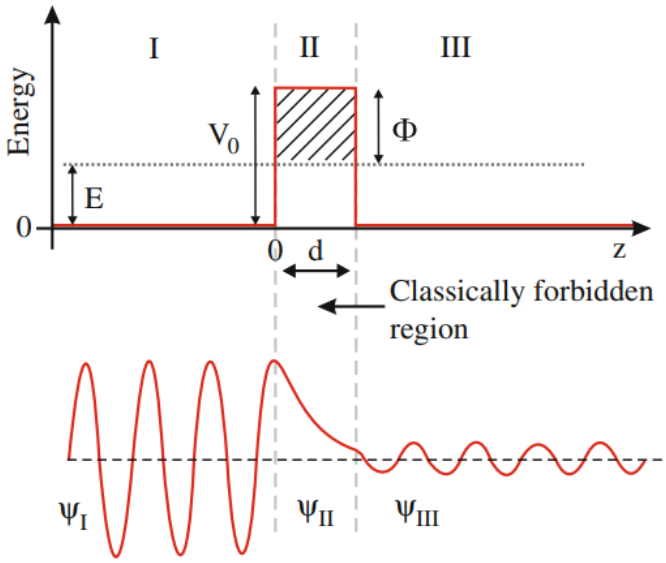

Figure 9. A diagram of the quantum tunneling effect as described by the electronic wavefunction to the left, inside and to the right of the potential barrier; in regions I and III, the electron behaves like a free particle while in region II where $V_0 \geq E$, the amplitude of the wavefunction (when squared gives the probability density) decays exponentially.[47]

Region I:

$$-\frac{\hbar}{2m}\frac{d^2\Psi_I}{dx^2} = E\Psi_I$$

$$\Psi_I = e^{ikx} + Ae^{-ikx} \; with \; k = \sqrt{\frac{2mE}{\hbar^2}}$$

To normalize the wavefunction (calculating the probability we find the electron in that region) we take the absolute square of the wavefunction

$$\Psi_I{}^*\Psi_I = |\Psi_I|^2$$

$$\int_{-\infty}^{\infty} |\Psi_I|^2 dx = 1$$

Region II:

$$-\frac{\hbar}{2m}\frac{d^2\Psi_{II}}{dx^2} + V_0\Psi_{II} = E\Psi_{II}$$

Since $V_0 \geq E$

$$\Psi_{II} = Be^{-ik'x} + Ce^{ik'x} \; with \; k' = \sqrt{\frac{2m(V_0 - E)}{\hbar^2}}$$

Region III:

$$-\frac{\hbar}{2m}\frac{d^2\Psi_{III}}{dx^2} = E\Psi_{III}$$

$$\Psi_{III} = e^{ikx} \; with \; k = \sqrt{\frac{2mE}{\hbar^2}}$$

$$\Psi_{III}{}^{*}\Psi_{III} = |\Psi_{III}|^2$$

$$\int_{-\infty}^{\infty} |\Psi_{III}|^2 dx = 1$$

Coefficients A, B and C are determined by matching the amplitudes and the first derivatives of the three waves at the discontinuity points (x=0 and x=d). In regions I and III, where we assume V=0, the solutions of the Schrödinger equation take the form of an oscillating wave (free electron) $\Psi = Ae^{ikx}$ (note that for region I there are two waves: reflected and transmitted). In region II, on the contrary, *k* is imaginary and the solution collapses into a decaying exponential with the form $\Psi = e^{-k'x}$ where $k' = \sqrt{\frac{2m(V_0-E)}{\hbar^2}}$.

As mentioned earlier, regions I and III correspond to the tip and the sample, while region II is the vacuum in-between. From the above equations it is possible to derive that the tunneling current, which is proportional to the transmission factor and depends on the tip-sample distance as $I \propto e^{-2k'd}$. This basically means that there is a tiny portion of the electronic waveform that spills over the barrier and there is a non-zero probability of finding the electron in III. Practically speaking, the transmission factor corresponds to the flux of electrons or electric current coming out from the potential barrier. From the perspective of the STM instrument, this appears as a current in the range of tens of pA to a few nA.

It should be noted that this negative exponential relation explains the sensitivity of the STM technique to the surface corrugation since k' is ≈1 Å for a work function of ϕ~4.5 eV, typical of metals, yielding a reduction of the tunneling current of approximately one order of magnitude every Å increase in the barrier width i.e. in the tip-surface distance.

***Bardeen formalism**

The formalism I have just illustrated allows one to calculate the tunnelling probability of one electron. [48] However, the presence of many electrons available to tunnel must be considered. These electrons are in different states. A formalism can be developed considering a finite number of discrete states but, in the present case, considering a continuum of states is more appropriate.

To further elaborate on the tunnelling process, we could use the Bardeen approach to describe the process as a problem in 3 dimensions.

$$I_T = \frac{4\pi e}{h} \int_0^{eV} \rho_s(E_F - eV)\rho_T(E_F + \varepsilon)|M|^2 d\varepsilon$$

Hence, we describe the tunnelling current as the convolution of the density of states between the sample and the tip. M is the tunnelling matrix, ρ_s and ρ_T are the surface density of states of the sample and the tip respectively and E_F is the fermi energy. When we solve for I_T the integration simplifies to $I_T \propto e^{-2ks}$, equivalent to the result we can get when solving for the 1D approximation. Another implication of this formalism is that we can determine the direction of the tunnelling current, either the electrons from the filled states of the sample move to the empty states of the tip or vice versa. A useful illustration of this can be seen in Figure 10. To detect a flow of current the Fermi levels of the tip and the sample need to be at different energies. This is done by applying a bias to either the tip or the sample. Assuming that the biasing is done on the sample, negative bias increases the Fermi level of the sample with respect to the tip (left side of Figure 10). This allows electrons in the filled states

of the sample to tunnel into the empty states of the tip (by convention current flows opposite of electron flux). In this case, valence band states and highest occupied molecular orbitals (HOMO) are probed. If the sample is positively biased, the Fermi level of the sample is lower than the one of the tip (right side of Figure 10, so that electrons tunnel from the tip to the sample. In this setup, the conduction band and the lowest unoccupied molecular orbitals (LUMO) are probed.

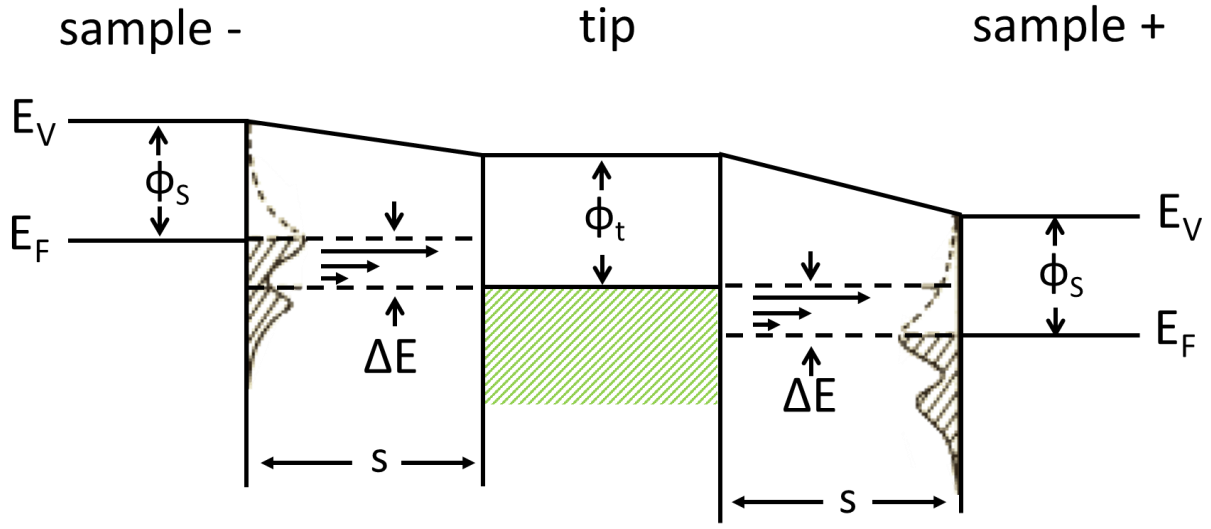

Figure 10 Illustration of the Fermi energy, vacuum and work functions for sample and tip depending on the bias

3.1.5 Operating procedure

To actually collect an image with the STM, some general steps are always followed. First, assuming that the temperature inside the STM is stable (77K or 5K), the tip can be directed to approach the sample. This is done automatically by the computer with the input by user being the physical position of the tip above the area to be scanned, the initial bias voltage, set point (the target tunnelling current when in constant current mode) and the rate of approach. Once in tunnelling and assuming the tip did not crash, the user can set the final settings for bias voltage, scan speed, and set point before acquiring an image. Samples vary, but a good base line would be to scan at a relatively low set point (0.1 to 0.5 nA) and bias of 500 mV to 1000 mV. This sets the tip at a relatively safe distance and the bias high enough to discourage molecules from sticking to the tip unintentionally. Main STM images were processed using WxSM [49]. All other graphs such as line scans were further processed in Igor (ver. 6) for visualization purposes.

3.1.6 Scanning Tunnelling Spectroscopy: Operation and Theory

One application of the STM hardware, ours included (Createc manufacturer), consists in the measuring of the local density of states (LDOS) of the surface. The formulas below show that the tunnelling current is proportional to the LDOS of the sample integrated from the Fermi energy to eV_0.

$$I = \frac{4\pi e}{\hbar}\int_0^{eV} \rho_{tip}(\varepsilon - eV)\rho_{sample}(\varepsilon)T(\varepsilon, V, d)d\varepsilon$$

$$\frac{dI}{dV} \approx \frac{4\pi e}{\hbar}\rho_{tip}(0)\rho_{sample}(eV)T(eV, V, d)$$

$$\frac{dI}{dV} \propto \rho_{sample}(eV)$$

Recall that the "image" generated by the STM is based on the changes in the current detected by the system as the tip raster scans across the surface. In constant current mode, the displacement of the tip along the Z axis (Z height) is recorded and is used to generate the "image" of the sample. Because this tunnelling current is dependent both on the distance between the tip and sample and on the conductivity or presence of electronic states in the sample, we can use the same tunnelling effect to further probe those electronic states.

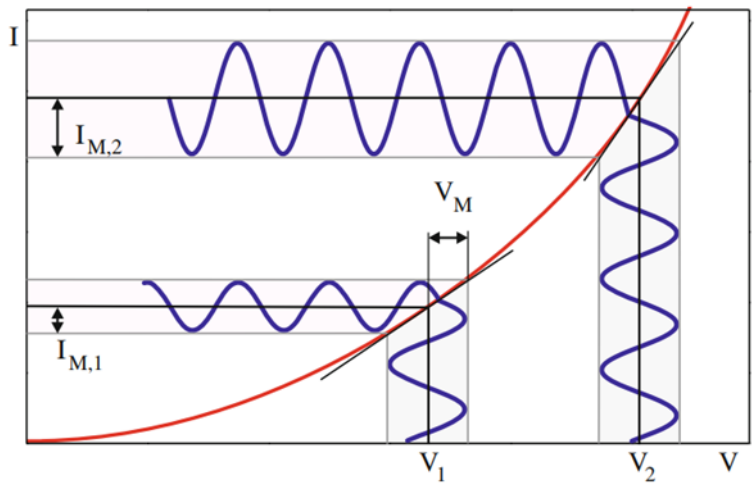

Figure 11. Scanning Tunneling Spectroscopy (STS) relies on the modulation of the bias voltage (V_M). This generates a modulation on the tunneling current (I_M) which, taking its 1st derivative, yields local density.

The basic principle behind scanning tunnelling spectroscopy (STS) is that it is possible to generate a differential conductance spectrum from an I/V curve (like in linear sweep voltammetry) but a dI/dV spectrum can be measured using a modulation or lock in technique for which the modulation in tunnelling current is induced by a modulating voltage. Since the STM is normally not operated with alternating current (AC), a small modulation voltage $V_M \cos \omega t$ is applied to the bias voltage V. The fluctuations or alternating current is then generated and recorded. The amplitude of the AC signal is proportional to the first derivative (dI/dV) (slope of the line Figure 11) of the incoming current which in turn is dependent on the presence (or absence) of local electron density across the surface of the sample. In other words, the differential conductance is proportional to the convolution of the local density of states of the tip and the sample as shown in the equations at the beginning of this section. The measurement of dI/dV is taken along the spectral width set by the amplitude of the modulating voltage as shown in Figure 11, and therefore the resolution of the STS is limited by the amplitude of the modulation voltage.

This is a powerful complementary technique to determine the electronic structure of the sample. For molecules, for example, this could mean seeing the onset of the valence and conduction bands (or the HOMO/LUMO) and therefore, the band gap.

3.1.7 STM calibration

Calibration of the STM is necessary to determine the dimensions of features we see on the surface of a sample. To calibrate the STM, we take the image of a surface lattice of well-known periodicity (typically determined by X-ray diffraction), and we adjust the piezo constants accordingly. The piezo constants are the conversion factors between the voltage applied to the piezos during the scan and the distance covered by the tip. They can be adjusted using the formula:

$$(1) \qquad C_{piezo}(new) = C_{piezo}(old)\frac{d}{d_{meas}}$$

Both the lateral and vertical movement of the tip are related to the physical deflection and compression of the piezo elements which are lower at lower T for any given voltage. Therefore, different C_{piezo} values will be appropriate when scanning at LN_2 (77 K) and at LHe (4 K) temperatures Because of this, the calibration process needs to be repeated at each T.

At 77 K I calibrated the piezoconstants for the lateral position of the tip both on atomically resolved images of clean Ag(110) (Figure 12a and table 1) and of O-Ag(110) added row reconstructed surface (Figure 12b and table 1), while the vertical motion (Z coordinate) is calibrated on the height of single steps (Figure 12c). The default lateral positioning of the tip is determined by a scan back and forth in the x direction as the scanning tip moves along the y direction. For example, on the clean surface (Figure 12a) I measured a periodicity of 2.4 Å and 4.1 Å in the $\langle 1\bar{1}0 \rangle$ and $\langle 001 \rangle$ directions, respectively These have to be compared with the values of the primitive unit cell for the Ag(110) surface of 2.89 Å and 4.09 Å. The data indicate that there is a slight compression of the image along the y direction. This effect is often present due to thermal drift and hysteresis of the piezo elements. Therefore, I consider only the line scan in the x direction for calibration and I notice that, according to formula (1), the correction factor is $\frac{d}{d_{meas}} = 1.01$, a difference of 1%. Acceptable deviation given the nature of the measurement and limits of the STM would be anywhere up to 5%. This correction therefore is well within the uncertainty of the measurement and so it is reasonable to say that the X and Y piezoconstants are calibrated in this case.

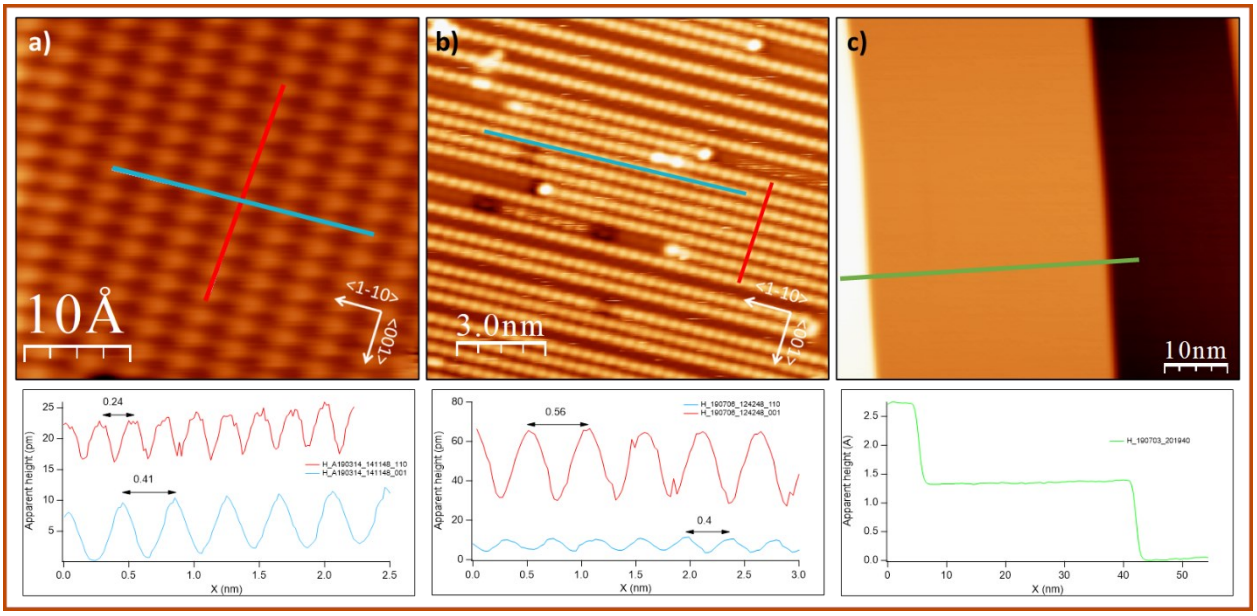

Figure 12 Line scans of different periodicities measured on a) clean Ag (110) and as well as b) added rows forming when Ag is exposed to O_2 at RT. c) Line scan across a step. Note the differrent scale in the apparent height of panels a and b with respect to panel c (line scans).

		Expected value (Å)	Measured value (Å)	Initial piezoconstant (Å/V)	Adjusted piezoconstant (Å/V)
LN_2 (77 K)	<1-10>	5.78	5.6	C_x=25	C_x =25
	<001>	4.09	4.0	C_y=25	C_y=25
	Step height	1.41	2	C_z =12	C_z =9
LHe (4 K)	<1-10>	5.78	5.3	C_x =12	C_x =14
	<001>	4.09	4.1	C_y=12	C_y=14
	Step height	1.41	1.4	C_z=6	C_z =6

Table 1 piezoconstant calibration parameters for LN_2 and LHe temperatures determined using the Ag-O-(2x1) surface reconstruction

3.1.8 UHV chambers specifics and attached instrumentation: XPS

The UHV chamber housing the XPS contains multiple complementary instruments. A view of the chamber is shown on Figure 13.

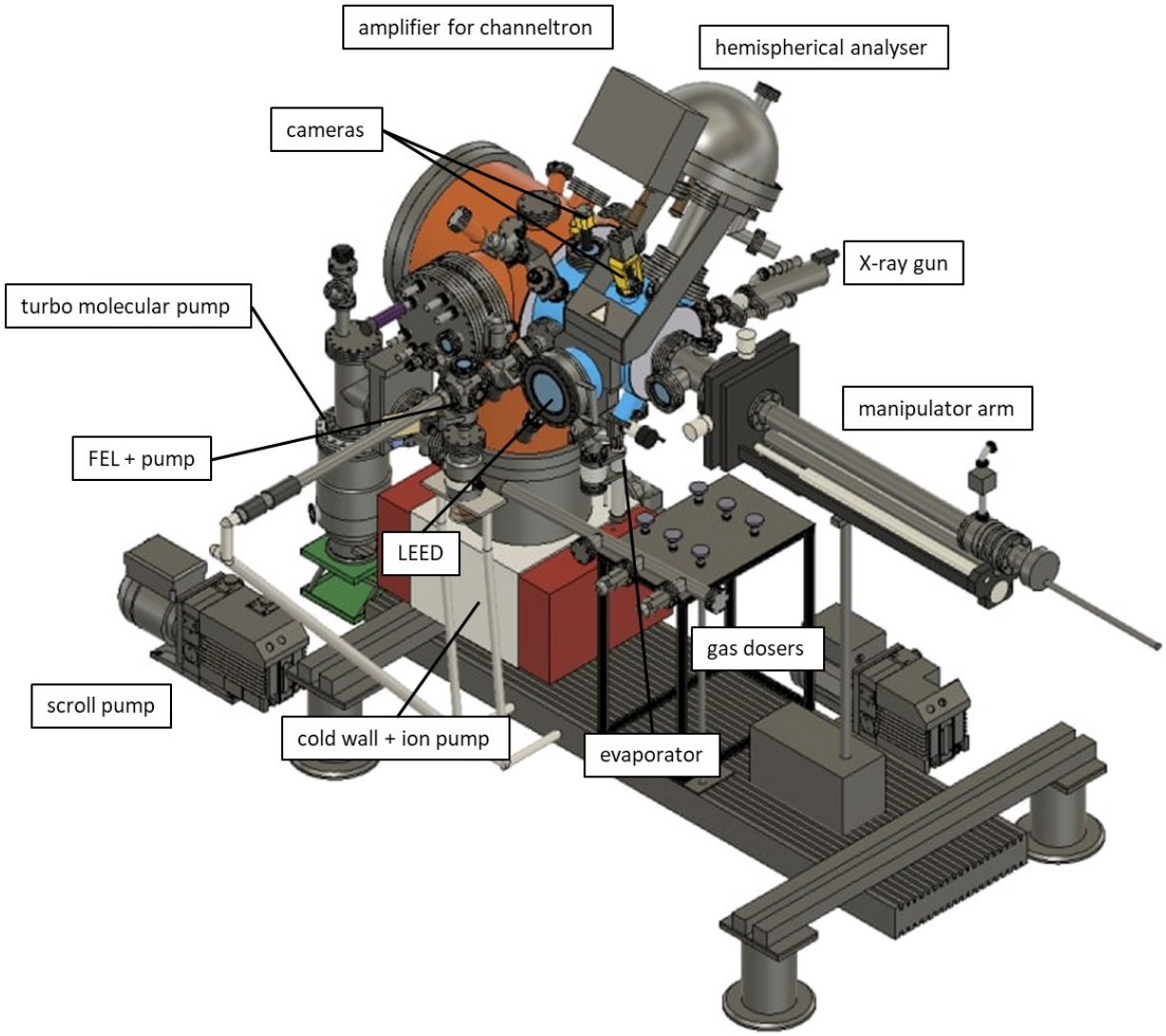

Figure 13. Schematic of the XPS chamber (Omicron) created in AutoCAD (c/o Simone Passaglia and Giovanni Carraro)

I underline the presence of:

a. A series of leak valves for dosing gases into the chamber.
b. High-resolution electron energy loss spectrometer (HREELS, not shown) and a low electron energy diffractometer (LEED), not used in my thesis.
c. An ion gun for surface cleaning (not shown)
d. A quadrupole mass spectrometer for residual gas analysis (not shown).
e. Fast lock entry (FEL) for transferring samples in and out of the chamber.

f. The XPS setup, consisting of an Omicron EA125 hemispherical analyser and a Omicron DAR400 X-ray source (non-monochromatized, dual Mg-Al anode).

A four degrees of freedom manipulator, which serves the same functions as the one present in the LT-STM chamber. However, the sample holder is a flag-type sample holder (as shown in Figure 14). The sample is clamped to the base (usually molybdenum) with spot-welded wires and the base is held on the end of the manipulator arm by tabs. The heating elements (filaments) on the manipulator arm are directly below the sample and the thermocouples are soldered somewhere adjacent to the sample holder. The sample is heated by electron bombardment. The filaments are heated and emit electrons by thermoionic effect. These electrons are then accelerated by biasing the sample (+) and would hit the back of the sample holder, heating the sample. Due to this configuration, the temperature reading is affected by a systematic error and is probably underestimated by 50-100 °C. This is inferred based on a calibration curve in which the read temperature was compared with the one measured by a pyrometer.

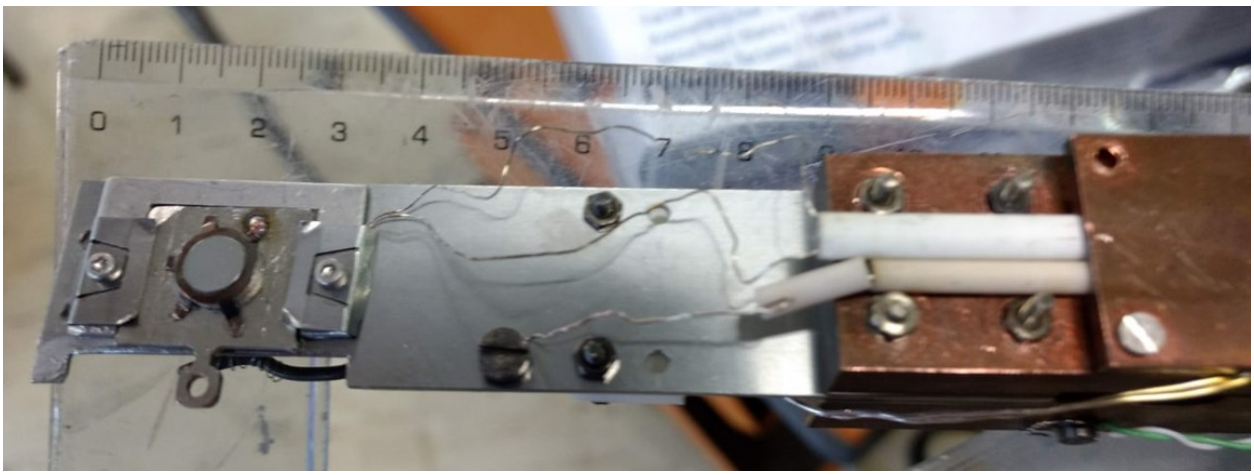

Figure 14. Flag-type sample holder for Omicron instruments. Seen here is a flixed Mo plate with a knob or ring to grab the plate with the sample on top. The electrical connections (bias voltage, thermocouple) is attached to the receptacle where the sample holder is held by tabs on either side. This is designed for easy sample transfer without breaking the vacuum (using an FEL).

For the XPS setup, the X-ray source for this chamber is a DAR400 from Omicron. It contains two anodes and one can select the energy to be used in the experiment (Al will generate light with the energy equivalent of $K\alpha_{Al}$ = 1486.6 eV and Mg will generate at $K\alpha_{Mg}$ = 1253.6 eV). For the purposes of the XPS experiments done in our chamber, I used $K\alpha_{Al}$ for those experiments.

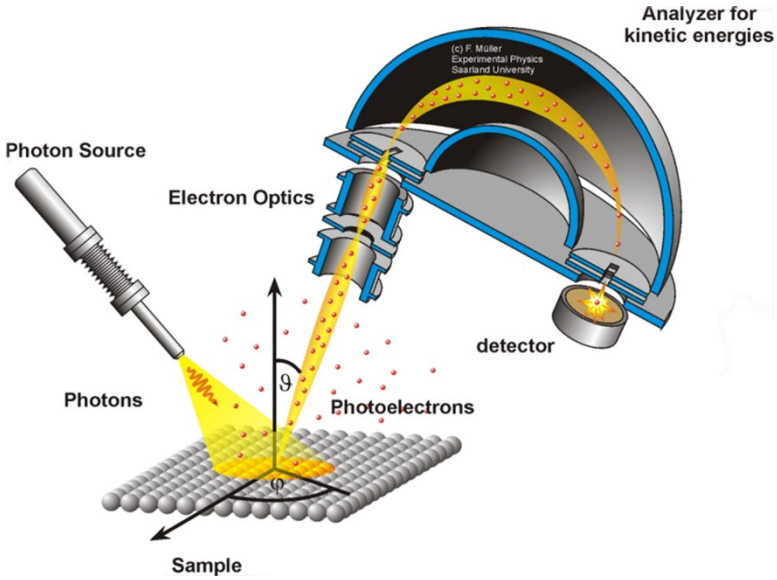

Figure 15. Diagram of a typical hemispherical analyzer for XPS. The XPS here is depicted with a non-monochromatized light source.

The hemispherical analyzer (Omicron EA125) has two main functions. It collects the photoemission electrons from the sample and with the channeltrons boost the signal of the detected electrons to a useable and readable measurement. First, upon the emission of electrons on the surface, the process of which will be elaborated later, the electrons pass through and are directed by a series of electrostatic lens at the input end of the analyzer. The collected electrons are then forced into a curved path by concentric spheres biased positive and negative with respect to the set pass energy. The electrons that make it on the output end are detected by channel electron multipliers or channeltrons. Our XPS has five channeltrons and these amplify the signal by a factor of 10^8 in order to produce a readable XPS spectrum of the sample.

3.1.9 X-ray Photoemission Spectroscopy: Operation and Theory

X-ray photoemission spectroscopy (XPS) was first conceived by Kai Siegbahn and his group in the 1960s at the University of Uppsala, Sweden for chemical analysis of surfaces (hence the older name Electron Spectroscopy for Chemical Analysis). Photoemission spectroscopy is a surface sensitive technique that uses the photoelectric effect to gather chemical information on the surface of a sample. For XPS specifically, the technique uses X-rays to excite core shell electrons. The kinetic energy (KE) of the photoelectrons can be measured, and the corresponding binding energy (Eb) can be subsequently determined. The binding energies of the core shell electrons are peculiar of each element, of each atomic level and of the elemental chemical state, therefore they provide information on the chemical composition of the surface and on the chemical bonds and oxidation states of the elements.

The process begins by irradiating the sample with an X-ray beam of high enough energy to to induce the photoelectric effect and eject electrons from the core shells of the elements (K shell, L shell) (the photoelectric effect is illustrated in more detail on Figure 16). The emitted electrons have kinetic energy given by:

$$KE = h\upsilon - E_b - \phi_s$$

Where hν is the photon energy, Eb is the binding energy of the atomic orbital where the electron originates, and φs is the spectrometer work function. The formula indicates that the kinetic energy of the photoelectrons can be measured, and the corresponding binding energies of those electrons can be subsequently determined. The binding energies of the core shell electrons correlate to the chemical

composition of the surface including what elements are present, chemical bonds and oxidation states of the elements.

Figure 16 depicts that the photoemission is just one of the many processes that may occur: photon-induced Auger peaks, valence band electrons, inelastic scattering processes and other features like shake-up and shake-off satellites.

Finally, an important characteristic of XPS is its surface sensitivity. Photons have a greater penetration depth than electrons (micrometers versus angstroms, depending on the energy of the photoemitted electrons) due to lower probability of interaction with matter. Therefore, even if ionization can occur micrometers in depth, only the electrons coming from tens of angstroms deep can escape from the surface and be detected.

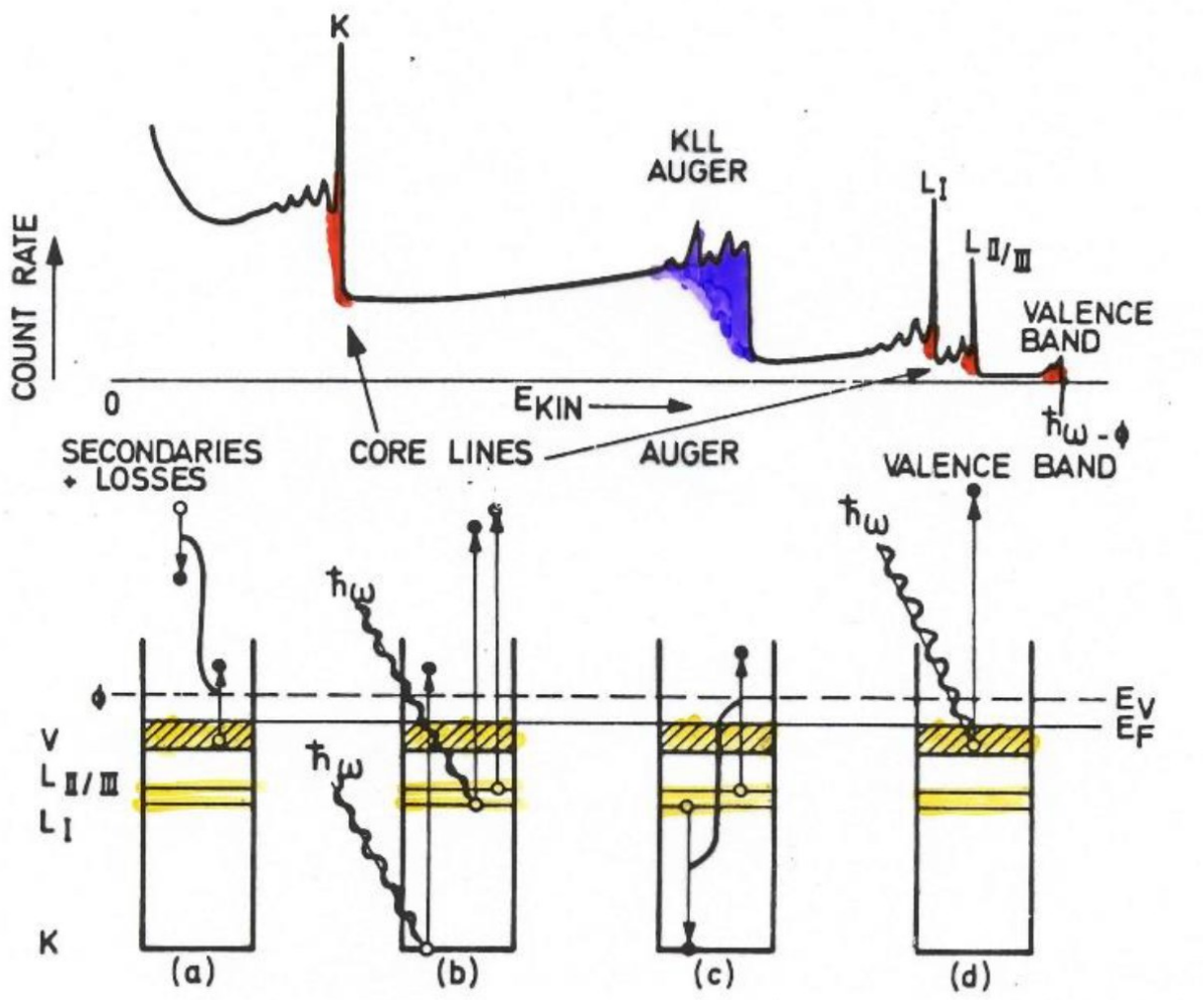

Figure 16 Different photoelectric processes (photoemission, Auger, secondary processes) and their corresponding positions on a spectra

Some of my experiments were performed at University of Genia and some at the ANCHOR endstation of the ALOISA beamline (Elettra Synchrotron Light Source) in Trieste, as discussed below.

Genoa

3.1.10 Calibration and analysis of XPS spectra

XPS results referenced in this dissertation come from two different setups. For the XPS spectra of the oxygen-exposed GNRs and for AB001, I used the UHV chamber described in section 3.1.8, which hosts a standard X-ray source (DAR400 by Omicron in my setup) containing a cathode filament and an anode. The electrons from the cathode are emitted and accelerated over a potential of 15 kV towards the anode producing X-ray photons. I used a non-monochromatized Al/Mg Ka X-ray source (Al Kα = 1486.6 eV or Mg Kα= 1253.6. The generated X ray photons have energy widths of 0.85 and 0.70 eV, respectively. The linewidth depends on the anode material and in our setup is the main limiting factor for the instrument's resolution

Experiments involving CyPd were done using synchrotron radiation. High resolution X-ray photoemission experiments were performed at the ANCHOR endstation, ALOISA beamline Elettra synchrotron in Trieste. Photoemission experiments were carried out using a Phoibos 150 analyzer (SPECS manufacturer). XPS spectra were recorded at normal emission and at a photon energy hν=515 eV. The instrumental resolution of 0.15 eV and the calibration of the binding energy (E_b) were determined by recording the Fermi edge of the Ag(110) substrate using software to zero the position of the Fermi edge. The Ag $3d_{5/2}$ line of the clean surface is found at E_b(Ag $3d_{5/2}$)= 368.21 eV after calibration, in agreement with literature data (Citrin et al., 1983). Core level spectra were fitted with Doniach-Sunjic line shapes convoluted with a Gaussian profile after subtraction of a linear background. ±5% error is estimated for the fitted intensities. Specific fits would be elaborated in the next chapter.

All other spectra were recorded at University of Genoa and with $Al_{K\alpha}$ photons and at normal emission. Calibration of the spectra was done by fixing the Ag $3d_{5/2}$ line at E_b=368.25 eV, in accord to literature values [ref]. This method is chosen because Ag has the strongest signal due to the substrate bulk material being Ag.

All graphs (spectra) from the XPS were processed in KolXPD and further processed in Igor (ver. 6) for visualization purposes.

3.2 TECHNIQUES USED BY AFFILIATES

Aside from the techniques mentioned here, some results in the following sections were acquired using techniques from our collaborators. High resolution X-ray photoemission (HR-XPS) experiments were carried out at ANCHOR-SUNDYN end-station of the ALOISA beamline at the Elettra synchrotron radiation facility (Trieste, Italy) [50]. Density Functional Theory (DFT) calculations were performed by our collaborators from UNIMIB headed by Cristina de Valentin and Daniele Perilli.

3.2.1 High resolution XPS and NEXAFS

High resolution photoemission and NEXAFS experiments were carried out at the ANCHOR endstation of the ALOISA beamline (Elettra Synchrotron Light Source) in Trieste. The system consists of an UHV chamber designed for in-situ growth of organic thin films. HR-XPS and NEXAFS takes

advantage of the high photon flux and tunability of the photon energy of the X-rays generated in the synchrotron. Synchrotron radiation is generated from deflecting charged particles (e.g., electrons) accelerated to relativistic speeds. The particles are deflected by magnets and, upon deflection, emit electromagnetic radiation in the form of X-rays, as shown in Figure 17. simplified diagram of a synchrotron and magnet placement producing either plane polarized or highly collimated light. Synchrotron radiation is an intense light source with narrow angular divergence, which along with slits, monochromators and different magnet configurations enables one to perform high energy resolution experiments with a very well collimated beam. In comparison to more conventional XPS setups, the radiation source has a continuous spectrum which allows tuning to any desired energy using undulator gaps and monochromators.

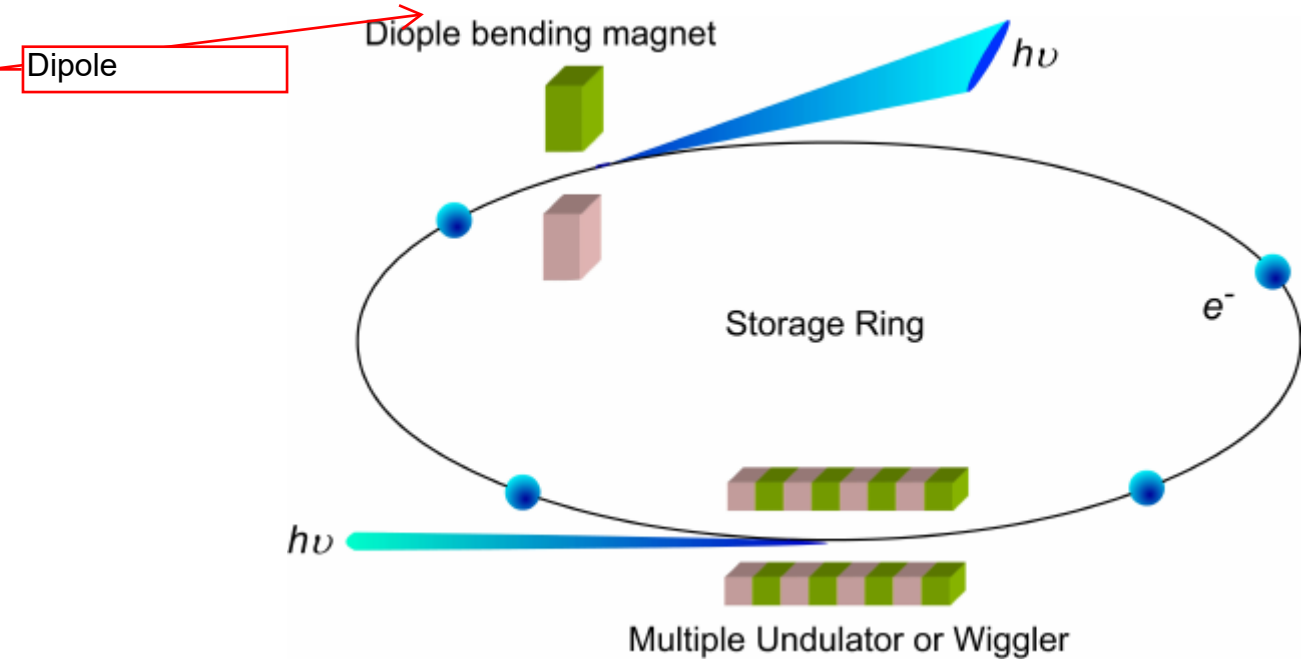

Figure 17. simplified diagram of a synchrotron and magnet placement producing either plane polarized or highly collimated light

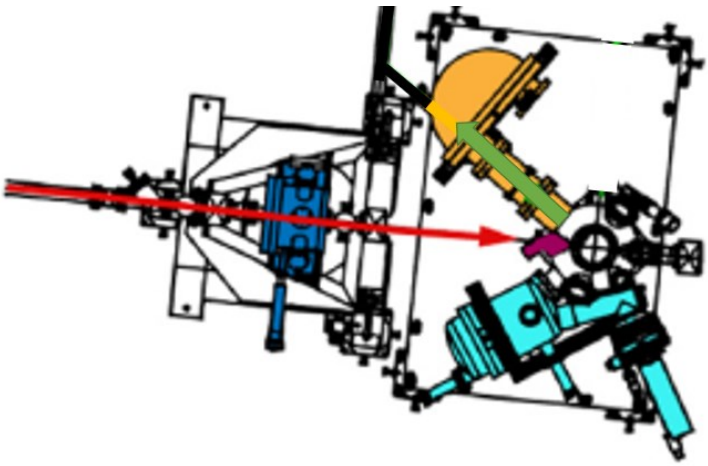

Figure 18. Schematic of the ALOISA beamline in Elettra (Trieste)

3.2.1.1 NEXAFS

Near Edge Absorption Fine Structure (NEXAFS) spectroscopy is an edge adsorption spectroscopy first used in 1983 by Jo Stohr [51]. This surface-sensitive technique is able to probe the orientation of molecular bonds of adsorbed molecules on a surface. The experiment works by how molecules absorb photons. Photons are absorbed by a molecule if the photon energy corresponds to an electronic transition from a core-level to an unoccupied molecular orbital. These electronic transitions include π^* orbitals and Rydberg states located just below the Fermi level and σ^* resonances in the continuum of unbound states, as shown in Figure 19. The resulting excited state decays by emission of an Auger electron or photon emission (fluorescence). These transitions and subsequent decays appear as resonances in the recorded spectrum. NEXAFS measurements are exclusively performed with synchrotron radiation because a tunable X-ray source is required. The investigated energy range is selected based on the adsorption edge of interest. For the experiments in this thesis, the C and N K-edges (transitions of 1s electrons of the corresponding atoms – respectively around 285 and 400 eV) were recorded in Auger electron yield. As for XPS, the experiment is particularly surface sensitive due to the limited mean free path of electrons.

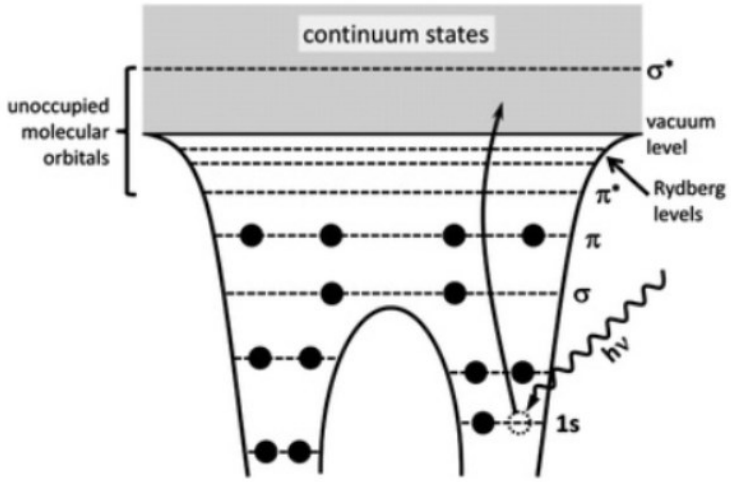

Figure 19. Various possible transitions occurring around the Fermi level, among which include transitions that could be probed by NEXAFS (π->π, Rydberg states, etc.)*

Probing transitions close to/surrounding Fermi (like σ -> σ^* or π* transitions) provide important information on the orientation of molecular bonds with respect to the surface. NEXAFS spectra contain all allowed transitions because these depend on the density of empty states. Dipole selection rules predict whether a transition is allowed or not.

For linearly polarized light and a 1s initial state, the intensity of a resonance is largest when $\vec{E}$ lies along the direction of the final state molecular orbital (a peak in the spectra) and vanishes when $\vec{E}$ is perpendicular to it. This is due to the directionality of the orbitals. Given that molecular orbitals involving π especially has an angular momentum dependence, recording spectra with at different light polarization can determine if there is a preferential orientation of a molecular orbital and therefore the molecule with respect to the substrate, see Figure 20.

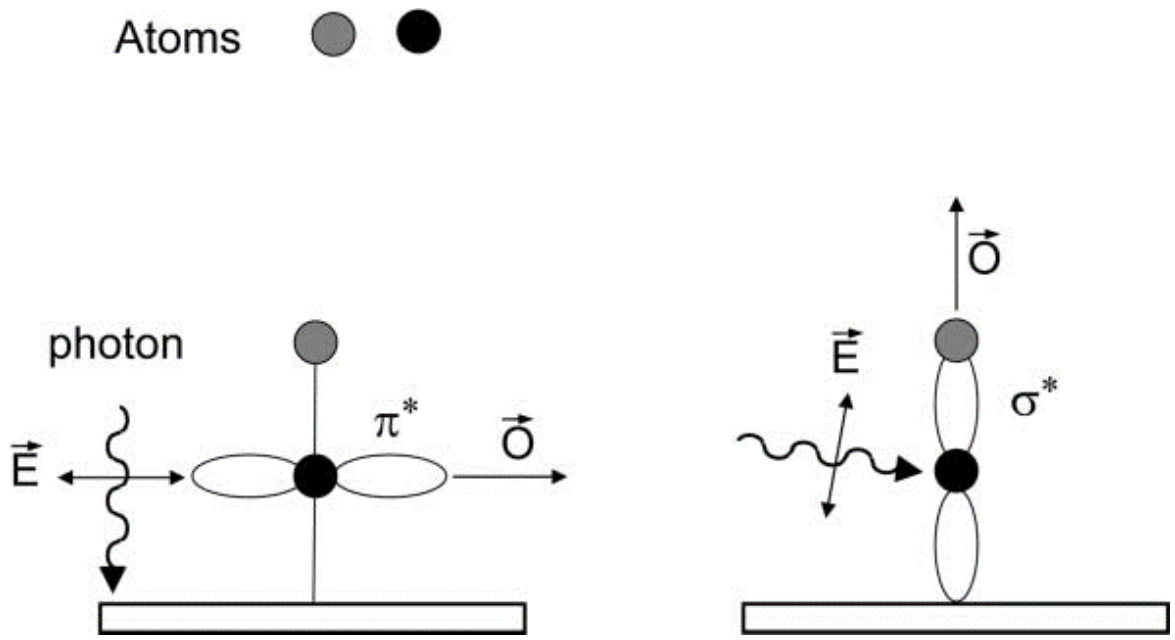

Figure 20. Polarization dependent NEXAFS allows for determining the molecular orientation on the surface.

3.2.2 NEXAFS analysis

The NEXAFS spectra were acquired in Auger electron yield mode recording C and N KVV Auger electrons. The hemispherical electron analyzer was fixed at a kinetic energy of 262 eV and 385 eV for the C and N K-edges, respectively. A two-step normalization process is used for the spectra. First, a multiplication factor is applied to scale the intensity before the energy threshold to the one of the clean surface. This corrects for unwanted variations of the X-ray beam intensity. Then the ratio between the so-normalized spectrum and the spectrum of the clean surface is plotted (Joachim Stöhr, 1992). This second step reduces the signals due to impurities and the substrate, leaving only the contributions of the adsorbates in the NEXAFS signal.

3.2.3 Computational methods (density functional theory)

An important complementary tool to complete the interpretation of my data is Density Functional Theory (DFT). Geometry optimization and simulation of STM images were performed by Dr. Daniele Perilli and Prof. Cristiana di Valentin (University of Milano Bicocca) starting from the experimental inputs provided by my experimental work.

DFT is a method using quantum mechanical principles to model periodic systems. DFT is used to investigate the electronic structure of many-body systems at their ground states. This in turn is done by solving electronic wave functions using the electron density $n(\vec{r})$ of the objects one is trying to describe.

DFT calculations were performed using the plane-wave-based Quantum ESPRESSO package (QE) (P Giannozzi et al., 2017; Paolo Giannozzi et al., 2009, 2020). The ultrasoft pseudopotentials were adopted to describe the electron-ion interaction with Ag (4d, 5s), Pd (4d, 5s), C (2s, 2p), N (2s, 2p), Cl (3s, 3p), Br (4s, 4p), and H (1s), treated as valence electrons. Energy cutoffs of 45 Ry and 360 Ry (for kinetic energy and charge density expansion, respectively) were adopted for all calculations. The Van

der Waals density functional vdW-DF2^{C09x} was used for electron exchange-correlation [52], which gives an accurate description of the adsorption energies and distances of graphene on metal surfaces [53] and has also been successfully applied to describe self-assembly of brominated tetracene (DBT) on different metal surfaces [35,54–56].

For the simulation of the Ag(110)-supported **CyPd** (**CyPd**/Ag), a (2√3**a** × 3√3**b**)R55 supercell was used, where **a** and **b** are the lattice vectors of the Ag(110) unit cell (2.88 Å and 4.07 Å, respectively, in perfect agreement with the experimental values). Such a cell has been chosen to match the experimental cell.

The geometry relaxation of all considered systems was performed with a 4 × 2 × 1 Monkhorst-Pack k-points mesh [57], followed by a non-self-consistent field (NSCF) calculation with a 12 × 6 × 1 Monkhorst-Pack k-points mesh for evaluating the electronic properties.

The Ag(110) surface was modeled by a three-layer slab with the bottom layer fixed to the bulk positions during the geometry relaxation to mimic a semi-infinite solid. To avoid interactions between adjacent periodic images, a vacuum space of about 25 Å in the direction perpendicular to the surface was used.

For the simulation of the Ag(110)-c(2×2) supported CyPd (CyPd/Ag-c(2×2)), a (6 **a** × 3√2 **a**) supercell was used, where **a** is the cubic lattice parameter of Ag bulk (4.07 Å, in agreement with the experimental value). The Ag(110) surface was modeled by a three-layer slab with the bottom layer fixed to the bulk positions during the geometry relaxation to mimic a semi-infinite solid. The c(2×2) reconstruction was modeled by adding 0.5 ML of Ag adatoms on 4-fold hollow sites. To avoid interactions between adjacent periodic images, a vacuum space of about 18 Å in the direction perpendicular to the surface was used. The geometry relaxation of all considered systems was performed with a 2 × 3 × 1 Monkhorst- Pack k-points mesh [57].

STM simulations were performed using the Tersoff-Hamann approach [58], according to which the tunneling current is proportional to the energy-integrated Local Density of States (ILDOS). STM images were rendered with Gwyddion software [59]. Constant-current and voltage values for the STM simulations have been chosen to match the experimental values.

The Climbing Image−Nudged Elastic Band (CI−NEB) method [60] was employed to simulate the cross coupling process at the Ag(110)-c(2×2) surface, generating the minimum energy path of the reaction step and an evaluation of the energy barrier.

3.3 SAMPLE PREPARATION (ORGANIC THIN FILMS/MOLECULAR SELF-ASSEMBLY)

Even though conditions vary from experiment to experiment, the general preparation procedure remains the same: after cleaning the Ag substrate, the precursor molecules are sublimated in UHV and the self-assembled layer is step-annealed up to induce desorption or polymerization of the adsorbates. Eventually, exposure to O2 in controlled conditions may be performed. Before going into details in each of these steps, I mention briefly how the molecules are synthesised.

3.3.1 Synthesis and preparation of molecular precursors

For my experiments I used three precursors molecules: 1,6-dibromopyrene (Chemical formula – DBP in the following), the dibrominated Pd-cyclometallated complex [(5-bromo-2-phenylpyridine)Pd(μ-Cl)]$_2$ (Chemical formula - CyPd in the following) and the same corresponding hydrogenated complex (Chemical formula – CyPd_2 in the following). All the molecules were synthesized by Prof. Antonio Papagni and Dr. Luca Vaghi at Universita di Milano-Biccoca. Their structures are shown in Figure 21. In the appendix,

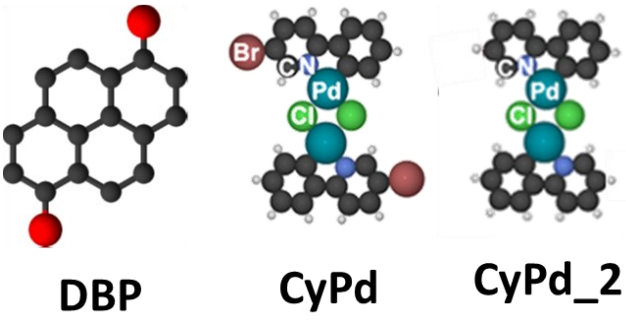

Figure 21 the molecules that serve as precursors for the different nanostructures and self-assemblies described in this dissertation.

1,6 BDP was synthesized using the procedure described in ref. [23]. In brief, 1,6 DBP is commercially available, but it was synthesized via direct bromination of pyrene [61]. Slow addition of bromine (1 ml, 19.5 mmol) in CHCl3 (50 ml) to a solution of pyrene (2 g, 9.9 mmol) in CHCl3 (50 ml) produced a 1,6 and 1,8 dibromo isomeric mixture from which pure 1,6-dibromopyrene was obtained by fractional crystallization from xylene (0.97 g, 27%). Physical and spectroscopic data are in line with a 1,6-dibromopyrene commercial sample.

CyPd, was synthesized according to the procedure of Yian Shi et al. (Peng 2011): $PdCl_2$ was reacted with a slight excess (1:1.05) of 5-bromo-2-phenylpyridine in $CHCl_3$, at a temperature of 100 °C (sealed tube, inert atmosphere) for 24 h. The precipitate was filtered and washed several times with $CHCl_3$ to obtain pure **CyPd** as a highly insoluble yellow powder.

Before their first use, precursor molecules are carefully outgassed in UHV though a differential pumping system and then into the preparation chamber, until a base pressure better than 10^{-8} mbar was achieved with the molecules at the chosen sublimation temperature (Tsub). Tsub is chosen significantly lower that the dissociation temperature of the corresponding compound, determined by TGA, in order to guarantee a reasonable flux without breaking the molecules.

3.3.2 Clean sample preparation

The samples were prepared *in situ* in each experimental chamber. The Ag(110) surface was cleaned by cycles of sputtering with noble gas ions (either Ne^+ or Ar^+ with 1 to 3 keV kinetic energy) followed by prolonged annealing to T=550 °C or T ~400 °C for microscopy and photoemission experiments, respectively. Surface cleanliness and order were checked by STM or by XPS and low energy electron diffraction.

3.3.3 Deposition and annealing of organic molecular precursors

The molecules are deposited on the sputtered and annealed Ag(110) substrate at room temperature (RT) (or in some experiments, at T~100 K) for a set amount of time. The system is then annealed to varying temperatures to possibly induce morphological/chemical changes or reactions that alter the system. These changes are observed using the previously mentioned techniques (STM, STS, XPS) and whenever possible, compared against simulations/DFT calculations by our partners in UNIMIB.

conditions

The general protocol for 1,6 DBP are as follows:

I sublimated DBP molecules on Ag(110) at RT from a Tantalum crucible heated to 100 °C under UHV until I obtained a coverage of DBP on Ag(110) of (0.6 ±0.2) ML, as estimated by XPS and STM. I ultimately decided on sub-monolayer coverage in order to have some bare Ag(110) areas after GNRs polymerization. This is a condition that would be preferable both for STS inspection and for better evidencing the effect of O_2 exposure.

After I deposited the DBP on Ag, I annealed the sample stepwise to produce GNRs, following the protocol defined in ref.[23] First, I slowly heated the sample to T=150 °C and kept it at that temperature for 15 minutes. I eventually raised the temperature to 400 °C (350 °C for XPS experiments) for 5 minutes and subsequently cooled the sample down slowly.

Afterwards, I exposed the GNRs to O_2 at RT or 300 °C for 20 minutes at a background pressure $P=1x10^{-6}$ mbar, resulting in a nominal exposure of 900 L. Since I employed a doser, placed at ~2 cm from the sample surface, we estimate a local enhancement of the pressure by approximately a factor of 5 [62].

At each stage of the preparation the sample was cooled down to LN_2 temperature and inserted eventually into the LT-STM for inspection. Conversely, XPS analysis was performed to monitor the evolution of the DBP layer up to GNRs formation.

CyPd and CyPd_2 followed a similar protocol for deposition and annealing.

Sublimation of CyPd was set at 130°C with the clean Ag(110) still at RT. Step-annealing followed with incremental steps from 100 to 450 or 500°C, holding the sample at a given temperature for 5 minutes before proceeding. Final configuration after each step was inspected under STM and XPS just as with the GNRs.

4 GRAPHENE NANORIBBONS FROM 1,6 DIBROMOPYRENE

In this chapter I will describe my activity on the characterization of GNRs and on their interaction with Oxygen. The research group I joined had already found a protocol for the growth of extended arrays of GNRs as mentioned previously, but the attention was focussed on forming ordered patterns starting from the deposition of multilayer DBP at Ag(110). You prosecuted that work starting from preliminary measurement of DBP deposition in the sub-ML regime.

DBP/Ag(110) at RT

????

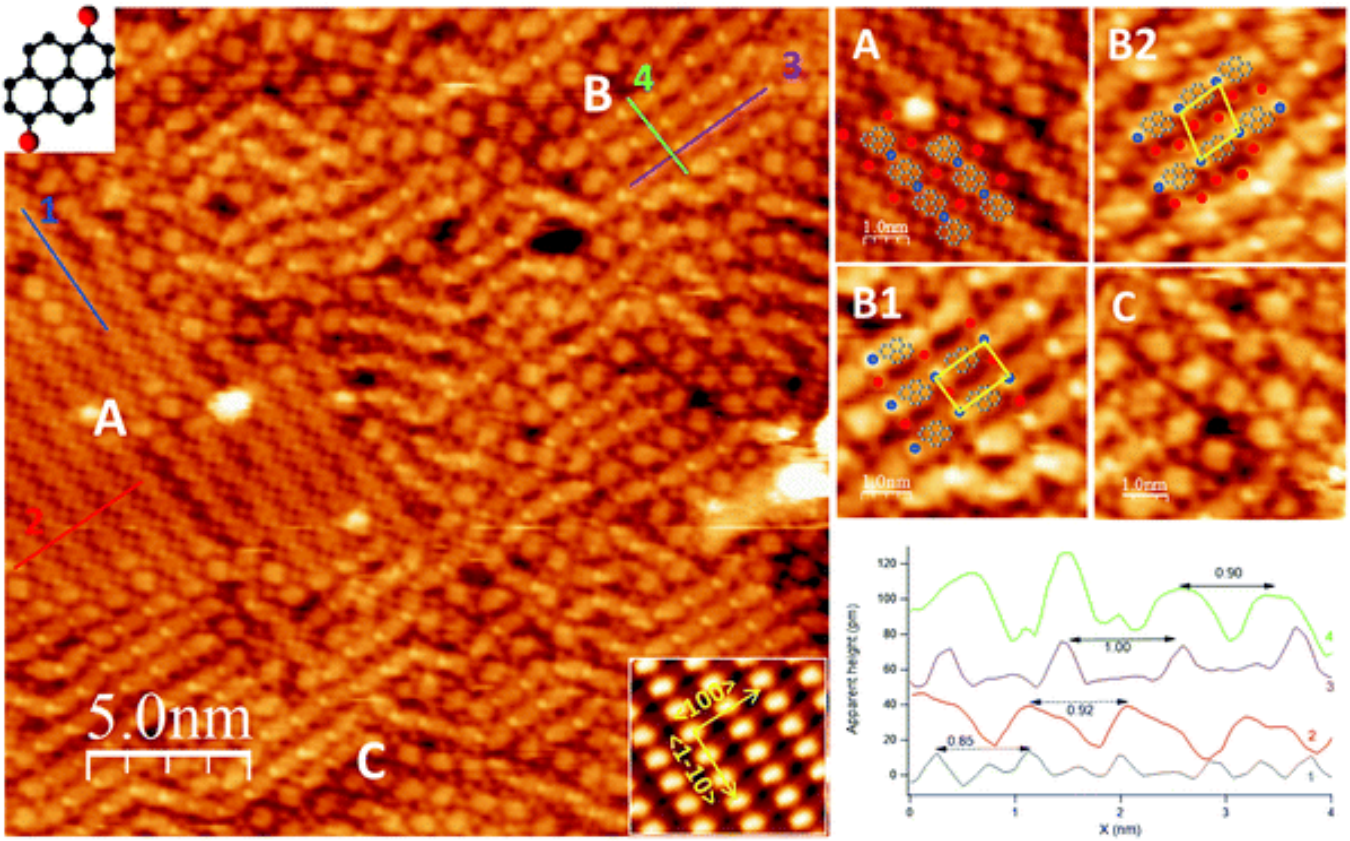

Figure 22. Left: STM image (V = −150 meV, I = 0.3 nA) showing the co-existence of three different self-assembled structures (labelled as A, B, C) obtained upon deposition of a sub-monolayer of DBP on Ag(110) at RT. Top and bottom insets recall respectively, the molecular structure of DBP and the atomically resolved image of clean Ag(110) from which the high symmetry directions (marked by arrows) are determined (image size: 1.8 × 1.6 nm^2). Top right: enlarged image of each domain (either from the area in the overview or from neighbouring areas). Among B domains, it is possible to distinguish rectangular (B1) and rhomboidal unit cells (B2). Empirical models deduced from the periodicities of the self-assembled structures and from XPS results are superimposed to the STM image for structures A, B1 and B2 (grey: de-brominated pyrene units; blue: Ag adatoms; red: Br atoms). Bottom right: line scans cut across the paths marked in the overview for structures A and B1 (follow colour code). Line scans drawn along and across the rows of structure B2 are not reported since they do not differ significantly from those of B1. The higher and sharper features in traces 1 and 3 correspond to the Ag atoms within the organometallic chains.

Figure 22 shows that 1,6 DBP molecules self-assembled into domains with different geometries upon sub-monolayer deposition on Ag(110) at RT. These precursor molecules formed large islands comprised of a single layer and tend to cover a whole terrace on the substrate. This behaviour suggests a high degree of mobility of the molecules at RT. I reported relevant measurements of the self-assembled structures in this paper [37]. To summarize, 1,6 DBP sub-ML coverage has three self-assembled structures (A, B, C) each with their own dimensions and features. Structure A consists of rows oriented along the $\langle 1\bar{1}0 \rangle$ direction. Substructures include alternating nearly oval features and small bright dots. Linescans determine periodicities of (8.4 ± 0.9) Å (trace 1, blue) and (9.0 ± 0.4) Å (trace 2, red) along and across the rows, respectively. I estimated a local molecular density of ~1.3 × 10^{14} DBP units per cm^2. These periodicities suggest that each of the large roundish protrusions in the chain consists of one single DBP unit. Structure B also consists of alternating protrusions. The larger protrusion identified as a DBP unit alternates with a smaller but brighter dot as compared with structure A. Unlike structure A, structure B had chains that are oriented at either −35° or 88° off $\langle 1\bar{1}0 \rangle$ and they were rather bent than straight. The less regular geometry causes the DBP units in adjacent rows to be either aligned, giving rise to a rectangular unit cell (assembly B1), or misaligned, resulting in a rhomboidal unit cell (assembly B2). Structure B has an average periodicity of (9.9 ± 0.5) Å along the

rows (trace 3, violet) and (8.7 ± 0.5) Å across the rows (trace 4, green), corresponding to a local molecular density of ~1.2×10^{14} DBP units per cm^2.

Corresponding XPS measurements provided additional information on the chemical nature of the self-assembled DBP layer and proof of subsequent formation of the GNRs. The presence of a $E_b(Br\ 3d_{5/2})$ = 68.2 eV and 70.4 eV along with evidence of a C-Ag peak in the C1s spectra at RT, indicates partial debromination of DBP and Br atoms bound to Ag (Figure 23). Figure 23 suggest an almost complete debromination of the molecules on the surface and formation of a stable organometallic intermediate. The rest of the XPS information helped corroborate the morphology we observed when forming the GNRs. Specifically, it helped determine the nature of the small bright features present in and in-between the rows. Comparing with what was observed for a DBP multilayer annealed to 150 °C,[23] I proposed that the de-brominated molecules form organometallic chains with Ag adatoms provided by the surface, most probably released from the step edges,[63] while dissociated Br atoms sit in-between these chains. I proposed the empirical models superimposed to the enlargements in Figure 22: the bright dots in the chains are Ag atoms (blue circles) bound to the pyrene groups to form organometallic proto-polymers and the Br atoms occupy interstitial sites in-between the rows (red circles).

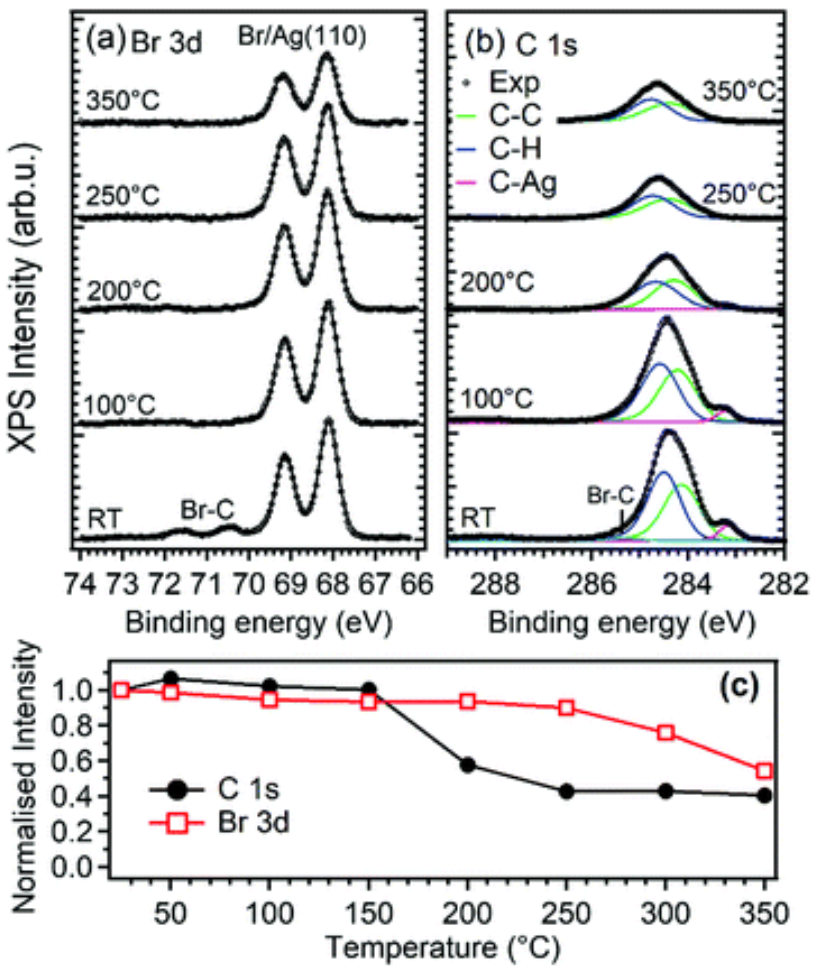

altri spettri xps in letteratura per confronto?

Figure 23. (a) Br 3d and (b) C 1s core level spectra of 0.6 ML of DBP deposited on Ag(110) at RT and after annealing the sample to the indicated temperature for 5 min. (c) Normalized integrated intensity of Br 3d and C 1s peaks as a function of temperature. The intensities are normalized to the peak areas measured after the deposition.

4.1 CHARACTERIZATION OF GNRS

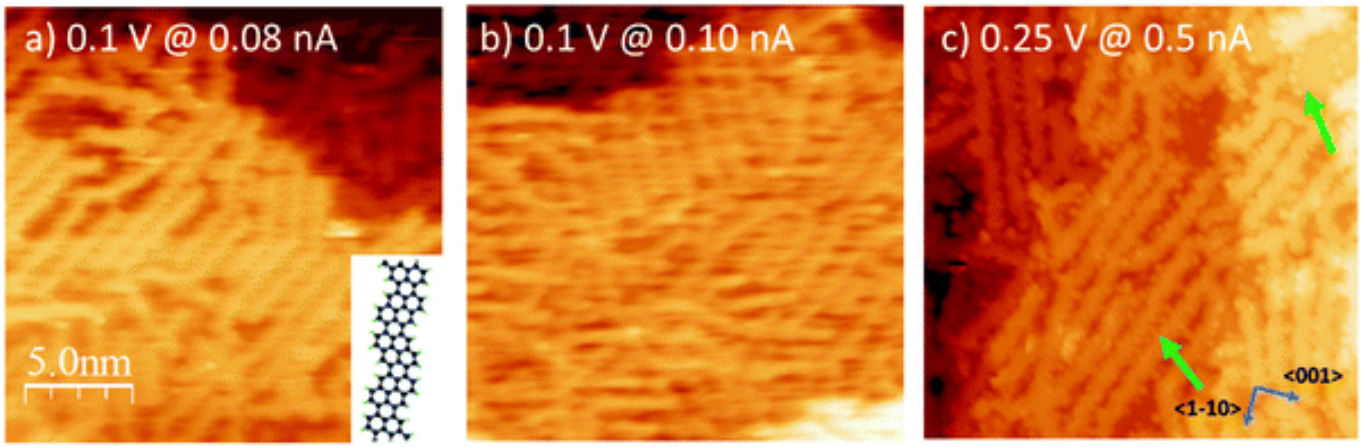

Figure 24. STM images showing overviews of the Ag(110) surface covered by a sub-monolayer of GNRs and subject to different treatments: (a) pristine GNRs; (b) same as (a) after exposure to O2 at room temperature; (c) same as (a) after exposure to O2 at 300 °C. The nominal O_2 dose is always 900 L (~4500 L when considering the doser enhancement factor). The green arrows in (c) point to additional features forming both in-between the GNRs and on bare Ag(110) areas.

As for the formation of the nanoribbons, the step annealing also shown with the XPS in Figure 23 induces the polymerization of the pyrene "monomers" and along with subsequent dehydrogenation forms the GNRs. In short, we are talking advantage of a surface-assisted Ullmann coupling reaction.[64] First, I observed complete debromination of the DBP upon annealing at 100°C. The most obvious chemical change happens between 200 and 250°C where I observe the disappearance of the C-Ag peak as well as a shift in the main C1s peak towards higher binding energy. These changes indicate transformations in the interaction between the molecules and the substrate and a chemical transformation, specifically an early indication of the polymerization process.[23,37] The final ordered arrangement is achieved after annealing the sample to 400°C for 5 minutes. At high temperatures hydrogen is liberated in the process of polymerization and escapes with the bromine as HBr as seen in the decrease of Br in increasing sample temperature.

Br può diluirsi dentro l'Ag???

Inspection of the GNRs by STM show that the nanoribbons arrange at the surface parallel to each other as seen in Figure 24a. The GNRs synthesized from DBP by surface assisted polymerization are very narrow (~1.0 nm) and have a peculiar edge-site sequence, which alternates two zigzag and one armchair site. [23,37] The estimated reduction of molecules on the surface with respect to the initial DBP coverage is smaller in STM images than what is suggested from XPS, but this is probably related to the slightly different heating rate in the two experiments or to the uncertainty (0.6 ± 0.2 ML) in the initial DBP coverage. Aggregation of the nanoribbons into local ordered clusters can also induce some overestimation of the coverage by STM. The overall degree of order on the surface is lower than for the case in which GNRs were produced starting from a DBP multilayer.[23] The less packed arrangement of the GNRs, however, could facilitate the intercalation of O_2, which are the goals of the present experiment. In addition, having some bare Ag(110) areas is preferable when performing STS measurements because I can then directly measure a clean spectrum on the same experiment.

manca la scala

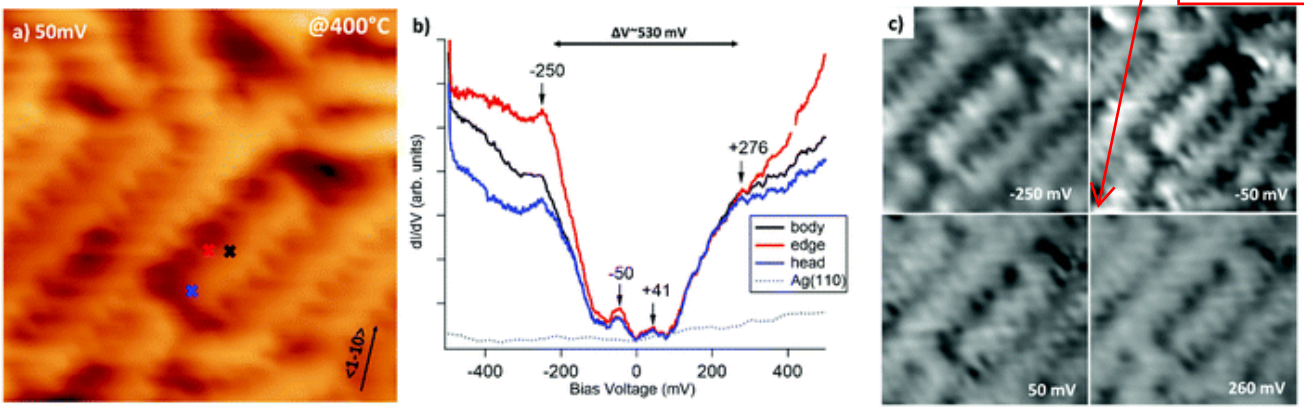

Figure 25.STS and dI/dV map of pristine GNRs in the bias range from −500 mV to 500 mV. (a) Topographical image (image size: 7.0 × 7.0 nm2, V = 50 mV, I = 0.02 nA); crosses indicate the sites where point spectra were recorded. (b) Differential conductance spectra recorded at the points marked in (a). The corresponding spectrum recorded on clean Ag(110) is reported for comparison. A band gap of ~530 meV was observed throughout the GNR. Localized states at −50 meV and +41 meV are present within the gap. Such values were measured reproducibly for 3–5 nm long GNRs; it is out of the scope of this work to determine a possible length dependence of the energy gap. (c) dI/dV maps taken at selected bias voltage suggested by the STS spectra.

I also reported that the GNRs have an electronic band gap of $\Delta V \sim 530$ mV centered around Fermi level and the presence of weak states inside the gap (-50 and +41 mV).[37] Figure 25 shows the morphology of the GNRs at sub ML coverage (left) with the corresponding spectra (center) and dI/dV maps (right) taken at the energies corresponding to the observed states in the gap. It should be noted that the measured energy band gap is relatively small, but it falls well within the expected range for GNRs. [27,34] I mention that, although some trends suggesting a correlation between the gap opening and the GNR width have been determined, they refer essentially to armchair GNRs (AGNRs). Much less information is available for nanostructures with different edges.

ZGNR mai definito

Identifying the nature of the states within the gap, especially the one at −50 meV, on the contrary, is not straightforward. On the one hand, the presence of edge states is usually associated to ZGNRs, and our nanostructures present a periodic edge site sequence in which two zig-zag sites alternate to one armchair; therefore, the almost regular spacing of the brighter spots may correspond to the location of zig-zag sites along the edges and at the heads of the GNR. On the other hand, edge sites should vanish, or at least attenuate, on the axis of the nanoribbon. However, there are no significant differences in the spectra taken at the centre (black trace), at the head (blue trace) and at the border (red trace) of the nanostructure, except that the rise of the LDOS seems to be steeper in the last case. In addition, the bright spots associated to the −50 meV state in the dI/dV maps do not seem to be localized at the edge but rather to be spread across the whole GNR width. Hence, an alternative explanation is that the −50 meV intensity is related to a localized state due to quantum confinement along the GNR long axis. Though a more thorough statistic is necessary to confirm this hypothesis, I mention that, in the ultra-narrow limit, hints are present that the gap size can be affected also by the ribbon length.

4.2 Oxygen exposure on GNRs

After studying the GNRs I synthesized previously in ideal conditions, it is important for us to also investigate the stability of the molecules closer to ambient conditions due to some potential applications like in devices. For this purpose, as a first step I exposed the GNRs in oxygen as a model reactive gas in controlled conditions. I want to understand if their characteristics are modified by their interaction with oxygen. It is also interesting to understand if small molecules can intercalate below the GNRs. This is a phenomenon already observed supported graphene monolayers,[[65,66]] The possibility of intercalation between the GNRs and the substrate might allow for the non-destructive

decoupling of the nanoribbons from the substrate. As mentioned previously, I began by exposing the Ag(110) surface covered by a sub-monolayer of GNRs (Figure 26a) to O_2 at RT (Figure 26b) or at 300 °C (Figure 26c) in the 10^{-6} mbar pressure range for 20 minutes. Considering that I use a doser, which makes the effective pressure at the sample larger than the background pressure, I estimate for all experiments an oxygen exposure of at least 900 L. Oxygen was chosen since it is one of the most reactive and abundant gases in air and because it is known to affect the growth of armchair GNRs if present in the UHV chamber above a critical pressure.[[40]] Heating the system to 300 °C was done in order to promote the mobility of the adsorbate while leaving the structure of the GNRs intact (they were produced at T = 400 °C and prolonged annealing leads only to a reduction in the coverage, without changes in the morphology of the GNRs). Any changes in the surface morphology are therefore due to the presence of the reactant and not to the effect of prolonged annealing.

STM experiments are reported in the overviews of Figure 24 and in the enlargements of Figure 26. By comparing the morphology of the GNRs/Ag(110) surface upon the different treatments, I observed some notable effects. Oxygen exposure at RT seems to induce some disorder in the ordered arrays of nanoribbons, which now show little preferential orientation on the surface. I did not observe additional features that can be related to oxygen adsorption but the lower stability of the tip and the worse quality of the images (see also enlarged image in Figure 26b) suggest that oxygen must be present on the surface and possibly functionalizing the tip. This is coherent with the XPS information presented in Figure 28. More peculiar morphological changes are observed after dosing oxygen while keeping the system at 300 °C. Besides the GNRs, several small round features (indicated by the arrows in Figure 24) are now present at the surface as seen in the STM image Figure 24 and in the enlargement reported in Figure 26, either in-between adjacent nanostructures or on bare Ag areas, where they organize in short rows. Similar features were also observed for the full monolayer of pristine GNRs in between the nanoribbons but not for the sub-monolayer preparation of Figure 24. In that case, they were identified as residual Br and Ag adatoms deriving from the thermal dissolution of the organometallic chains.[23]since the Ag adatoms failed to migrate back to the step edges of the Ag(110) planes due to the compact arrangement of the GNRs. This constraint is apparently removed for the less dense sub-monolayer. Upon oxygen exposure at 300 °C, the small bright dots are more abundant than they were on the full monolayer of pristine GNRs.[23] They are randomly distributed along the edges of the nanostructures as well as on clean areas of the substrate away from any nanoribbons. Therefore, such bright dots with Ag-containing features seems to be stabilized at the surface by the presence of oxygen. Indeed Ag is prone to react with oxygen to form a wide zoology of Ag–O complexes.[63,67] The height profile of the isolated dots (not shown) protrudes by ~0.4 Å from the bare Ag plane. It also has a shape similar to the one of O–Ag–O added rows and this suggests that the observed protrusions consist of Ag and O adatoms.

seem

many different
Ag-O complexes

manca la scala

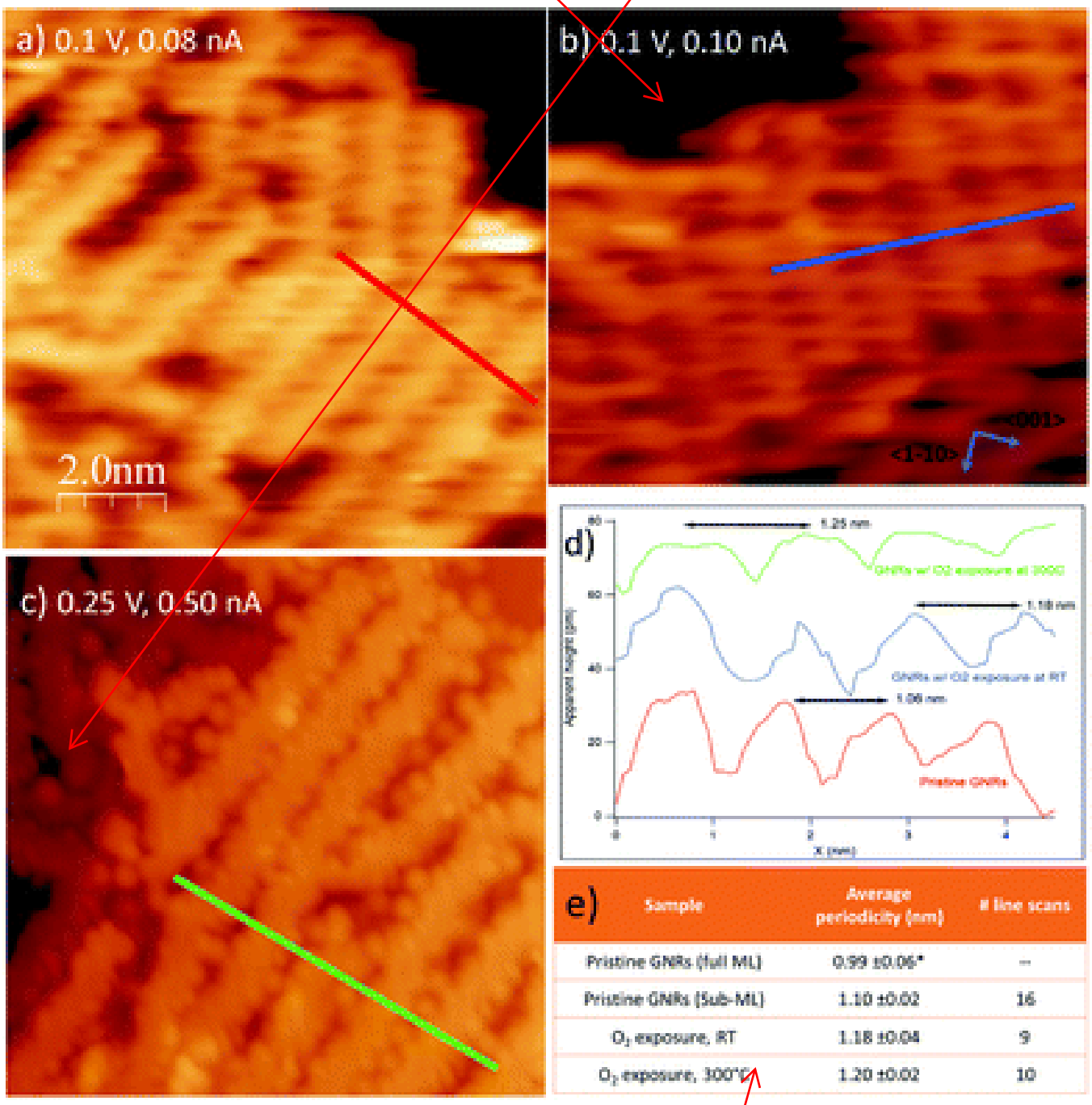

*Figure 26. Close up images of the three preparations in Figure 24 with corresponding line scans indicating the periodicity of the GNRs. (A) Pristine GNRs; (b) same as (a) after exposure to O2 at RT; (c) same as (a) after exposure to O2 at 300 °C. In this preparation the small features in-between the GNRs are evident. (d) Line scans cut along the paths marked in panels (a–c) showing that the separation between adjacent GNRs increases after o2 exposure. (e) Table summarizing the average separation between GNRs in ordered arrays, together with the number of line scans considered for each preparation (corresponding to the number of GNRs arrays considered). Values are given with their standard error. Data indicated with * are taken from ref.*[23]

molto sgranata - non si legge

Finally, I focused on the small arrays of parallel GNRs, which are present for all the three preparations reported in Figure 26 and I measured the separation or periodicity between adjacent GNRs. Line scans drawn along the paths marked in panels (a–c) (perpendicular to the long direction of the nanoribbons) are reported in panel (d). The table in panel (e) summarizes the outcome of a statistical analysis over several ordered arrays. The corresponding measured value for full monolayer coverage is also reported for comparison. [23] Firstly, the GNRs tend to form arrays even at sub-monolayer coverage, though less densely packed than for the full monolayer coverage.[23] The distance between adjacent nanostructures further increases upon oxygen exposure. Line scans present a less regular profile (the

distance between maxima is not always the same, as seen with the more disordered distribution and orientation of the nanoribbons). The spacing on average between adjacent structures increases by ~10% with respect to the pristine sample. I remark that this effect must be due to oxygen exposure. In fact, the samples in Figure 24b, c and Figure 26b, c were obtained by exposing the pristine sample of Figure 24a and Figure 26a, so that the initial density of GNRs is the same. The larger separation between adjacent nanoribbons upon oxygen adsorption suggests that the O adatoms adsorbed on the first Ag layer or the O–Ag–O complexes act as "spacers". It also indicates that, following oxygen exposure, the bonding of the nanostructure to the substrate gets weaker and the GNRs can displace along the surface without changing their geometry. Whether or not this is only due to repulsion by the presence of the additional adatoms or a more significant interaction (chemical reaction) is explored in the corresponding XPS experiments.

STS spectra could have also been extremely useful to determine if these morphological changes affect the width of the band-gap or its position with respect to the Fermi edge but, unfortunately, I was unable to record them with a useful signal-to-noise ratio due to the instability of the tip for samples exposed to oxygen as mentioned earlier. However, dI/dV maps could be acquired in the bias range $-1.0\ \mathrm{V} < V < +1.0\ \mathrm{V}$ after dosing O_2 at 300 °C.

Figure 27 shows a comparison between dI/dV maps recorded near the band-gap edges for the pristine GNRs sample and for the same sample after exposure to O_2 at 300 °C. There appears to be a contrast change between positive (empty states) and negative (filled states) bias for the pristine GNRs. At −250 mV, the nanostructures appear narrower, and the measured corrugation is larger than at +250 mV. This effect is less pronounced after exposure to O_2. In the case of oxygen exposure, the images appear very similar in contrast and the small differences at the edges are a consequence of the derivative operation. In addition, the nanostructures appear wider, and their edges are much better defined than on the pristine surface. The effect goes well beyond the improved quality of the tip in this image. This change in local density suggest a reaction of the nanoribbons with oxygen. It is possible that interacting with oxygen causes a better confinement of electrons within the GNR. This hypothesis (O_2 reacting with the GNRs) would be corroborated in the XPS findings discussed in the next section.

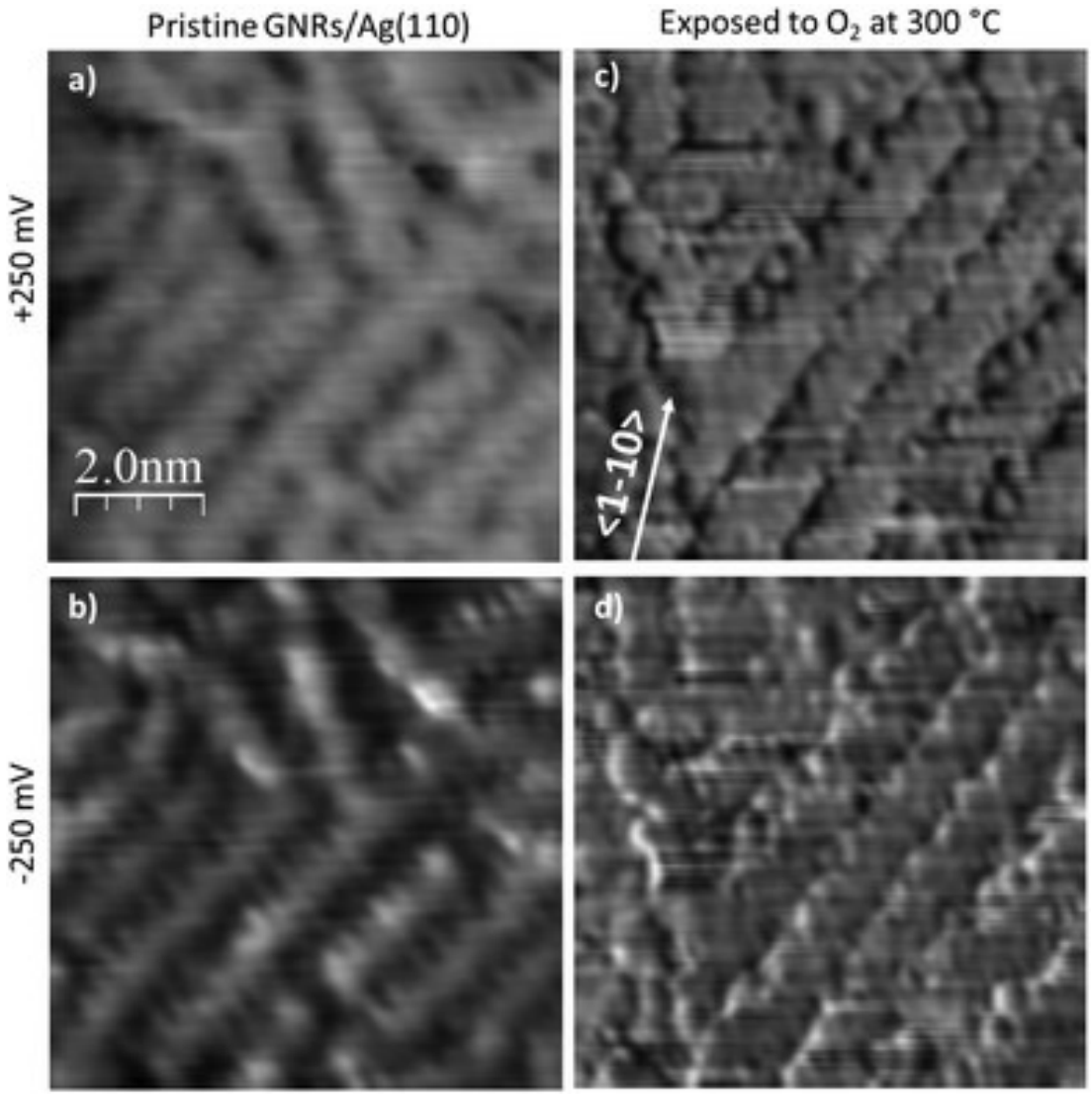

Figure 27. Comparison of the dI/dV maps of GNRs pristine and after exposure to oxygen at 300 °C. Bias voltages corresponding to the edges of the energy gap measured for the pristine sample are presented. The corresponding topographical images are those of Figure 25a and Figure 26c. Z-scale is the same for all images.

meglio ripetere
chi è a), b), c), d)

Finally, I mention that previous literature on AGNRs reports that the nanostructures are affected by the presence of gases (water or oxygen) during the surface assisted synthesis[40] but that, if grown under clean UHV conditions, their properties are stable even at atmospheric pressure.[39] Our results are not in contradiction with these works since they refer to the morphology of the GNRs, which is also preserved in our case, while they did not perform any XPS analysis on the investigated systems.

XPS spectra of C 1s and O 1s regions recorded for the GNRs/Ag(110) system before and after O_2 exposure are reported in Figure 28. It should be noted that these spectra were recorded with a conventional X-ray source and therefore the resolution is lower than the one of the spectra of Figure 23 which were taken with synchrotron radiation. For this reason, the major C 1s signal was presented as a convolution of the C–C and C–H peaks and fitted as only one component. After synthesis of the GNRs, the C 1s spectrum is compatible with the one of Figure 23, while the O 1s region is completely flat. After exposure to O_2 at RT, a minor component at 287.4 eV appears in the C 1s spectrum while the main C1s line downshifts by 0.25 eV. A similar downshift upon oxygen intercalation has already been observed for 2D graphene layers on Ir(111)[68] and on polycrystalline Cu,[69] while a coherent increase in the work function was measured for graphene on Ru(0001).[70] The effect is interpreted

a 300 C il segnale del carbonio GNR cala drammaticamente, mentre quello dell'O quasi no. Il segnale O1s cambia poco, anche nei rapporti relativi. Quindi pare che quasi tutto l'ossigeno rimanga attaccato all'Ag o intrappolato sotto i pochi GNR rimasti e che aiuti a non far desorbire i GNRs ?

as evidence of the graphene layer detaching from the substrate. This lowers the graphene–substrate interaction and thus leads to a reduction of the n-doping induced by the presence of the metal substrate. The O 1s signal can be fitted with two components at 529.9 and 531.2 eV. The former can be assigned to oxygen adatoms on Ag. This is expected considering the sticking probability for dissociative adsorption of O_2 on Ag(110) at RT (0.1%),[71], the presence of bare areas of the sample and the large oxygen exposure I performed. On the other hand, the peaks at 287.4 and 531.2 eV are compatible with the formation of C–O bonds [72–75]. This suggests that some interaction occurs between the dissociated oxygen atoms and the GNRs. A reaction between oxygen atoms with pyrene compounds, especially in presence of a metal substrate, is possible and may lead to different oxygenated pyrene species, such as pyrene containing hydroxyl, carbonyl or epoxy functionalities. This phenomenon extends to larger carbon nanostructures as documented here [38] on the stability of 3,1 GNRs derived from DBBA when exposed to air. The formation of carbonyl groups is the most probable outcome from the observed binding energies. Additional O_2 exposure at 300 °C causes a reduction of the C1s signal, indicating partial desorption of the nanostructures, and a relative increase of the high E_b components both in the C 1s and O 1s regions.

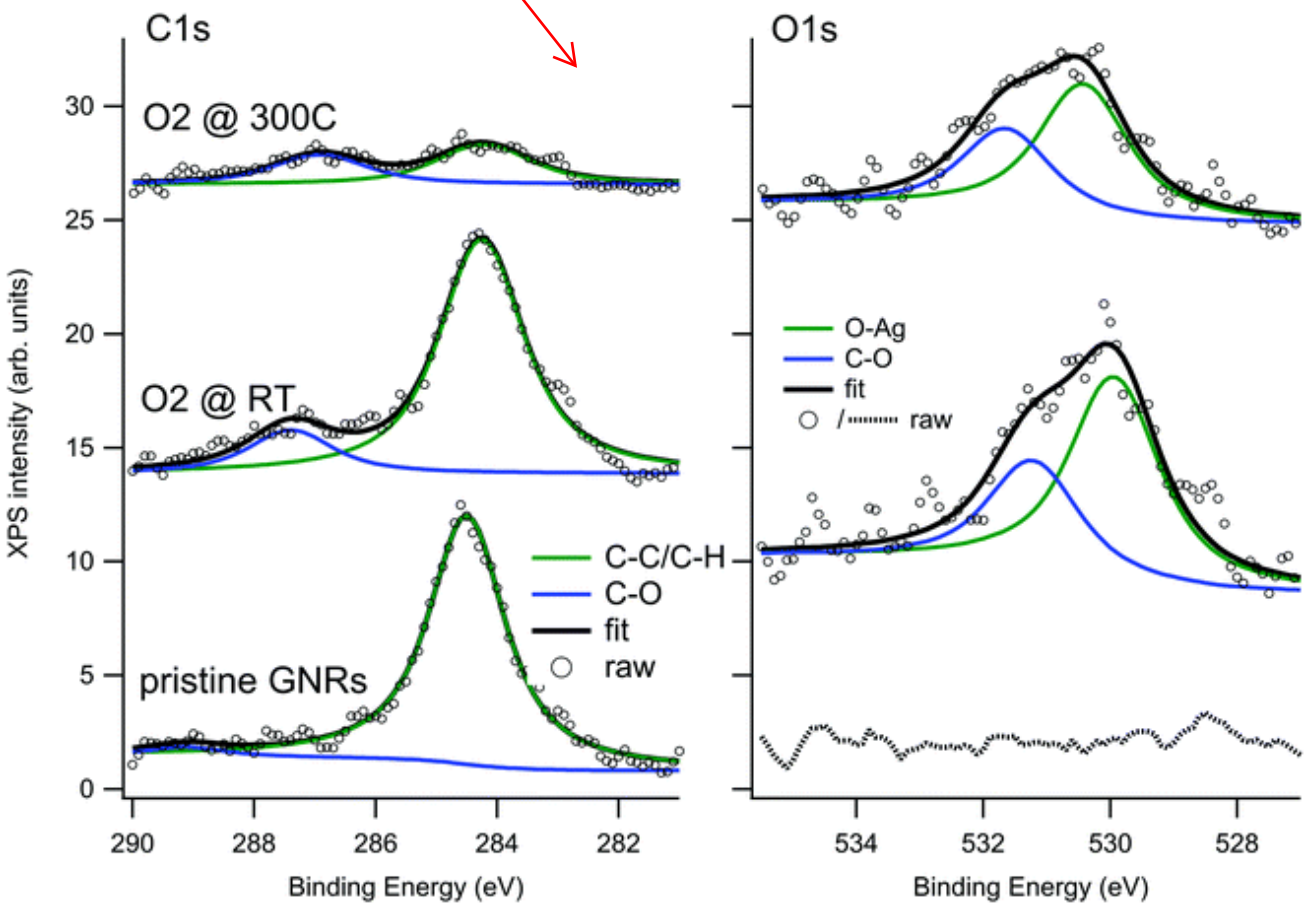

Figure 28. XPS spectra of the C 1s (left) and O 1s (right) regions recorded on the GNRs/Ag(110) surface before and after O2 exposure.

Given the observed changes in morphology in STM and evidence of reactions by the GNRs and oxygen, it is reasonable to state that this raises concerns over the stability of the GNRs in harsher, more realistic conditions. This will have to be taken into consideration when we eventually devise practical applications for the GNRs in the future.

5 Pd-cyclometallated complex [(5-bromo-2-phenylpyridine)Pd(*m*-Cl)]$_2$ (CyPd) on Ag(110)

After investigating simpler graphene nanostructures as the graphene nanoribbons discussed in the previous chapter, the natural evolution of my research is to investigate more complex and suitably doped C-based networks. As explained in the introduction, quite a lot of work is available in the literature for C-based nanostructures doped with non-metal atoms [refs]. Viceversa, much less information is available on doping with transition metal atoms, though interesting properties are predicted by theory for these systems both for catalysis and sensoristic. Therefore I focused my attention on the possibility to produce TM-doped C-based networks starting from a precursor molecule already containing the metallic element. Here I present my findings for the Pd-cyclometallated complex [(5-bromo-2-phenylpyridine)Pd(μ-Cl)]$_2$ deposited on Ag(110). I recall that I had both the di-brominated and the hydrogenated version of the same compound available. The choice of starting with the former one is due to the tendency of aromatic hydrocarbon complexed to dehalogenate due to the interaction with the surface [ref] and hence to make C-bonds available for the formation of organometallic structures and/or for polymerization.
The chemical characterization obtained by XPS is complemented by STM analysis of morphology of the self-assembled structures and by some DFT calculations which validate the models proposed.

5.1 XPS Results for CyPd on Ag(110)

che risoluzione?

sistemare la frase

I begin my analysis of CyPd on Ag(110) by investigating the chemistry of the system using high-resolution XPS. Figure 29 shows the Br 3d (panel a) and C 1s (panel b) spectra recorded during a **CyPd** uptake on Ag(110) at RT, i.e. following incremental doses of CyPd on the substrate. The total C 1s and Br 3d areas are reported in panel c and show that saturation coverage was reached after 8 minutes as the dose, as the signal intensity did not increase significantly from 4 to 8 minutes of dosing. According to the STM information that I will discuss in the following, saturation coverage at RT corresponds to a full CyPd monolayer (ML). Rounding out the chemical information of CyPd/Ag(110), figure 3 shows the N 1s, C 1s, Cl 2p and Br 3d regions for the full **CyPd** monolayer of Figure 2 (bottom traces) and their evolution upon annealing to 150 °C (top traces). I also report I outcome of the fitting procedure that reveals the different components contributing to each spectrum.

???

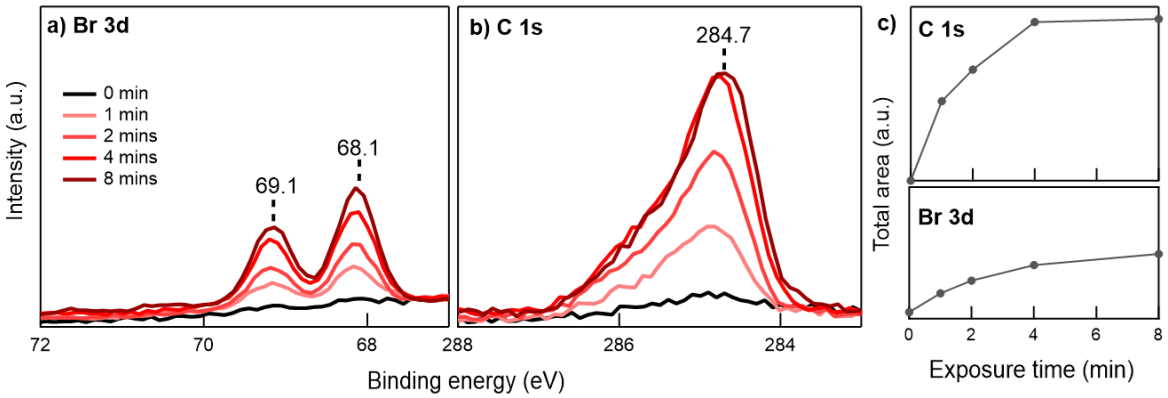

*Figure 29. XPS spectra of a) Br 3d and b) C 1s regions for the Ag(110) surface clean (black trace) and after increasing exposure of **CyPd** at RT (red traces). c) Total C 1s and Br 3d areas vs exposure time.*

photon energy???

Only one doublet is present in the Br 3d region at E_b(Br $3d_{5/2}$)=68.1 eV, i.e. at a binding energy corresponding to Br atoms bound to Ag. On the contrary, no traces of Br-C bonds appear around 70 eV [23,76]. This behavior was already evident at the smallest dose. This indicates that full debromination of **CyPd** already occurs on Ag(110) at RT, consistent with what was observed for DBP/Ag(110) and for other halogenated aromatic hydrocarbon species [23,54,77].

The Cl 2p spectrum, characterized by a doublet with E_b(Cl $2p_{3/2}$)=197.6 eV, is less conclusive since this binding energy is suitable for Cl atoms bound to a transition metITM) therefore either Pd or Ag [78] in the context of CyPd on Ag(110). Because it can be either Pd or Ag, it is not possible to determine from XPS spectra if Cl atoms remain bound to the molecule or if they dissociate upon adsorption.

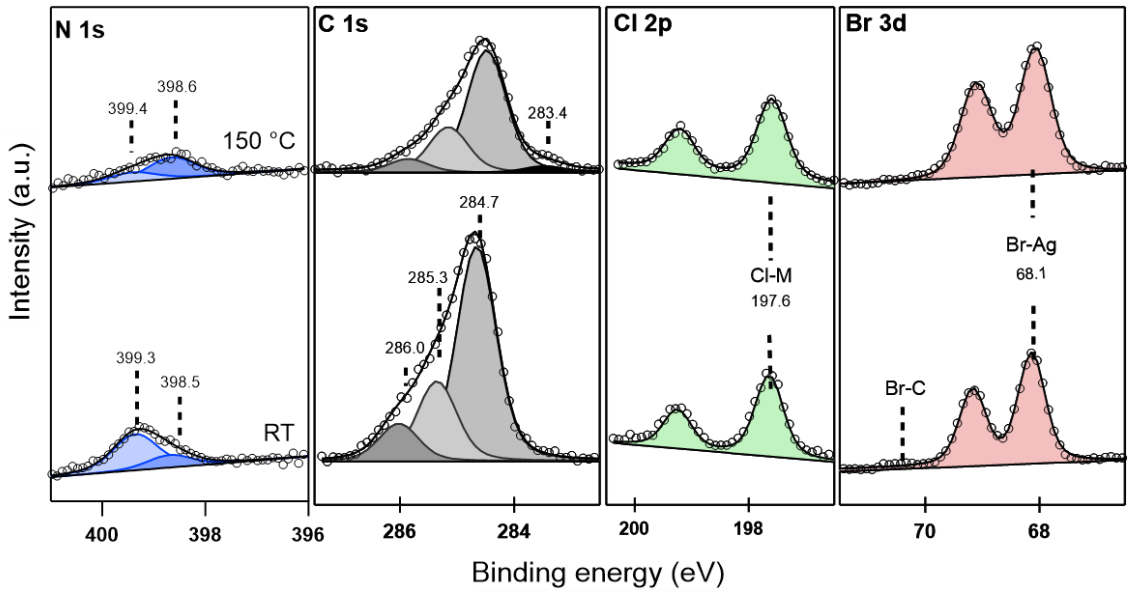

*Figure 30. XPS spectra of C 1s, N 1s, Cl 2p and Br 3d regions recorded for **CyPd**/Ag(110) at RT and saturation coverage and after 5 min step-annealing up to 150 °C (upshifted for sake of clarity). The outcome of the fitting procedure and the different components identified are reported in each region.*

photon energy?

The C 1s spectrum observed at RT is quite complex and has a strongly asymmetric shape already at the smallest coverage of CyPd. It clearly indicates the presence of multiple components corresponding to C atoms in different chemical environments. The main line at E_b=284.7 is assigned to the unresolved

contributions of sp^2C atoms (C–C component) and C-H bound carbon atoms [23,54]. The components at E_b=285.3 eV and 286.0 eV are in the range suitable for C-N bonds [79].

The N 1s spectrum at RT shows a single feature, which can be resolved into two components: a main one at 399.4 eV and minor one at 398.6 eV. Previous papers [80] suggest that both species are suitable for pyridinic nitrogen, though their assignment is not straightforward. They could be assigned to N atoms with a slightly different interaction with the Ag substrate. An E_b value corresponding to the higher energy component was observed for bi-isonicotinic acid on Ag(111) and attributed to nitrogen atoms weakly interacting with the substrate [81]. The lower energy component one the other hand is compatible with the signal measured in N-doped graphene on Ni(111) [82] and may therefore indicate a stronger interaction with the substrate and possibly N-Ag bond formation.

After characterizing the CyPd/Ag(110) system at RT, I investigated its thermal evolution to check if any polymerization occurs, as it was the case for DBP. Spectra were taken after heating the, up to a maximum temperature of 500°C, i.e., until almost complete desorption of the adsorbate.

The top spectra in Figure 30 show the modification to the XPS spectra observed upon annealing to 150 °C. Heating up the sample to this T caused the desorption of the aromatic part of the molecule. This is indicated by a ~40% decrease of the C 1s and N 1s intensity. In the C 1s region, I observed a small downshift of ~0.1 eV in E_b and the appearance of a small additional component at 283.4 eV. This could be because of some segregation of C induced by the annealing process or by the formation of additional Ag-C bonds. In this latter case, they should be different from those already formed at RT upon debromination. On the other hand, the intensity ratio of the two components in the N1s region gets inverted. This suggests that the amount of N atoms interacting more strongly with Ag increases slightly though the overall coverage decreases with annealing. However, as I will discuss later, the change in the N 1s spectrum is not fully reflected in the geometry of the self-assembled overlayer, that shows only minor changes upon annealing to 150 °C. Finally, annealing does not cause significant changes for Cl 2p and Br 3d regions, suggesting that the halogen atoms would remain stable on the surface.

In a different preparation I followed the thermal evolution of CyPd/Ag(110) up to 500 °C. As shown Figure 31, the spectra at RT are perfectly equivalent to those discussed in Figure 30. I notice that the C 1s and N 1s intensity already drop from the first annealing steps, while the Cl and Br signals remain stable till 300 °C and 450 °C (spectrum not shown), respectively. To better visualize the thermal evolution of the CyPd/Ag(110) system, I took the Br 3d signal as a reference and plotted the C/Br, N/Br and Cl/Br area ratio in the bottom panel of Figure 31. Since I am interested in comparing the behavior of the different elemental constituents of CyPd and not in their absolute values, all the traces are further normalized to the value at RT. The graph shows that C and N have the same behavior: their intensity reduces to less than 40% of the original value when CyPd is annealed from RT to 200°C, indicating partial desorption of the organic part of the CyPd molecule. Then the peak areas remain almost stable while the peaks broaden and downshift in binding energy. I associate the residual C 1s and N 1s intensity to a degradation of the remaining Phe-Pyr units. The phenyl and/or pyridine rings would break and smaller fragments bind to the Ag surface. On the contrary, the Cl and Br intensity is stable up to much higher temperatures. Br remains on the surface over the full annealing range, while the Cl intensity drops above 300°C.

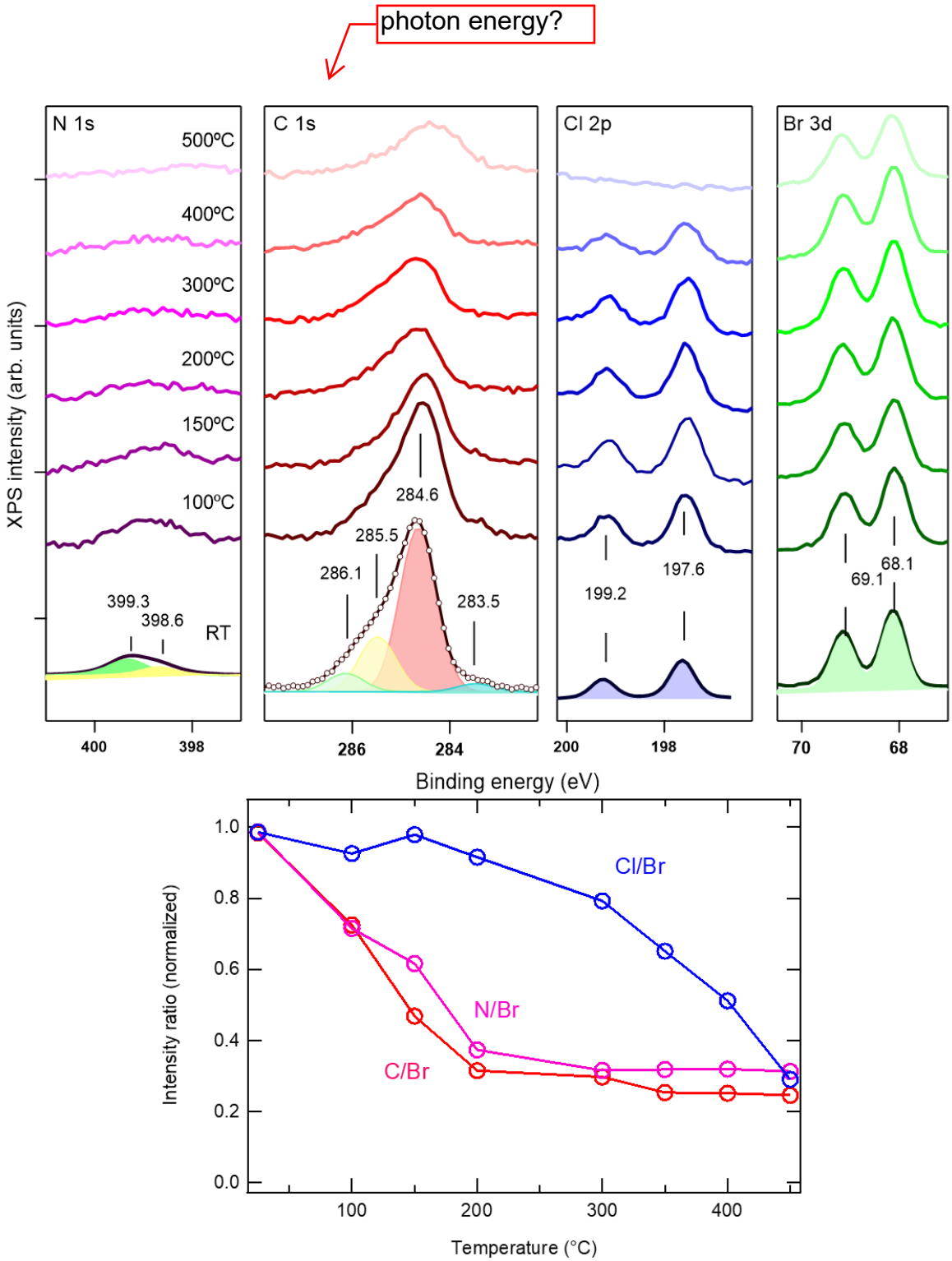

Figure 31. Top: Photoemission core level spectra of N 1s (purple), C 1s (red), Cl 2p (blue) and Br 3d (green) lines for the CyPd/Ag(110) system obtained upon 24 minutes of deposition at RT and following step-annealing up to 500 °C. Traces are normalized to the background of the corresponding spectrum recorded for clean Ag(110) (not shown) and upshifted for sake of clarity. hv = 515 eV, pass energy = 25 eV. Bottom: Thermal behavior of the C 1s, N 1s and Cl 2p lines. For a better visualization and to avoid systematic errors, the total C 1s, N 1s and Cl 2p areas are normalized to the corresponding Br 3d signal (assumed as constant) and to the value at RT.

Considering the small dimensions of Cl and the higher desorption temperatures reported in literature [83], I suppose that some diffusion into the bulk may occur for the initial reduction of intensity. The overall higher thermal stability of halogen species indicates that the interaction with the substrate is stronger for the halogen atoms than for the organic fragments. I also want to mention that at RT, C:Br, C:Cl and C:N ratios are close to the stoichiometric value of 11:1, though there is a slight deficiency in C as seen in the table below [84].

	C:N	Cl:N	Br:N	Br:Cl
Expected ratio	*11*	*1*	*1*	*1*
Expt. A (uptake)	*7.89*	*0.81*	*0.84*	*1.04*
Expt. B (thermal evolution)	*7.86*	*0.79*	*0.77*	*0.97*

Table 2.Stoichiometric ratios of elements for CyPd. Reported values here correspond to the saturation coverage at RT for both experiments.

The CyPd elemental constituent that I haven't mentioned yet is Pd. Indeed, as evident from the Pd 3d region reported in Figure 32, almost no intensity is observed around 335 eV (Pd $3d_{5/2}$) in spite of its relatively high cross section under the present experimental conditions. This indicates that throughout the deposition and thermal evolution, Pd atoms are efficiently screened, i.e., that they migrate below the Ag surface. The implication of this is that the CyPd interaction causes the breaking of the molelule and the release of Pd atoms, which are then free to migrate into the crystal. This hypothesis will be further developed in light of STM data and DFT calculations.

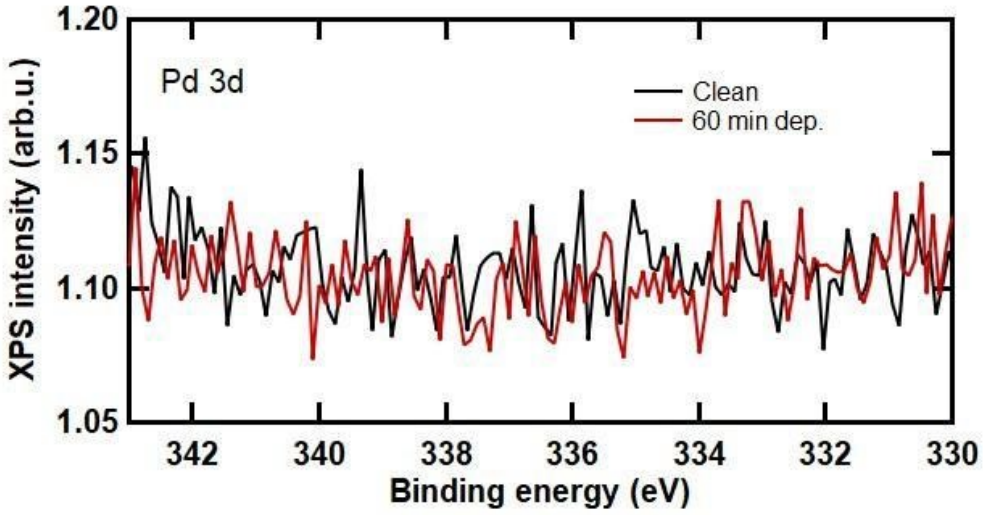

*Figure 32. XPS spectra of the Pd 3d region before and after **CyPd** deposition. No significant intensity is present at the binding energies expected for the Pd 3d lines (around 335 eV and 340 eV).*

For the moment I wish to mention that the possibility that the molecule dissociates in the crucible during sublimation is ruled out because: i) at RT, the C:Br, C:Cl and C:N ratios are close to the stoichiometric value of 11:1, though there is a slight deficiency in C [84], (see table XX; ii) as I will elaborate later, the molecular fragments organize on the surface in an ordered, reproducible, and periodic structure. If fragments were produced into the crucible because of thermal degradation catalyzed by the crucible material, the produced fragments would have different sublimation temperatures and therefore their relative abundance on the surface should be far from molecular stoichiometry. Iii) Thermogravimetric analysis of the molecules shows a clear drop off point at above 300°C, Figure 33, suggesting that thermal degradation occurs much higher than the established sublimation temperature. Iv) Finally, the ATR-FTIR and XPS analysis of the fresh **CyPd** powders and after several sublimation cycles in the crucible yielded perfectly compatible results, further indicating that no degradation of the molecule had occurred, Figure 34 and Figure 35, respectively.

acronimo non definito

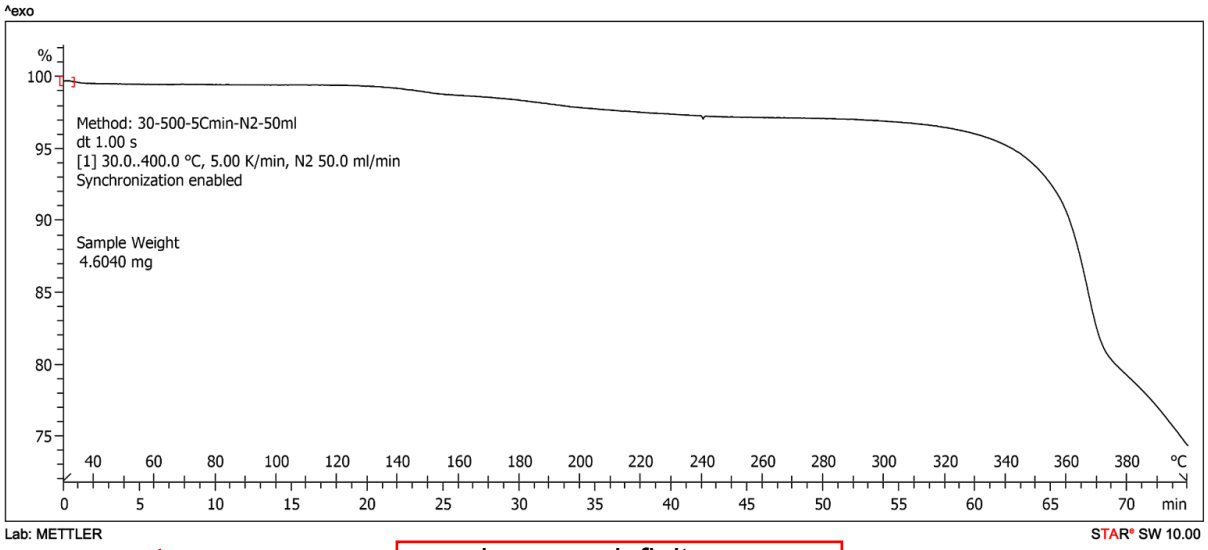

Figure 33. TGA analysis of CyPd.

acronimo non definito

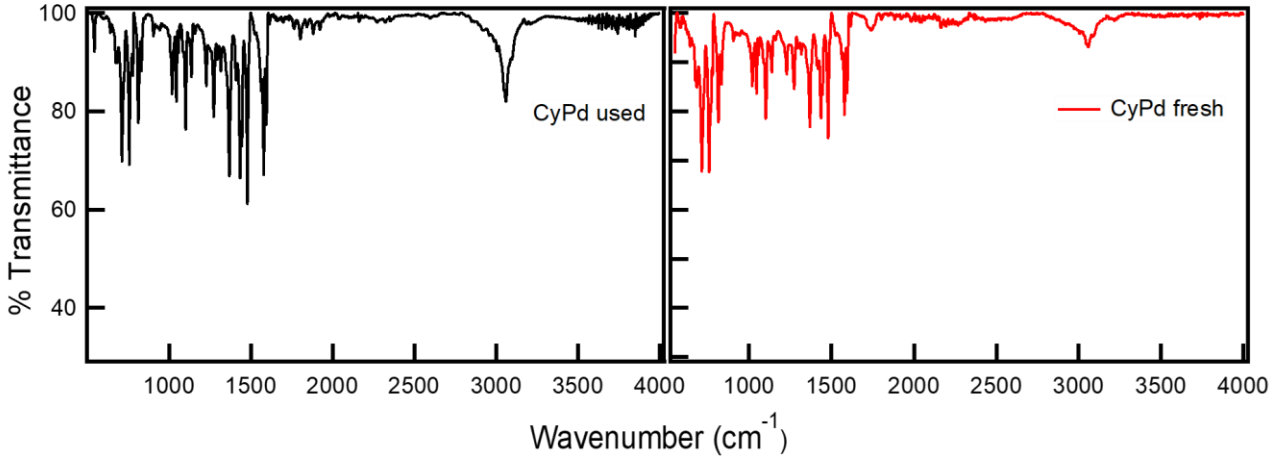

Figure 34. FTIR ATR spectra of CyPd molecules in the 1650-550 cm^{-1} region. The spectra compare the CyPd Powder as prepared, recorded with a Perkin Elmer Spectrum 100 FTIR spectrometer and after several sublimation cycles in the crucible, recorded with a Nicolet iS20 FTIR spectrometer.

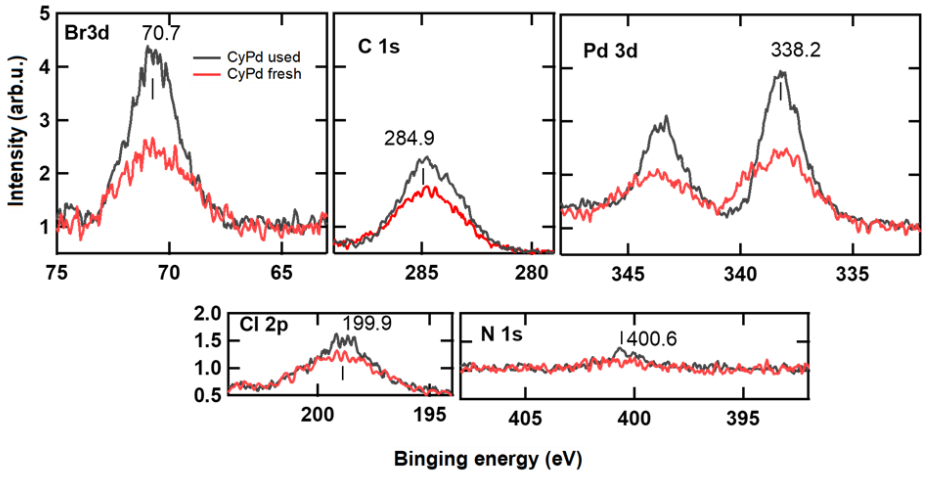

	C1s/N1s	*Cl2p/N1s*	*Br3d/N1s*	*Pd3d/N1s*	*Br/Cl*
Nominal value	*11*	*1*	*1*	*1*	*1*
Powders new	*14.5*	*1.64*	*1.26*	*1.24*	*0.77*
Powders used	*13.3*	*1.26*	*1.15*	*1.14*	*0.91*

Figure 35. XPS spectra of CyPd powders as prepared (red traces) and after several sublimation cycles (black traces). Br 3d, C 1s, Pd 3d, Cl 2p and N 1s regions are reported. The spectra are recorded with a XPS, hemispherical analyser model 10–360 and monochromatic X-ray source model 10–610 by Physical Electronics. The slightly larger shape of the fresh CyPd spectra is due to limited charging effects during the acquisition of the spectrum, which do not affect our analysis.

5.2 NEXAFS SPECTRA OF CYPD/AG(110)

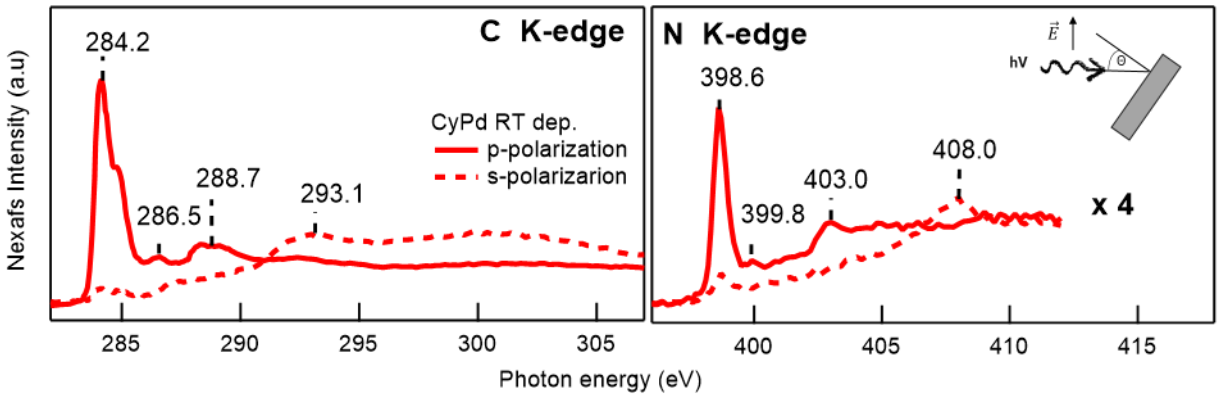

Figure 36. NEXAFS spectra of the C K-edge and N K-edge recorded with the linearly polarized photon beam impinging normal to the surface (corresponding to s-polarization) and at 85° incidence (corresponding to p-polarization).

During the beamtime at Aloisa, we collected also the NEXAFS spectra corresponding to the RT preparations of Figure 30 and Figure 31. The scope of this experiment was to gain possible information of the orientation of the molecule or molecular fragments when adsorbed at the surface.
The NEXAFS spectra of Figure 36 report the C and N K-edges recorded after deposition of a full monolayer of **CyPd** on Ag(110) at RT. Main resonances are present at 284.2 eV, with a shoulder at

284.8 eV and at 288.7 eV in the C K-edge spectrum recorded in p-polarization (continuous lines). Their intensity is reduced by a factor of ~10 in the s-polarization spectra (dashed lines), while broad structures centered around 293 eV and 300 eV appear. The energy region below 290 eV is dominated by π* resonances. I identify the peak at 284.2 eV and the smaller one at 288.7 eV with the $1s \rightarrow \pi_1^*$ and $1s \rightarrow \pi_2^*$ transitions from C 1s occupied core-levels to the lowest unoccupied molecular levels (LUMOs), in agreement with what reported in previous literature for the aromatic systems of phenyl rings [85]. The shoulder at 284.8 eV in the main π^* resonance is likely related to the non-equivalent C atoms bound to N atoms in the pyridine unit [86]. A contribution of C-Ag interaction to the NEXAFS features cannot be excluded. The energy region above 290 eV is characterized by σ* resonances.

The N K-edge spectra show peaks at 398.6 eV and 402.9 eV in p-polarization, while a large resonance around 408 eV is dominant in s-polarization. These features are assigned to the transition of N 1s electrons into the π_1^*, π_3^* and σ^* molecular states, respectively, in good agreement with what reported for gas-phase pyridine [86] and for pyridine compounds on Au [79,87].

The strong polarization dependence of NEXAFS spectra implies a preferential orientation of the molecules. However, the residual intensity of π* transitions in the s-polarization spectra indicates that the molecular plane is not flat with respect to the surface. An estimation of the molecular tilt angle can be given by evaluating the s-/p-polarization intensity ratio and following the approach indicated by Stohr for a two-fold symmetry domain [51]. Considering the error introduced by the spectra normalization procedure as well as the azimuthal misalignment of the beam electric field with respect to the <001> direction due to the sample mounting, it was estimated that the molecules are tilted by (20±10)° with respect to the surface plane.

5.3 STM RESULTS OF CYPD ON AG(110)

So far, I have detailed some interesting and unexpected chemistry on the CyPd/Ag(110) system based on the information obtained by XPS and NEXAFS.To complement this information, I studied the morphology of CyPd/Ag(110) by LT-STM under the same experimental conditions: the molecules were sublimated at T_{sub}=130°C on Ag(110) at RT and the same annealing steps were taken to observe the initial morphology of the layer and its thermal evolution. I mention too that these STM experiments are divided into two sections, the former corresponding to sub-ML coverage and the latter to a full ML at RT. Indeed, the experimental conditions (sample temperature, CyPd sublimation temperature and deposition time) were nominally the same in both experiments, but no full monolayer coverage could be reached in the first preparations. We deduce that the molecular flux on the surface was significantly lower and, indeed, XPS experiments indicate that this parameter generally increases after several sublimation cycles, i.e. when the molecules get better outgassed. Since the molecules self-assemble in different geometries in the two cases, I suggest that the kinetics of the self-assembly process plays a role in determining the final structure. If the flux is low, the molecules land on the surface and have time to dissociate, diffuse and interact with Ag atoms. Increasing the flux, the mobility of molecules/fragments is reduced and the probability of inter-molecular interactions during the formation of the self-assembly gets larger and may lead to completely different arrangement, as discussed in the following.

Unfortunately, it was not possible to measure the CyPd flux directly in the experimental apparatuses available.

5.3.1 Sub ML coverage of CyPd on Ag(110)

Upon deposition of **CyPd** on Ag(110) at RT I always observed the formation of extended self-assembled patterns. In the case that only sub-ML coverage is reached, the observed geometry is the one reported in the overview of Figure 37. It should be noted that no isolated molecules were observed on the surface, but that these compact islands coexist with bare Ag(110) patches. On the other hand, I could not find traces of multilayer in the present experimental conditions, which suggests that **CyPd** adsorption is a self-limiting process: an attractive interaction among molecules is present and, at RT, they are mobile enough to diffuse on the surface to serve as a nucleation site for a new island of molecules or to merge an already existing one.

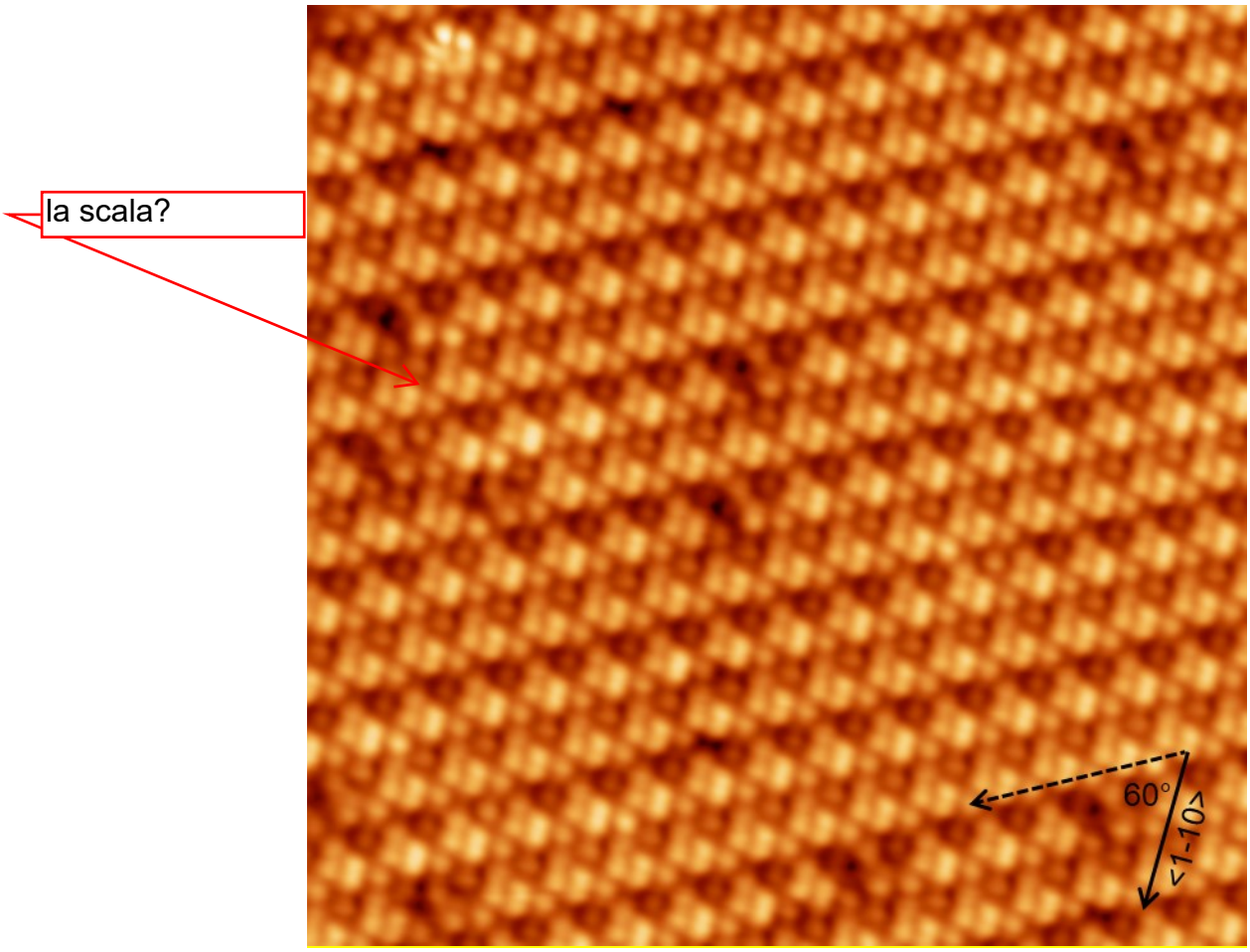

Figure 37. STM overview of the self-assembly of CyPd on Ag(110)

The 2D-network I observe for sub-ML coverage consists of lozenge-shaped features assembled in a double row-structure (Figure 37). The rows are oriented ±(60°±3°) off the <1-10> direction. Each feature consists of four lobes of slightly different brightness arranged in a rhomboidal shape and are surrounded by some interstitial dots. More details are shown in the enlarged image of Figure 38.

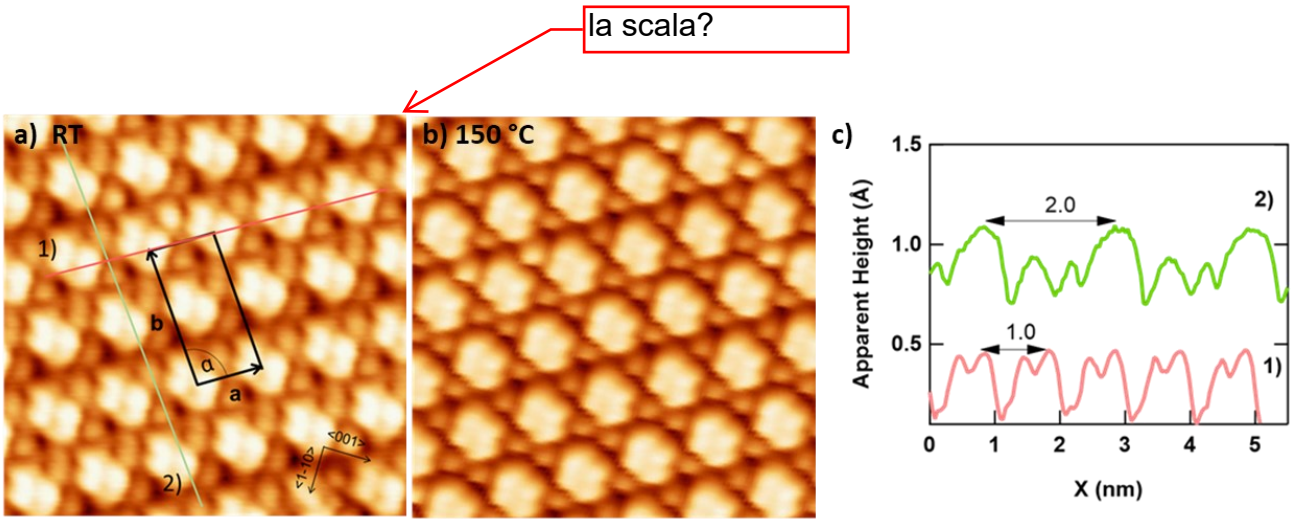

*Figure 38. **Details of the self-assembly.** a) High resolution STM image of the self-assembled layer. The unit cell is marked by the black rectangle. The high symmetry directions of Ag(110) are marked in the bottom-right corner. b) upon annealing to 150 °C for 5 minutes (Imaging at 80 K). In both cases, image size: 6 x 6 nm², V= -0.1V, I=0.1 nA. c) Height profiles cut along the red and green traces in panel B1), corresponding to the unit cell directions **a** and **b**, respectively.*

A comparison of the morphology of the **CyPd**/Ag(110) sample as grown at RT and after annealing to 150 °C is shown in Figure 38. No significant changes are observed in the layer upon annealing to T=100 °C (not shown) and to 150 °C. Statistical analysis of several equivalent images and of line scans as the ones reported in c) helped me to determine the typical periodicities of the self-assembled geometry and eventually to draw the unit cell marked in Figure 38a. At RT, it is nearly rectangular, with unit cell vectors **a**=(0.97 ± 0.04) nm and **b**=(2.01 ± 0.10) nm aligned along the rows and perpendicular to them, respectively. The unit cell parameters are compatible within the error for the sample as grown and after annealing (see Table 3), confirming the deduction that the observed self-assembled geometry is stable in the investigated temperature range. I remark that a smaller unit cell is not possible because the pairs of rows are slightly misaligned and the separation between one row and the next is not the same on either side.

	RT	100 °C	150 °C
UNIT CELL PARAMETERES	a=(0.97±0.04)nm b=(2.01±0.10)nm α=(86±3)°	a=(0.94±0.01)nm b=(2.13±0.01)nm α=(90±1)°	a=(0.94±0.03)nm b=(2.00±0.12)nm α=(89±1)°
ORIENTATION OFF <1-10>	±(60±3)°	±(60±3)°	±(60±3)°

Table 3. Unit cell parameters of the ordered structures from CyPd on Ag(110) at RT deposition, 100 and 150°C annealing.

Each unit cell consists of two lozenge-shaped features and four smaller and fainter dots. By comparing the experimentally determined values of the unit cell with the expected molecular dimensions of the isolated **CyPd** molecule (1.34 nm long and 1.05 nm wide), I estimated that there is one molecule per unit cell, with a corresponding local coverage of $(5.1\pm 0.1)\cdot 10^{13}$ molecules/cm^2. Looking at the structure inside the unit cell more closely, the two large features could correspond to the two halves of the molecule, while the dots around them are less straightforward to identify. Referring to previous literature on halogenated aromatic systems on the same surface [23,43] and considering the evidence of dehalogenation given by XPS, I can tentatively assign them to dissociated Br atoms and/or Ag adatoms taken from the substrate. However, this hypothesis needs to be verified due to the larger complexity of the **CyPd**/Ag(110) system with respect to the cited ones. Finally, I note that the structure of **CyPd** consists of two equivalent parts rotated by 180° with respect to each other, while careful

inspection of the high-resolution images of Figure 38a and b shows that all the lozenges have the same shape and orientation.

5.3.2 DFT calculations: sub ML CyPd on Ag(110)

The experimental information available for the CyPd/Ag(110) system was used as inputs by our partners at UNIMIB to model the system by DFT. I will present here the model of the structure observed at sub-ML coverage while in the section 5.3.4 the results relative to the full ML structures will be reported.

conformations

Based on the STM images and on the XPS information, we tried to figure out a reasonable model for the self-assembly of Figure 38. Calculations were long and accurate. Our partners started from the geometry optimization and simulation of the STM image of the undissociated CyPd molecule (which is contrary to experimental evidence but functional to the development of the calculations) and proceeded to test different conformation of the dissociated molecule. They always based the choice of the next step on a close comparison between the simulated and experimentally observed geometry. I summarize here the main information functional to the interpretation of the experimental data; more details on DFT calculations can be found in ref. [84] and in the associated supporting material.
The Ag(110) supercell model that was considered in the computational study (purple full cell in Figure 39a) is almost coincident with the experimentally determined repeating unit and it is characterized by a surface area sufficient to support one Pd dimer complex ($C_{22}H_{14}Br_2N_2Pd_2Cl_2$) (Figure 39a).

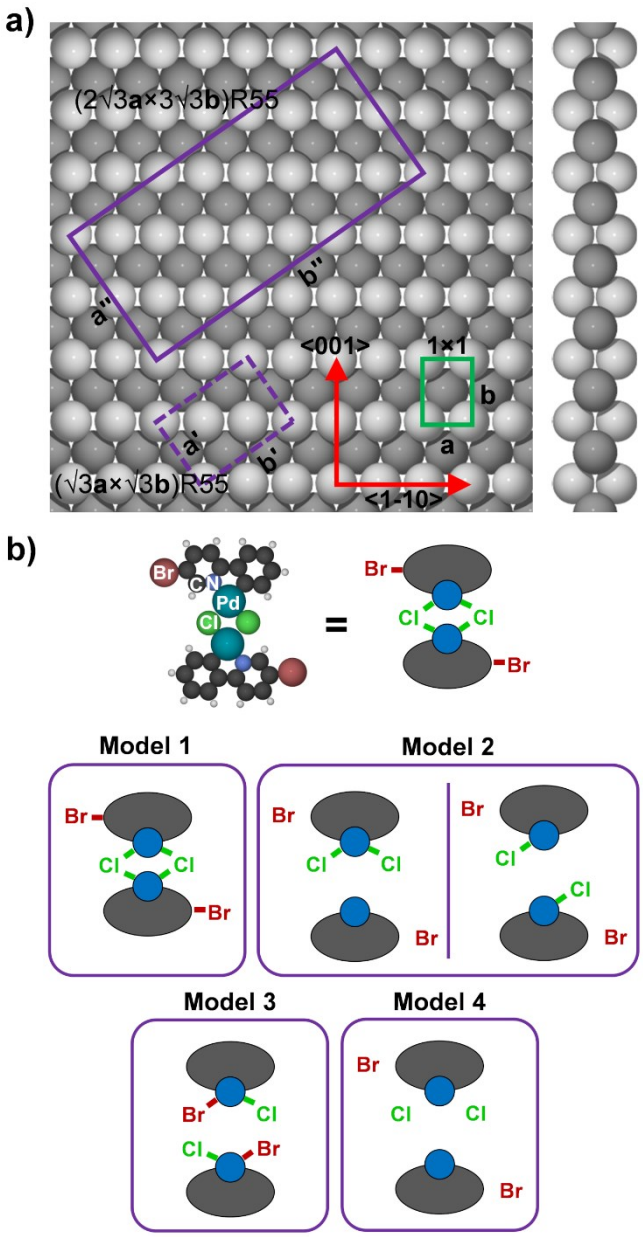

*Figure 39. a) Top and side view of Ag(110). The surface unit cell is shown in green, whereas the smallest unit cell with the same orientation as the experimental one (rotated by ≈60° with respect to the <1-10> direction) is marked in dashed purple. Given the size of **CyPd**, a (2 × 3) supercell was used (purple full cell). Ag atoms in the top and bottom layer are rendered in light grey; Ag atoms in the middle layer are rendered in dark grey. b) Scheme of possible adsorption/dissociation configurations of **CyPd** according to the different chemical connectivity.*

From here, the possible configurations of CyPd on the surface were considered and labelled as models 1-4 (Figure 39b). Model 1 is the undissociated CyPd complex while the following models correspond to the molecule dissociated in two Phe-Pyr-Pd fragments and with different distribution of the halogen atoms (bound to a fragment or to the Ag substrate). For the moment only the dissociation pattern is considered; in a next step also the fact that Pd can migrate into the bulk will be taken into account. In each model, the molecules/molecular fragments are deposited on the Ag supercell and the lowest energy configuration is calculated. Then the corresponding STM image is simulated and compared to the experimental one. Model 4, in which the halogen atoms are separated from the two Phe-Pyr-Pd fragments, best reproduces the experimental images of CyPd/Ag(110). However, since we know from

XPS that the Pd atoms do not stay at the surface, the new model 4-Ag was developed, in which a Pd-Ag exchange is performed (Figure 40). This system is only +50 meV less stable with respect to model 4. The atomic charge on the Ag atom attached to the phe-pyr fragment (+0.37 e^-) is about the same as the one calculated for the Pd atom (+0.39 e^-) in the previous model 4. Therefore, Model 4-Ag is the structure we propose as the one that best fits the experimental findings for sub ML CyPd (110).

lines or arrows?

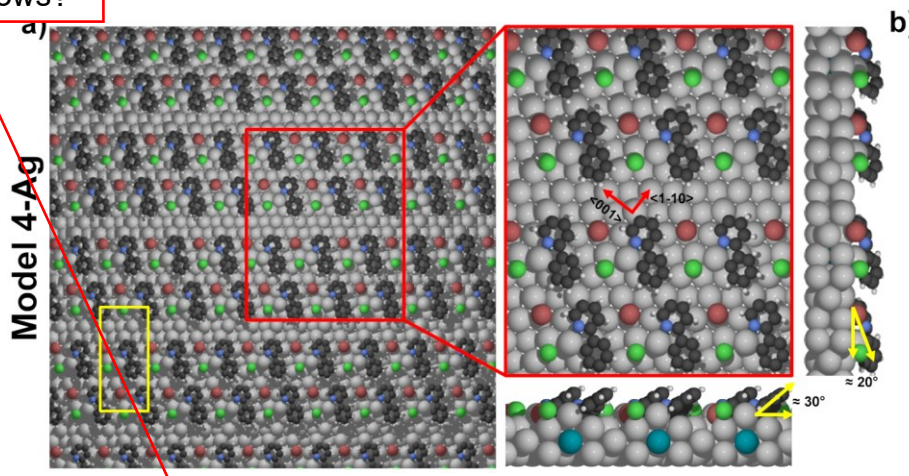

manca la scala

*Figure 40. a) Top and side view for Model 4-Ag of **CyPd**/Ag(110). Red lines indicate the two main crystallographic directions <001> and <1-10>. Yellow lines indicate the estimated tilting angle values for the molecular fragments with respect to the metal surface plane. The unit cell is indicated by a yellow box. Atoms color code is the same as reported in Figure 4b. **b)** Simulated STM image (V=-0.5 V) with the optimized DFT adsorption configuration overlayed (Model 4-Ag). The two lozenge shaped features correspond to the phenyl-pyridine unit bridged by Ag adatom (orange ball); the fainter surrounding dots are the dissociated Br (red ball) and Cl atoms (green ball). The pyridinic part of the ring has darker contrast with respect to the phenyl ring, appearing as a brighter protrusion in the STM image. Pd occupies the octahedral sites below the surface and hence it does not appear in the figure. The corresponding experimental STM image is reported in the bottom-left corner to underline the good matching.*

I mention that metal ion exchange between organometallic compounds and the metallic substrate has already been reported for several systems, as Ni porphyrins [88] and Co phthalocyanines [89] on Cu(111). The exchange is favored by annealing of the adsorbed layer but, when the molecules are sublimed at 700 K, their high thermal energy ignites the process already at RT. I do not believe this holds in the present case, in which the molecules were sublimed at 130 °C (403 K), while the exchange is likely to be favored by the dissociation of the CyPd complex upon interaction with the Ag surface. Diffusion of the Pd atom below the surface is not surprising, since the surface energy of Pd is significantly higher than that of Ag [90] (2.05 J/m^2 for Pd and 1.25 J/$m/^2$ for Ag), so that Pd atoms tend to migrate into the bulk of the Ag crystal. This is confirmed by state-of-the-art calculations on the growth of bimetallic AgPd clusters, showing the formation of a core-shell structure with Pd atoms preferentially in subsurface sites [91].

To verify this trend, and since our XPS data suggest that Pd atoms may go deeper into the crystal, the geometry optimization of Model 4-Ag of **CyPd**/Ag(110) was repeated increasing the slab thickness from 3 Ag layers up to 5 and 7 Ag layers. The outcome indicates that in the most stable configuration the Pd atoms are always in the middle of the slab (i.e., in the central Ag layer), with a gain in energy of -0.06 and -0.08 eV/Pd for the 5-layer and 7-layer slabs, respectively. The segregation effect of Pd in the subsurface metal layers can be even further facilitated by the high mobility of Ag atoms at the surface, which was not taken into account in the simulations and would support the experimental information.

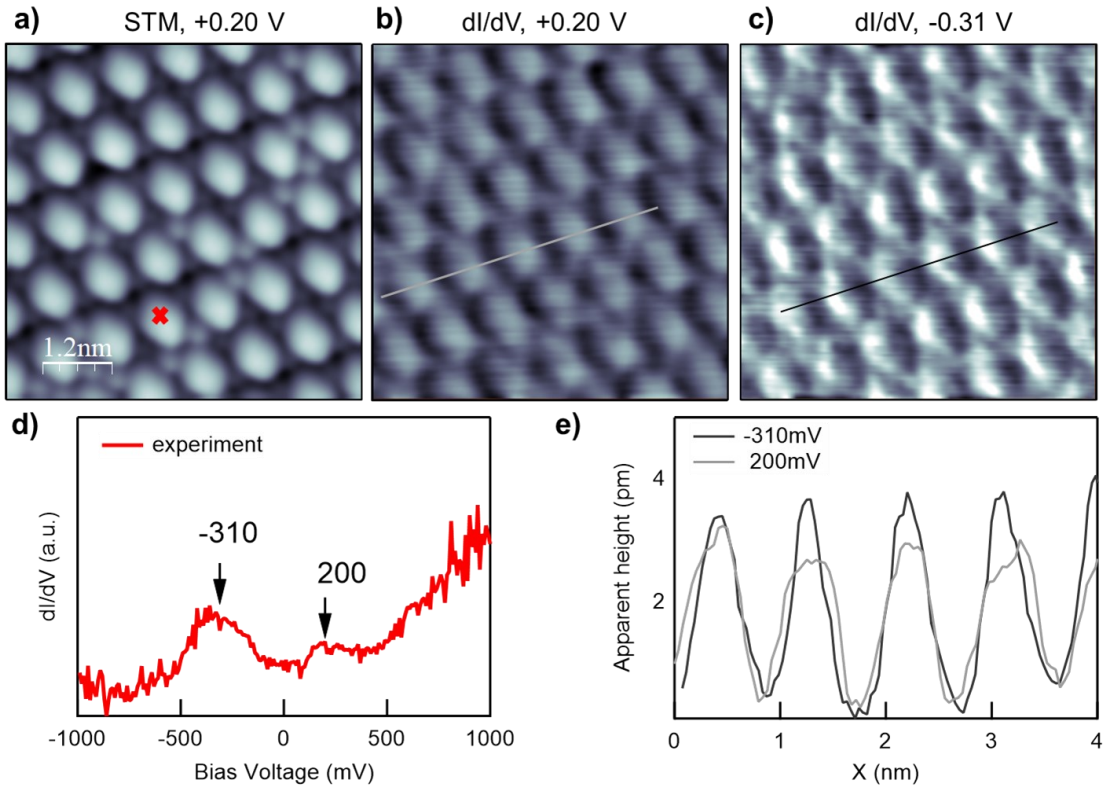

Figure 41. ***a)*** *STM image of* ***CyPd*** *upon RT deposition. The red cross marks the point where the STS spectrum of panel* ***d)*** *was recorded. Image size: 6.0 x 6.0 nm², V =+0.2 V, I= 0.42 nA.* ***b) and c)*** *dI/dV maps taken at the bias voltages corresponding to local maxima in the STS spectrum of panel* ***d). e)*** *Line scans cut along the grey and black traces marked in the* ***b)*** *and* ***c)****.*

complementary

After investigating the morphology of CyPd on Ag(110), I also collected complimentary information on the electronic structure by recording STS spectra and dI/dV maps. The outcome is reported in Figure 41. The STM image of panel a) matches the double row structure described in Figure 38, though the internal structure of the lozenges is not evident due to the lower resolution. The STS spectrum of panel d) is measured at the center of a lozenge (cross in a) and is representative of the local density of states of CyPd around the Fermi Edge. In fact, several STS measurements performed at different points of the unit cell gave spectra equivalent to the one of panel d), which is characterized by a weak state at V~+0.20 V and by a broad and more intense one at V~−0.31 V. The rising tail above +0.5 V is coherent with that observed for other aromatic compounds as benzene [92]. The dI/dV maps recorded in correspondence of the observed states (panels b and c) show that the lozenges supposedly corresponding to the CyPd molecule have a different contrast at the two bias voltages. These differences are reflected in the line scans of panel e), cut along the lines marked on the dI/dV maps. While a lower and broader corrugation is found for V=+0.20 V, the profile measured at V=-0.31 V is sharper and with slightly asymmetric shape induced by the presence of a bright spot in each lozenge. STS and dI/dV maps suggest, therefore, the presence of a localized state around V=-0.31 V, in a position corresponding to the N atom in the pyridinic ring. This assignment agrees with the STS spectra of N-doped graphene with N atoms in pyridinic configuration [93], while the benzene ring is expected to have an empty state at higher energy (approximately 2.0 V) [92].

5.3.3 Full ML coverage of CyPd on Ag(110)

When repeating the CyPd deposition on Ag(110) at RT with a higher flux, I saw distinct structures compared to the sub-ML coverage. The polymorphic behaviour I report here shed light into the complexity of this system.

The STM image in Figure 42 shows an overview of the Ag(110) surface after deposition of CyPd at RT for 30 minutes. The surface is covered by a compact overlayer of adsorbates. No clean areas of the Ag substrate nor evidence of double or multilayer formation is observed inspecting multiple areas of the sample. Given this, I could safely conclude that full monolayer coverage has been reached for this preparation and that the process is self-limiting.

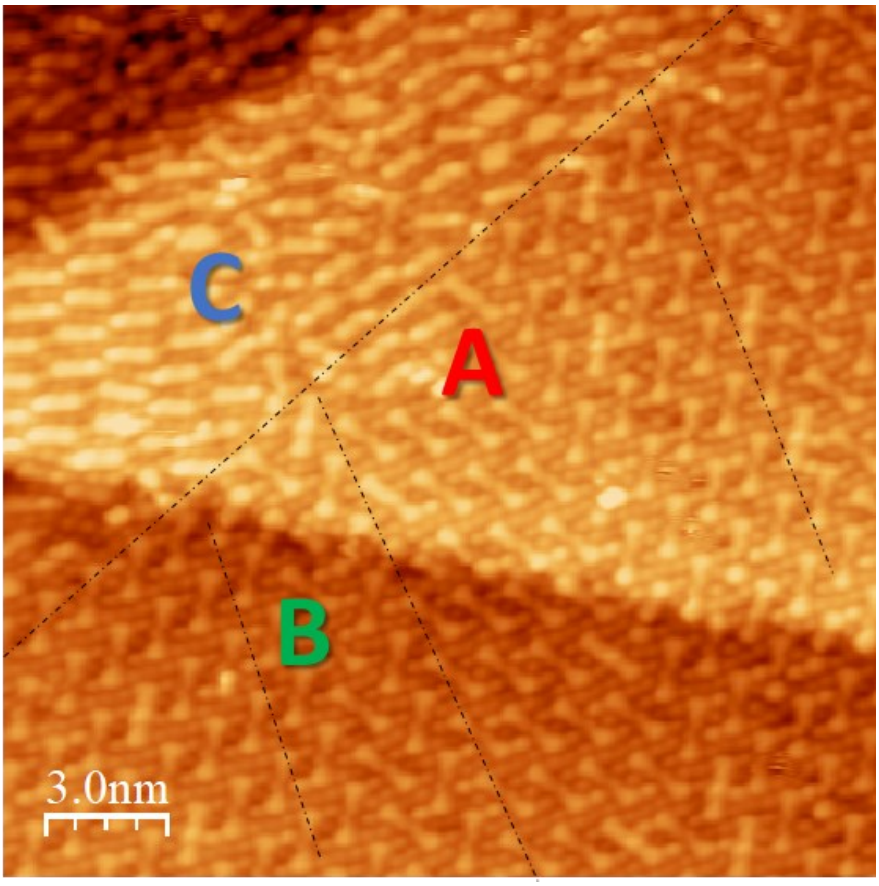

Figure 42. STM image of the Ag(110) surface after 30 min deposition of CyPd at RT. Image size: 21x21 nm², V =0.36 V, I= 0.64 nA. A,B and C domains are separated by dashed lines.

Three different self-assembled geometries (labelled A, B and C in the following) coexist in Figure 42. Figure 42 shows separate surface areas covered by extended domains of each of these structures. The common feature among them is the presence of stick-shaped units separated by dots and oriented ±30° off the <1-10> direction, which acts as a mirror axis. In domain A, all the sticks have the same orientation, while in domain B adjacent sticks have opposite orientation and form a sort of zig-zag pattern (see also enlarged images in Figure 43). Since it is difficult to distinguish A and B domains of the smallest size, for simplicity and to be able to define a unit cell we identify a domain as of A or B type if it contained a minimum of four sticks with the same or with alternating orientation, respectively. In structure C, the same sticks observed in structures A and B appear as minority structures, being surrounded by shorter features with a brighter end (Figure 43c). A few diamond-shaped features are also randomly present (see top-right corner of domain C in Figure 42). Arrangement C has a short-

range and much lower degree of order and it disappears above RT; therefore, it will not be discussed in further details.

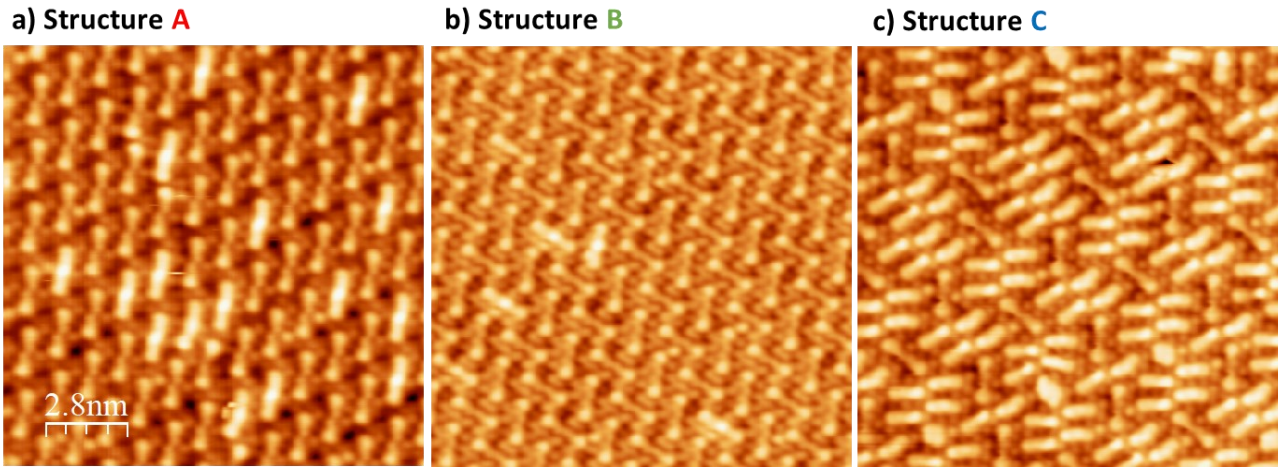

Figure 43. STM images showing long-range order self-assemblies of type A, B and C. Images are recorded for the same sample of Figure 1c of the main text, i.e. upon 30 min deposition of CyPd at RT. Image size 14x14nm², V=0.5V, i=0.2 nA.

Temperature

After deposition at RT, the sample was step annealed up to a maximum temperature T=450 °C to investigate the thermal evolution of the self-assembled layers. Annealing to 100°C resulted in the disappearance of structure C, a reduction in the extension of B and an increase of the area covered by structure A. Such behavior suggests that the most ordered geometry is also the most stable one. I also discovered that, at this T, two new structures appear (Figure 46): the former (labelled I) consists of isolated sticks lying on a c(2x2) reconstructed surface; it becomes dominant at 200 °C and is almost completely removed at 250 °C. The latter (R) consists of bare Ag(110) areas with a (2x1) reconstruction. The area covered by structure R increases from 100 °C to 350 °C, at which T it extends almost over the whole surface. Above 450°C, the reconstruction has been lifted and clean, unreconstructed Ag(110) terraces appear in STM images.

5.3.3.1 Extended assemblies of type A and B

I decided to look more closely at the ordered arrangements. Figure 44 shows an enlargement of self-assemblies A and B, in which their geometry appears in better detail. The unit cell of structure A is defined by a black rhomboid with sides a=(1.26±0.01) nm and b=(2.24±0.04) nm. These vectors are oriented -12° and -58° off the <001> direction, respectively, and form an angle α=(46±3)° with each other. The unit cell contains one stick oriented nearly parallel to the **b** vector, and 6 dots of different brightness. Comparing the experimentally determined periodicities with the size of a CyPd molecule (1.34 nm long and 1.05 nm wide), I estimated a population of one molecule per unit cell, corresponding to a local coverage of $(4.9\pm0.1)\cdot10^{13}$ molecules/cm^2. For structure B, the unit cell is nearly rectangular, with a=(1.56±0.02) nm, b=(2.39±0.06) nm and α=(89±3)°, and with vector **b** parallel to the <001> direction. The unit cell contains 2 sticks, oriented at +30° and -30° off <1-10>, respectively, and 8 interstitial dots. Therefore, in this case the assembly is slightly more compact, accommodating $(5.3\pm0.1)\cdot10^{13}$ molecules/cm^2. For both structures A and B, the unit cell parameters measured at RT and after annealing are compatible within the error.

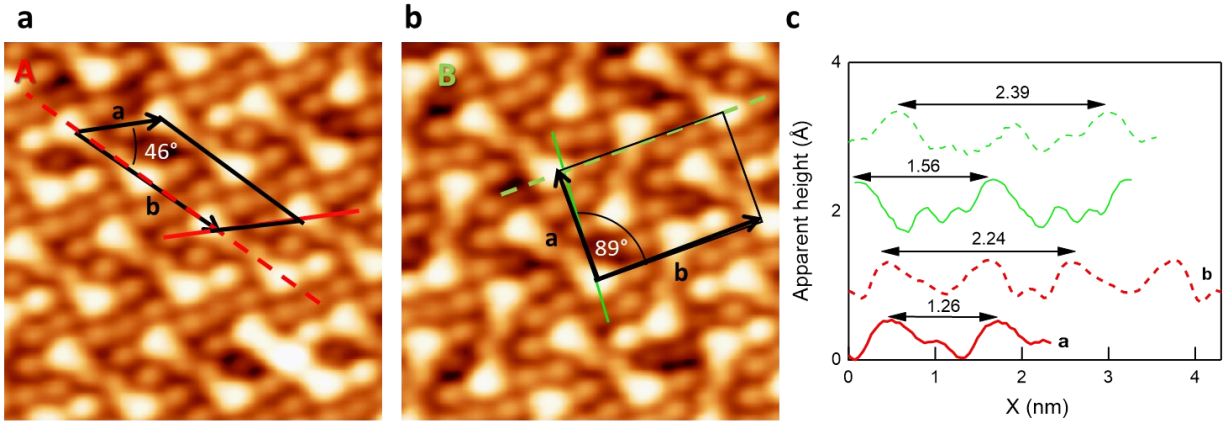

Figure 44. a) and b): Close-up STM images (5 x 5 nm^2) of the overview in Figure 1, showing the details of structures A and B, respectively. The unit cells are marked in black. $\vec{a} = 3.0\hat{\imath} - \hat{\jmath}$, $\vec{b} = 3.0\hat{\imath} - 6.5\,\hat{\jmath}$ *for structure A and* $\vec{a} = 4.5\hat{\jmath}$, $\vec{b} = 5{,}5\hat{\imath}$ *for structure B, being* $\hat{\imath}, \hat{\jmath}$ *the primitive unit vectors of Ag(110) in the <001> and <1-10> directions, respectively. c) Height profiles cut along the paths marked in panels a) and b) and corresponding to the unit cell sides.*

The sticks are basic constituents of the assemblies, and they are present in two different shapes. In most cases, they have a minimum at the center, but a few sticks with a central maximum appear in each overview. The high resolution STM image of Figure 45a and the corresponding line scans of Figure 45c emphasize this difference (the heat map in Figure 45b also highlights the two different sticks in even better detail). Sticks showing a minimum at their center (green continuous trace in panel c) are formed by two "comma-like" features facing each other. Each of them consists of a bright lobe (L) at the end of the stick and of a smaller and fainter lobe (F) pointing towards its center but misaligned with respect to the stick axis. Sticks with a maximum at their center present, on the contrary, a central lobe (L_c) slightly more protruding than the lateral ones (green dashed trace in panel c). The overall length is ~1.7 nm for both structures. The relative population of bright sticks in the compact assemblies of type A and B varies from 10% to 20% depending on T, as indicated in the histogram in panel d. Sticks are surrounded by several dots of alternating brightness. Since their density exceeds the number of halogen atoms expected for each molecule, I think that they correspond both to halogen and Ag atoms and indicate that a significant reorganization of surface atoms occurs upon CyPd adsorption and dissociation.

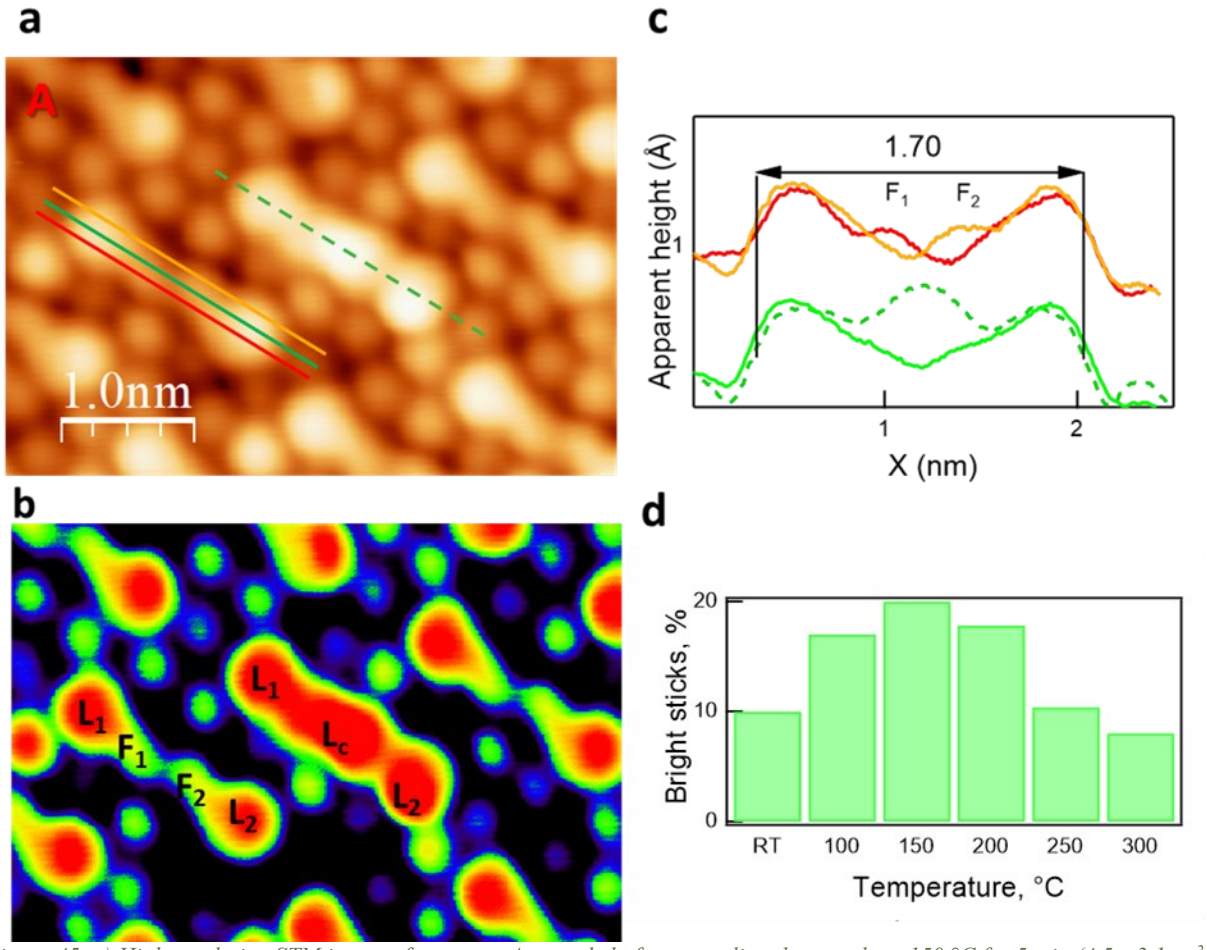

Figure 45. a) High resolution STM image of structure A recorded after annealing the sample to 150 °C for 5 min (4.5 x 3.1nm², V=-0.1 V, i=0.2nA). b) Same image of panel a) plotted with a different color palette to better highlight details. c) Height profiles cut along the traces marked in panel a. d) Histogram showing the distribution of bright sticks in domains A and B.

5.3.3.2 Isolated structure and surface reconstruction

After annealing the sample to 100 °C, desorption of the Phe-Pyr units occurs. This is consistent with the XPS information that the organic component strongly reduces when increasing the temperature. Sample areas with little or no molecule-related features start to appear in STM images. Figure 46a shows a STM overview of the Ag(110) surface after annealing to 200 °C. Most of the surface is covered with structure I, which consists of isolated sticks oriented ± 60° off the <1-10> direction. All the sticks have a central bright lobe and are ~1.7 nm long, thus, they highly resemble those already discussed for assemblies A and B. They sit on top of Ag terraces presenting a slightly compressed hexagonal pattern (see panel b) which, for fcc crystals, corresponds to a c(2x2) reconstruction of the (110) face. Therefore, the different orientation of the sticks (±60° off <1-10> instead of ±30° for the compact structures) could be related to the low density and/or to the symmetry of the reconstructed Ag terrace. In addition, a few areas with a rectangular pattern typical of a p(2x1) reconstruction of the substrate (indicated by R – see unit cell dimensions and orientation marked in panel c) are visible in the overview. Such patches grow with T and cover most of the surface at 350 °C. I remark that no molecular features are found on the R structure. This observation indicates that R becomes energetically favored only after complete local desorption of the organic fragments.

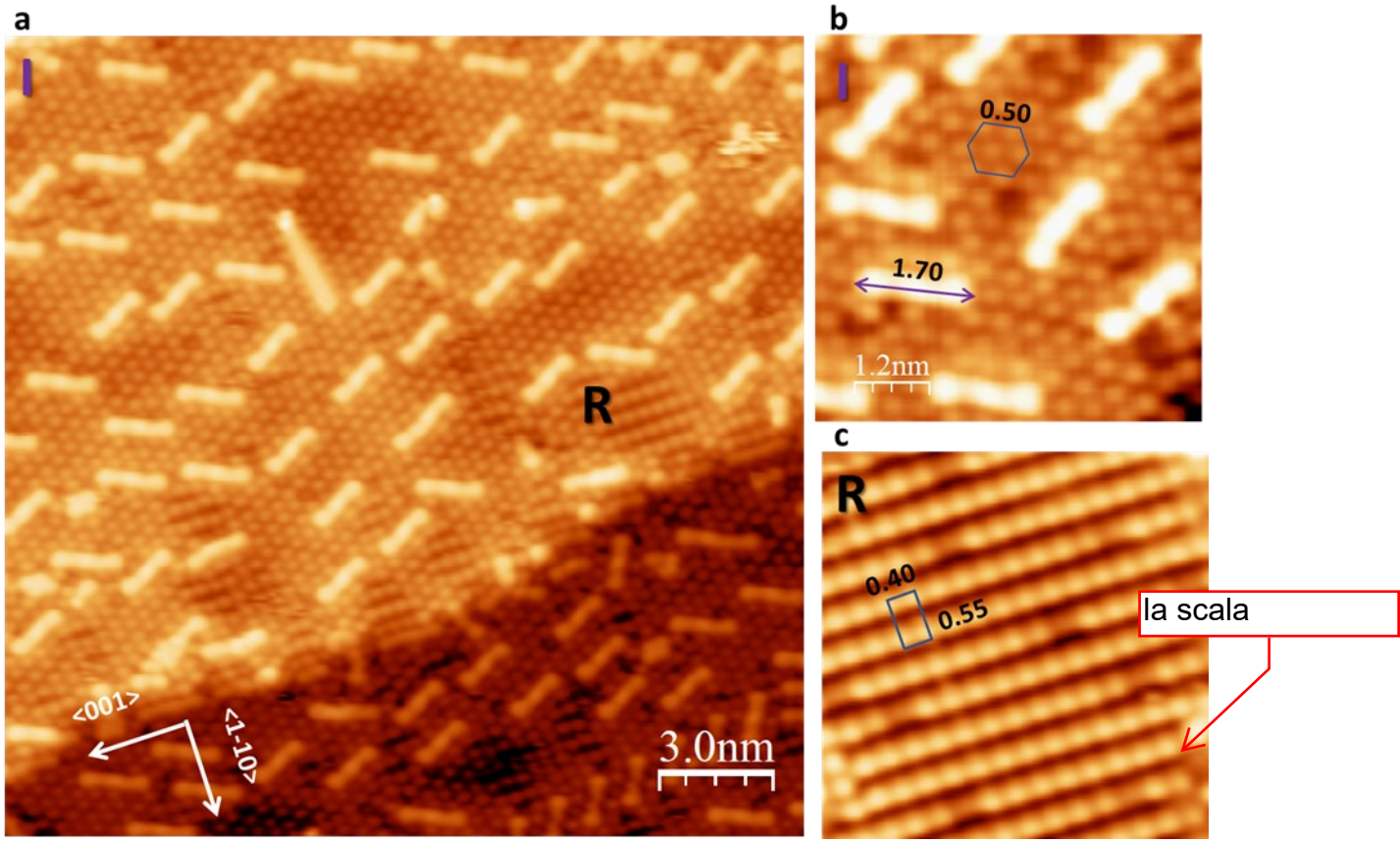

Figure 46. a): Overview STM image of the Ag(110) surface covered with structure I. Domains with reconstructed p(2x1) surface are also present and labelled as R. The image was recorded after step-annealing the sample to 200 °C for 5 minutes (20x20 nm^2, V= 0.5 V, i=0.2 nA). b) and c): Close-ups of I and R structures (6 x 6nm^2, V=-0.5 V). The unit cell of the reconstructed surface is reported on both panels; dimensions are expressed in nm.

5.3.4 DFT calculations: full ML CyPd on Ag(110)

To determine the atomic structure and conformation of the bright sticks, a second DFT study was performed starting from a model consistent with the experimental evidence. We recall that XPS data suggests dissociative adsorption of CyPd on the Ag surface followed by Pd atoms diffusion into the surface. Cl and Br atoms disappear only for T > 300 °C and T> 450 °C, respectively, i.e., at a much higher temperature than the organic fragments, suggesting that also for the full ML structures the halogen atoms are detached from the molecule and adsorbed to the surface. Furthermore, the presence of a c(2x2) reconstruction must be considered. Based on this information, we assume that each stick is formed by two Phe-Pyr units (molecular structure of CyPd in Figure 21) anchored to the Ag surface. Halogen atoms are not explicitly present in the model, because we consider that they bind to a surface Ag atom immediately after dissociation from the organic fragments, and act then as spectators. Similarly, Pd atoms are not explicitly considered in the proposed model since, based on our previous calculations [84], they are expected to become buried beneath the Ag surface.

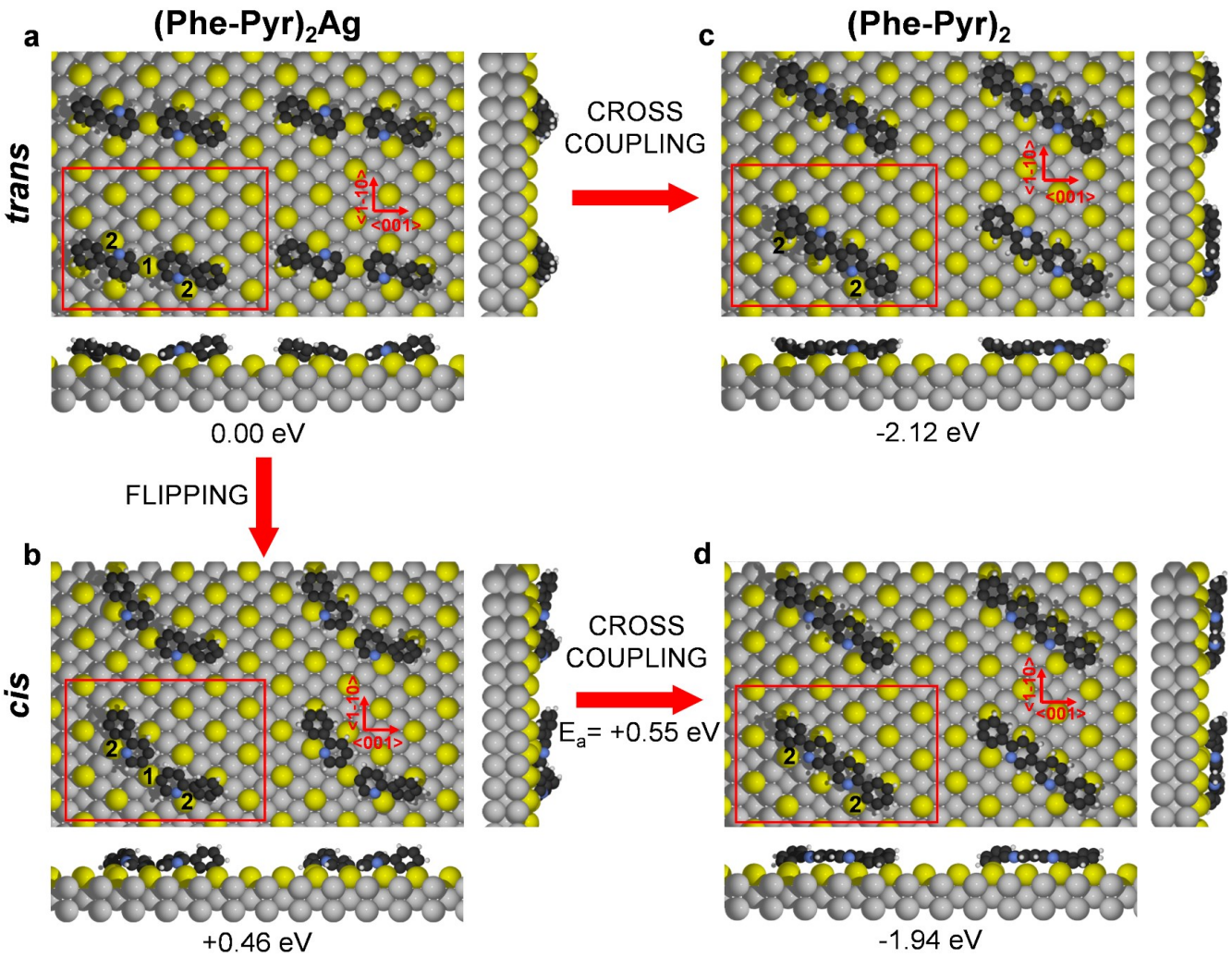

*Figure 47. Top and side views for adsorption models of CyPd on Ag(110)-c(2×2). The two main crystallographic directions (<001> and <1-10>) are indicated by the red arrows. The (6 × 3√2) supercell is shown in red. Relative energies (with respect to configuration **a**) are reported below each panel (in eV). Color coding: Ag atoms belonging to Ag(110) surface are in gray, Ag adatoms due to the c(2×2) reconstruction are in yellow, C atoms are in black, N atoms are in blue, and H atoms are in white. Ag adatoms involved in interaction with the molecular fragments are labeled as (1) and (2), as described in the text.*

The proposed adsorption models for dissociated CyPd on the Ag(110)-c(2x2) surface are reported in Figure 47, starting from two Phe-Pyr units in a *trans* configuration (see Figure 47a). The *trans* configuration, in which N atoms of the Pyr rings are on opposite sides of the two units (see blue atoms in the red box of Figure 47a), is expected to form after dissociation of a CyPd molecule and diffusion of the fragments on the surface. The optimized dimeric organometallic structure, named *trans* (Phe-Pyr)$_2$Ag, presents the two Phe-Pyr units almost aligned to each other and linked together through one Ag adatom (1), thus forming two bridging organometallic C-Ag-C bonds. Each Phe-Pyr unit is also anchored to another Ag adatom (2) by C-Ag and N-Ag bonds. It is worth noting that this configuration is stabilized through the passivation of all dangling bonds (produced by dissociation of the Pd and halogen atoms from the original molecule) by the Ag substrate, and that the new C-Ag and N-Ag bonds are responsible for the molecule orientation. The optimized model does not display any geometrical atomic protrusion at the expected location for the Ag adatom (as shown from the side view in Figure 6a), and it is thus consistent with the experimentally observed sticks with central minimum (Figure 45a and b) present in structures A and B. Indeed, the corresponding simulated STM image (see Figure 48) well reproduces the experimental image of the repeating unit of arrangements A and B (Figure 44), showing two features with brighter lobes towards the outside and fainter lobes facing each other.

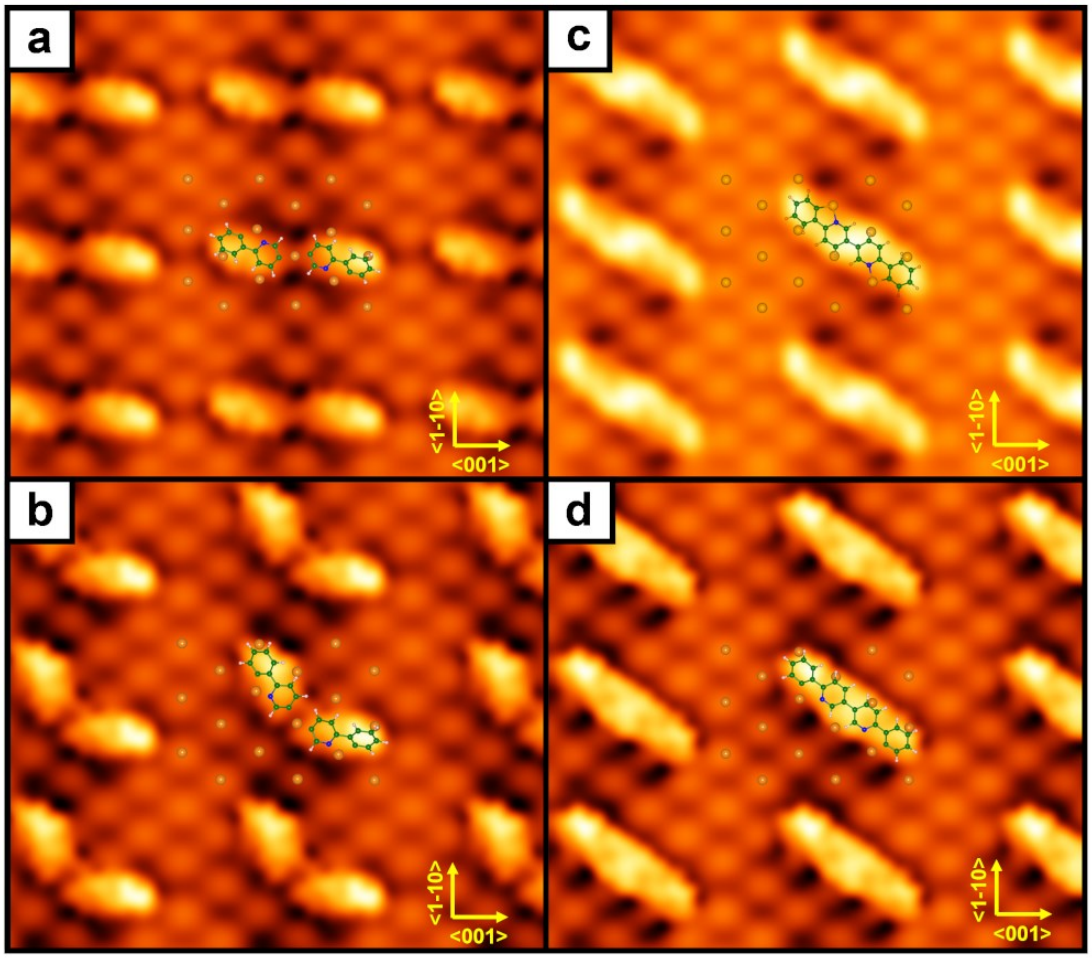

Figure 48. Simulated STM images of the models reported in Figure 7. Panels a, b, c, and d correspond to geometries a, b, c, and d of Figure 7, respectively. Yellow lines indicate the two main crystallographic directions: <001>, and <1-10>. Atoms of the CyPd molecule (C in green, N in blue, and H in white) and the Ag adatoms (in orange) contained in the (6 × 3√2) supercell are superimposed on the image to facilitate its understanding. V = −0.1 V, ILDOS iso-surface value of 5 × 10^{-5} $|e|/a_0^3$.

To explain why sticks in structure I (and in smaller numbers also in structures A and B) present a bright central lobe, we considered the possibility that a C-C coupling reaction occurs, which converts (Phe-Pyr)$_2$Ag into the organic dimer 6,6′ -diphenyl-3,3′ -bipyridine (Phe-Pyr)$_2$. Direct conversion from *trans* (Phe-Pyr)$_2$Ag (in Figure 47a) to *trans* (Phe-Pyr)$_2$ (Figure 47c), although largely exothermic (-2.12 eV), is likely to be kinetically hindered. In fact, the formation of the new C-C bond requires the two Phe-Pyr fragments to move over the surface and around the Ag adatom (1) till they get close enough for the C-C coupling. These adjustments could be energetically demanding since one organic fragment (e.g. the one on the left) must break a strong interaction with the Ag adatom (2) on the same row of Ag adatom (1) and establish a new bond with a Ag adatom in another row (compare Figure 6a and 6c). Therefore, we propose the alternative easier path shown in Figure 7bd: one Phe-Pyr unit of *trans* (Phe-Pyr)$_2$Ag flips on the surface around the Ag adatom (2), without need to detach from both Ag adatom (1) and (2), and converts into the *cis* (Phe-Pyrs)$_2$Ag conformer (Figure 6b). Starting from this new conformer, the C-C coupling can more easily take place and lead directly to the final *cis* (Phe-Pyr)$_2$ product (in Figure 6d). In this case, no detachment of the Phe-Pyr uint from the surface is needed because the two C atoms are now on the same side of the Ag(2)-Ag(1)-Ag(2) row. The activation barrier for this last step is computed to be 0.55 eV. Note that the simulated STM image of *cis* (Phe-Pyr)$_2$ (in Figure 7d) is in better agreement with the experimental images of sticks with a central maximum (in Figure 5b) than the corresponding simulated STM image of *trans* (Phe-Pyr)$_2$ (in Figure

manca il .

48c). Simulated STM images were performed for all the models and they are in agreement with the experiment. Experimentally, we observe that the density of bright sticks increases after the first annealing steps (see figure 41, above in the text), though the overall molecular coverage at the surface decreases significantly. This evidence is coherent with the small activation barrier found by DFT calculations in the conversion from configuration a) to d) (Figure 47) and confirms that this mechanism competes with desorption.

Finally, we should address the role of halogens and the presence of a surface reconstruction. We recall that Cl and Br remain stable at the surface up to temperatures much higher than the Phe-Pyr units. In particular, Br is stable well above the values measured in similar experiments leading to surface assisted synthesis of C-based networks [23,36,94]. An efficient desorption mechanism for halogen atoms chemisorbed on metals is to react with H and leave the surface in the form of hydrogen halide. This was the case, e.g. for di-bromo-pyrene, di-bromo-benzene and di-bromo-tetracene [23,94,95] on Ag or Cu surfaces. In those works, H is provided by further thermal induced dehydrogenation of the precursor molecule, or even by controlled exposure of the sample to a flux of atomic H [94]. The situation is different in the present case, since no additional C-H bonds are broken upon annealing; instead, Phe-Pyr units are likely to desorb intact or to cross-couple to form $(Phe\text{-}Pyr)_2$. We believe that the unavailability of H is the reason for the higher thermal stability of halogens with respect to other literature data, since they will desorb as diatomic molecules or metal halides [83,96,97] or, in case of the small Cl atom, may diffuse into the substrate [83].

Isolated sticks sit on a c(2x2) reconstructed surface, while a p(2x1) pattern appears in areas where all the $(Phe\text{-}Pyr)_2$ units have desorbed. Coherently, the latter domains get more and more extended with increasing T, i.e., when the coverage of organic fragments reduces. This is indicative of a strong surface rearrangement upon interaction with CyPd. We mention that, due to their open structure, (110) faces of fcc crystals are prone to surface reconstruction and roughening [98]. Such reorganization is certainly favored by the strong mobility of Ag adatoms, provided by step edges [99], and by the presence of halogen atoms, which are known to form superstructures on several metal surfaces [96,97]. However, we believe the present situation to be more complex. On the one hand, some atom reorganization is evident already at RT but, due to the dense packing of organic structures, it is not possible to understand if the surface underneath the adsorbates is reconstructed or if the additional atoms simply surround the sticks. Indeed, each Phe-Pyr fragment anchors to two Ag adatoms according to our model and it is reasonable that this is a driving mechanism for the displacement of Ag adatoms. On the other hand, we believe that halogens have a role in the reconstructed phases observed above RT, but that the observed superstructure is due to Ag adatoms. We base our statement on the following observation: i) the halogen coverage (nearly 1/4 of ML at RT) is not sufficient to justify the extended reconstruction observed as due to Cl and/or Br atoms; the c(2x2) reconstruction coexists with the isolated sticks and is observed in a T range in which both Cl and Br are stable on the surface. When the Cl signal decreases significantly ($T \geqslant 300$ °C), only clean, p(2x1)-reconstructed terraces are observed by STM. Therefore, we suggest that halogen atoms promote surface reconstruction, as previously reported for other elements on Ag(110) [100,101].

To summarize, from the DFT investigation above, the following picture emerges: the CyPd molecules land on the surface and dissociate; the two newly formed Phe-Pyr fragments align along a Ag(2)-Ag(1)-Ag(2) row, the dangling N and C bonds saturate towards the same Ag adatom (2), while the dangling C bond resulting from debromination saturates towards another Ag adatom (1) of the same row, forming a *trans* $(Phe\text{-}Pyr)_2Ag$ species (Figure 47a). The overall appearance in STM images is a stick-shaped structure with a minimum at the center (in line with Figure 44a and b). When enough energy is provided, through thermal annealing up to at least 100 °C, a fast *trans-cis* interconversion occurs (Figure 47b), followed by C-C coupling and formation of a *cis* $(Phe\text{-}Pyr)_2$ compound (Figure

47d). Since the latter lies flat on the surface, it appears as a stick with a central maximum (in line with structure I in Figure 46).

Therefore, our combined experimental and theoretical analysis suggests that surface assisted synthesis of the $(Phe\text{-}Pyr)_2$ compound occurs on Ag(110) by cross-coupling reaction of the two identical organic fragments generated by dissociation of a single organometallic CyPd unit. This is at variance with the majority of cross coupling reactions, which most often are used to build larger compounds or complex molecular architectures starting from the co-adsorption of different molecular species or from different molecules of the same precursor.

6 LOW TEMPERATURE (LT) DEPOSITION OF CYPD ON AG(110) - STM

6.1 STM RESULTS

As my first experiment, I deposited CyPd with T_{sub}=110 °C on Ag(110) at -100 °C and I monitored the surface by LT-STM. Figure 49 shows STM images after 15 min and 1 min CyPd deposition at LT. Panel a) denotes that the structures are arranged in quasi hexagonal symmetry and with a periodicity 0.4nm. While imaging this preparation, I notice that the sample is strongly interacting with the tip and when I could resolve an image, it was not flat. Hence, I assume I have produced multilayer of loosely bound CyPd molecules which are strongly interacting with the tip. Since 15 minutes of deposition time produced a multilayer, I diminished the deposition time to 1 minute, while keeping the substrate and evaporation temperature unchanged. The resulting surface panel b consists of patches of clean Ag and what seems to be amorphous clusters/multilayer of CyPd molecules. The next step was to anneal the layer, which I am going to discuss in the next section.

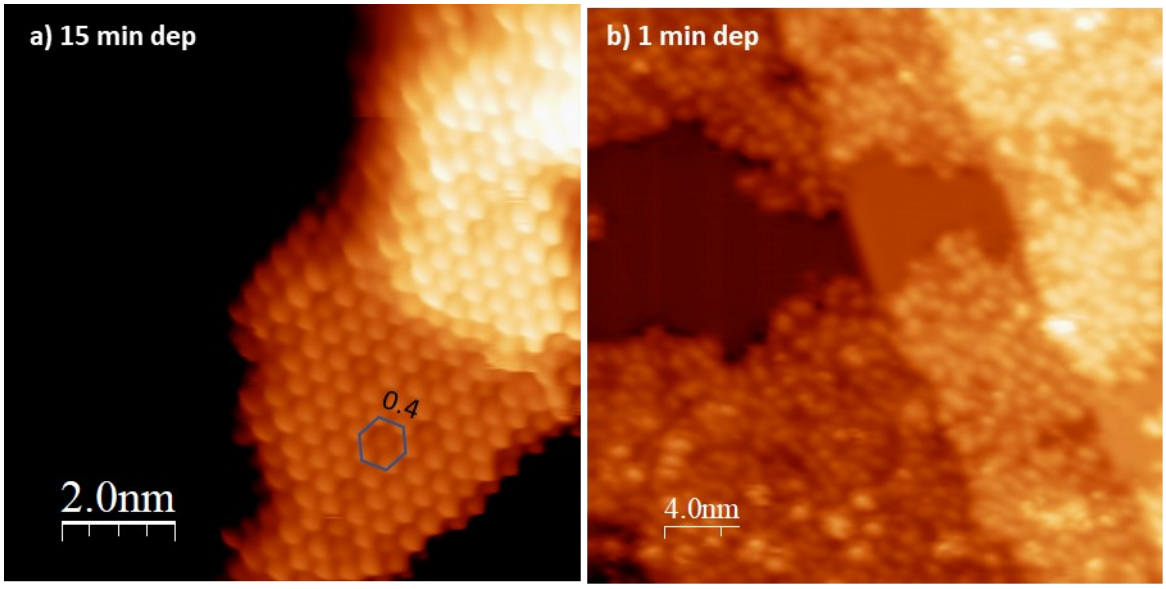

Figure 49. Structures observed on the surface after a) 15 minutes and b) 1 minute of deposition time keeping the substrate at -100°C. 15-minute deposition resulted in what appears to be disordered/multilayer of AB005 molecules (a) with dimensions that were inconsistent with those found in previous images of the surface at RT deposition.

CyPd forse?

The sample prepared with 15 minutes deposition was then annealed to RT for 5 minutes. Figure 50 shows the corresponding STM images. Here, I notice that the majority structure (panels a and b) consists of a complex arrangement in which a central diamond-shaped feature is surrounded by two sticks at the top and the bottom, respectively, and by 6 fainter lobes. It should be noted that I chose not to discuss the minority structure in panel c because it is observed only seldom and because it is more disordered and much less defined. While individual structures seem similar individual elements of previous preparations, it is more practical to focus on the ordered structures here.

Two unit cells with dimensions a=1.2 nm, b=2.5 nm and were identified depending on the orientation of the longer lattice vector (-12° or sometimes at +24° off <1-10>). They have the same dimensions within experimental error and in both cases the lattice vectors form an angle of 72° with respect to each other. However, these unit cells are not mirror images of each other because their orientation is not the same if the <1-10> direction is used as a line of symmetry. As for some more internal dimensions within the unit cell, the top and bottom sticks measure at around 1 nm in length and the

diamond is around 0.8 nm long. Given the dimensions of the unit cell, the measurements and appearances of the individual elements in the unit cell, it is reasonable to consider that the diamond is made of two Phe-pyr units coupled together like in the cross-coupling case (section 5.3.3) albeit arranged in a slightly different way. The sticks meanwhile could be the same bi-phe-pyr units in the cross-coupling case [102].

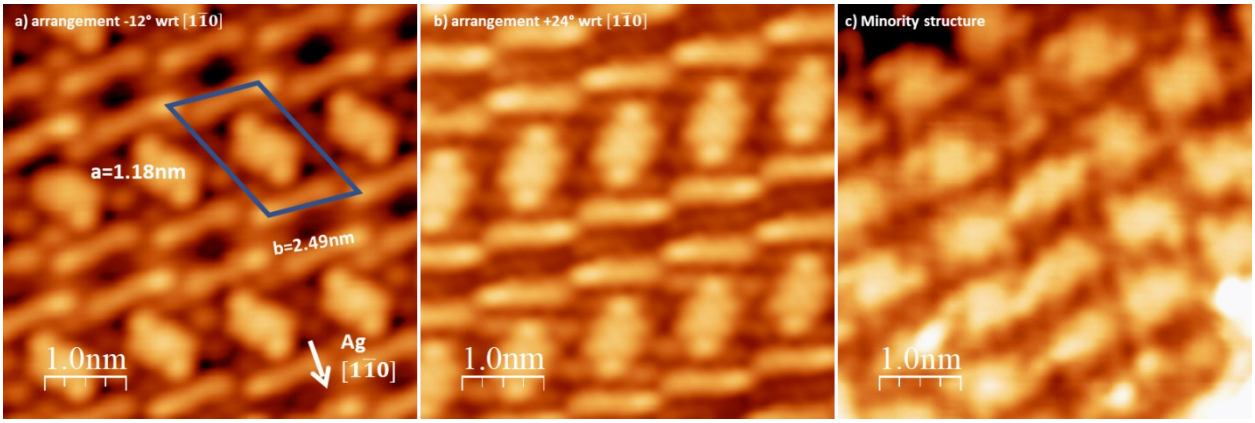

Figure 50. Structures observed after annealing the LT deposition for 5 minutes at RT. Panels a) and b) are teh self-assembled structures of CyPd while panel c) shows an amorphous monolayer.

The bias dependence the self-assembled structures in Figure 50a and b were also investigated and shown in Figure 51. Overall, the structures are stable up to ±2 V and I observe noticeable topographical differences only at the highest positive bias, as it is shown in Figure 51 for the 24° case. The bottom part of the figure reports the line scans cut along the lines marked in ±500 mV bias image, showing the changes in the apparent height of the structures. In general, a gradual decrease in apparent height is observed for very high bias settings (positive or negative). On the other hand, at the lowest bias the diamond features result as formed by 6 lobes, the top and bottom of which are brighter than the others. This is reflected in the line scans (2), cut parallel to the long direction of the unit cell. The last set of line scans (3) shows that the sticks are comprised of three balls of different apparent height, making the stick appear lopsided/tilted. Just like the middle part of the unit cell, the sticks undergo a significant change in morphology at high positive bias (+1500 and +2000 mV) becoming less resolved. The bias dependence of the self-assembly oriented at -12° behaves in the same way. I only remark that the tallest apparent height is observed at ±300 mV. Shortest apparent height is maintained at the highest bias for both positive and negative values.

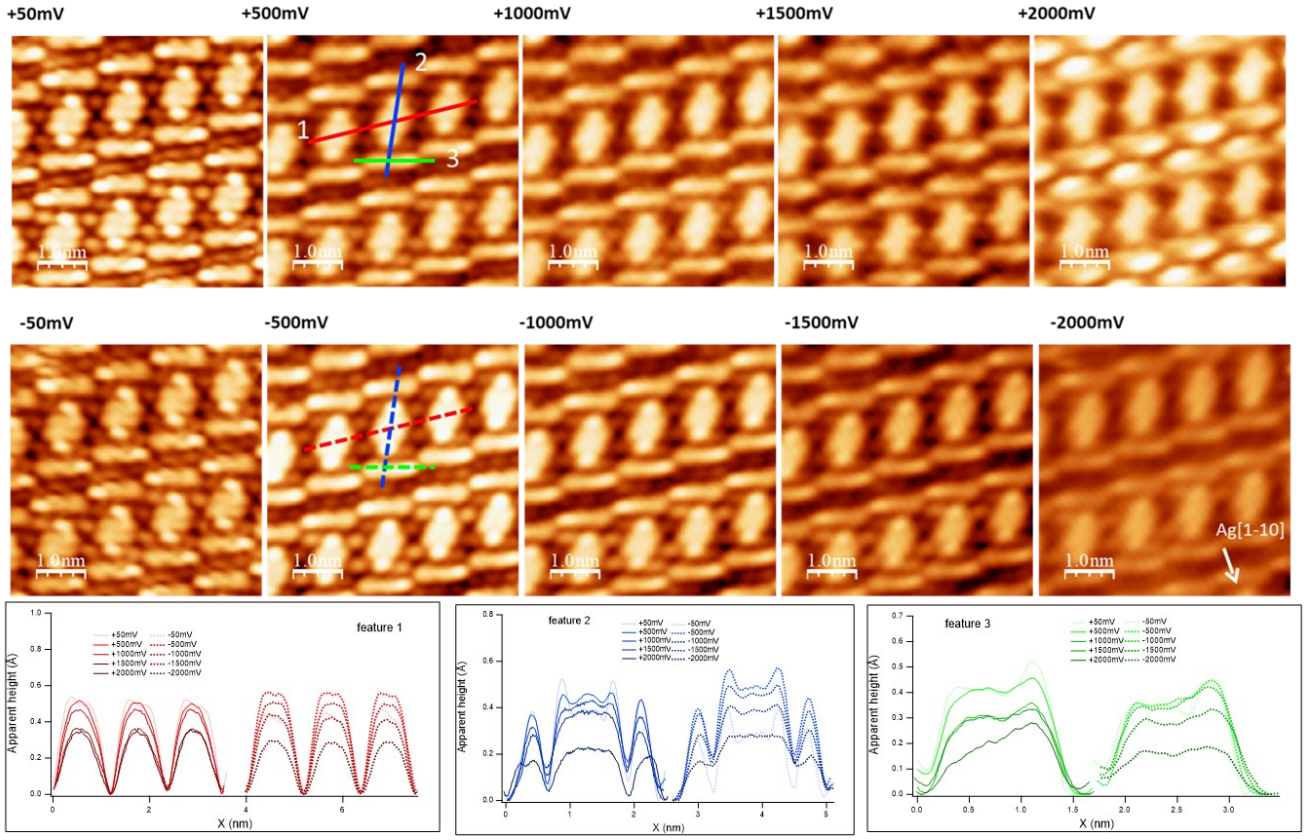

Figure 51. Bias dependence of the self-assembled structures formed by AB005 under LT deposition and RT annealing. The structure here is oriented +24° wrt Ag $[1\bar{1}0]$ *direction. Lower bias ranges show a few substructures and features of the suspected molecule especially in the middle of the structure. Higher biases result in the loss of fine structures in the line scans. The apparent height profile taken along the limescans marked in the STM image at 500 mV are shown below.*

CyPd ?

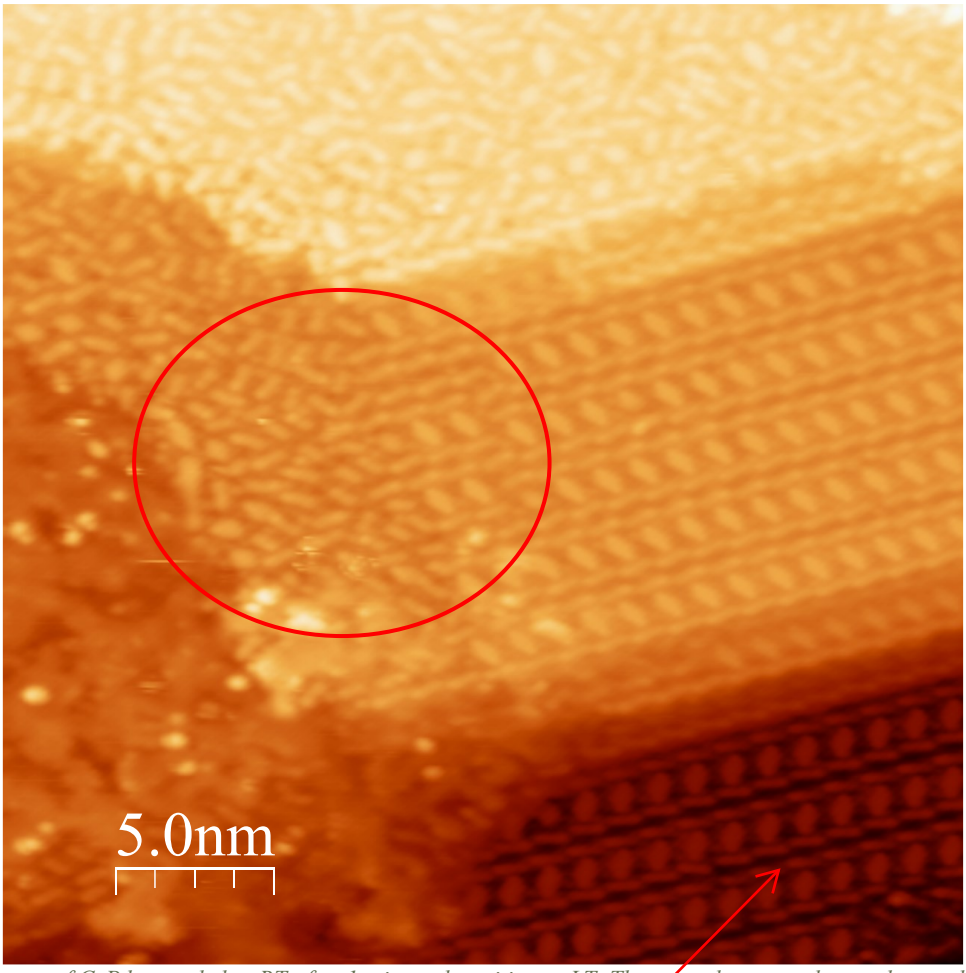

Figure 52. STM image of CyPd annealed to RT after 1 minute deposition at LT. The central terrace shows what could be a transition from the amorphous monolayer encircled in red (with features similar to those observed in CyPd deposited at RT in the previous chapters) to an ordered structure only observed when CyPd is deposited at LT and annealed back to RT.

Non ho la immagine

I would still like to mention some more observations that relate to the self-assemblies I have observed up to this point. First is that even though the same ordered structure was observed in both 1- and 15-minute deposition times after annealing to RT, the preparation of 15 minutes deposition yielded the ordered structure as the majority structure meaning that there was far more coverage of the ordered structure than the amorphous one. For the 1-minute deposition the situation is flipped where the amorphous structure dominates and the ordered structure only start to appear more regularly after annealing for an extended period at RT, about an additional 15 minutes. In the 1-minute deposition, by annealing it I have observed local areas on the surface that showcase a transition from the amorphous to ordered self-assemblies as seen in Figure 52. Both disordered regions (upper terrace) and areas with a well-ordered pattern (bottom terraces) coexist on the surface. The latter is equivalent to those I already presented in Figure 50.

6.2 XPS RESULTS

STM data are complemented by XPS experiments performed with synchrotron radiation. At variance with the STM preparations, deposition of CyPd was done with the substrate at 200K and the sample was then annealed for 5 minutes at RT. Figure 53 reports the Br 3d, Cl 2p, C 1s, N 1s and Pd 3d regions. The bottom spectrum refers the sample at LT while the upper traces were recorded after annealing. The spectrum corresponding to saturation coverage for deposition at RT is also reported for comparison (dashed red trace). I notice that at LT (orange solid line), the Br3d region shows a major

doublet at 68.3/69.3 eV, corresponding to Br-Ag bonds, and a minor one at 70.7/71.7 eV, indicating that a small fraction of C-Br bonds is still present. This is indicative that a fraction of molecules is not fully dibrominated yet. The C1s region at LT deposition also shows both a slight upshift and a broader shape compared to RT deposition.

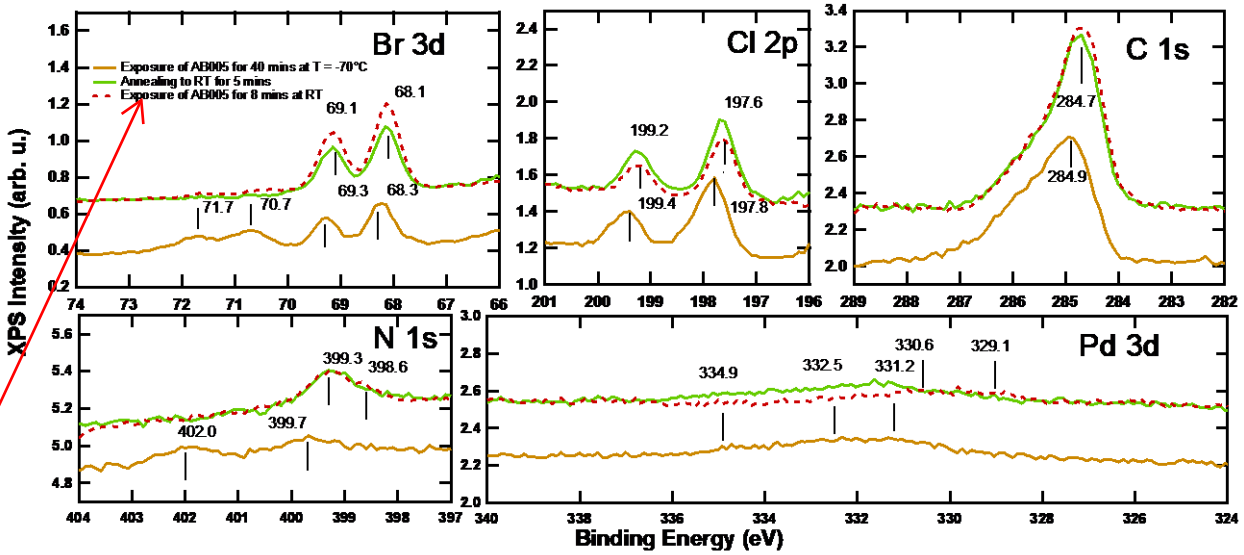

Figure 53. XPS spectra of Ag(110) sample after exposure to AB005 at T= -70°C for 40 mins (orange dash-lines). The sample was then annealed to RT (green dash-line) staying for 5 minutes, being compared to Ag(110) after exposure to AB005 at RT (red dash-line). Panels correspond to regions: Br 3d, Cl 2p, C 1s, N 1s, Pd 3d, hv = 515 eV, PE = 25 eV.

CyPd ?

CyPd ?

Upon annealing to RT, the XPS spectra are almost identical to those recorded upon RT deposition both from the point of view of the peak shape, while only slight variations in the Cl and Br intensity are observed. I also remark that the total C 1s intensity is not significantly diminished upon annealing, indicating a similar total coverage at 200 K and at RT. This information suggests that, from a chemical perspective, the annealed sample that was deposited at LT is equivalent to the sample deposited at RT, in spite of the different geometry observed by STM in the two cases. The common features seem to be the short sticks and diamonds, which are present in structure C in the RT preparation and appears in the present experiment both in the ordered and disordered arrangements.

One final consideration is about the Pd 3d region, in which I do not see significant intensity corresponding to the Pd lines (expected at 335 and 340 eV). This is indicative that Pd is diffusing below the crystal also at 200 K. Though it is quite unexpected, I should consider that the STM images indicate that fragmentation of the molecule is possible already at low T and that the spectra refer to a (sub)-ML coverage, as inferred by comparison the intensity of the RT spectra. Further investigation, repeating the LT deposition up to the achievement of a thick CyPd layer would be necessary to verify this point.

Note that due to the similarities between the XPS of CyPd as it is annealed to RT and in section 5.1 (and therefore the chemical nature of the species on the surface), it is unclear what exactly is the composition of the central part of the unit cell. This is assuming that the molecule splits apart as it was hypothesized in the previous preparations at higher temperature. Even though a clean or reconstructed surface such as ones found in the RT deposition of CyPd cannot be found, it is still clear that the halogens dissociated and continued to interact strongly with the Ag substrate just as was speculated for RT deposition of CyPd [84,102].

For now, I would like to propose what could be a plausible model given the possible dissociation and cross coupling of the molecular fragments and dimensions of the features on the surface. I propose the

following coupling configuration in Figure 54. The model accounts for the dangling bond that we think persists from the dissociation of the molecule and the repulsion that might occur with the pyridine groups (hence they face outward). It should be noted that the model has yet to be confirmed by calculations or models at the time of writing, but this proposed configuration has already been mentioned to our partners in UNIMIB and would work on this model in the soonest possible opportunity.

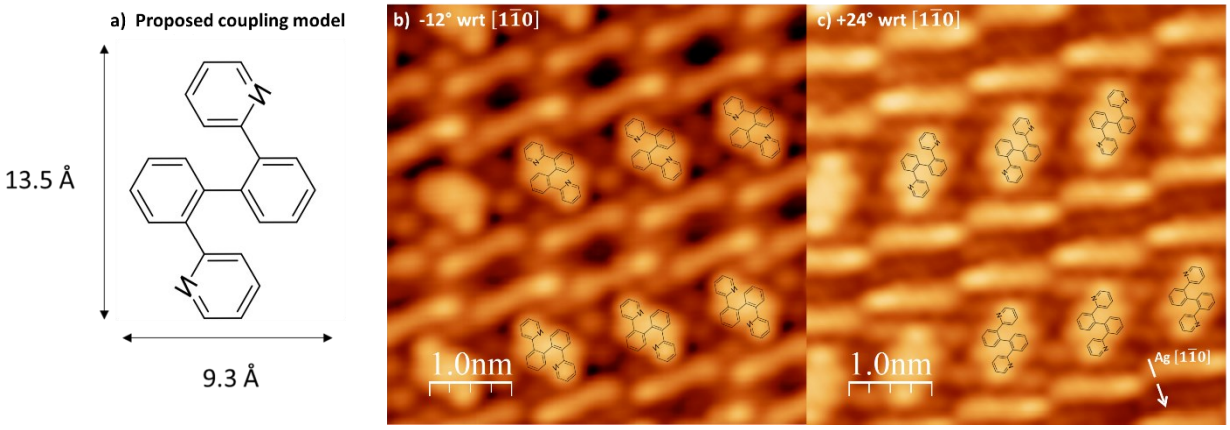

Figure 54. A proposed model (a); untested) for the self-assembly after RT annealing of the LT deposition of CyPd (b and c).

PD-CYCLOMETALLATED COMPLEX [(2-PHENYLPYRIDINE)PD(*M*-CL)]$_2$ (CYPD_2) ON AG(110)

The last precursor molecule I investigated in my thesis is the non-brominated version of CyPd, [(2-phenylpyridine)Pd(μ-Cl)]$_2$ (CyPd_2), which I deposited on Ag(110) at RT.

Looking at CyPd_2 is beneficial because it should help further clarify a couple of things that arose from CyPd. First, it would be interesting to know how much of the reconstructed surface in the previous experiment was influenced by bromine, chlorine, or both. Second, how does the morphology and chemistry of this molecule and substrate differ from CyPd/Ag(110)? I previously proposed that CyPd readily fragments on the substrate and depending on the conditions, would further undergo cross-coupling along with the Ag substrate undergoing reconstruction. ([84,102]) Does also CyPd_2 fragment on the surface? And how do the fragments arrange, since the Phe-Pyr units have one anchoring point less that CyPd? Finally, does Pd behave as for CyPd_2?

I underline that I performed these experiments as last experimental activity in the Genova laboratory, hence a full analysis is still running and the level of interpretation is lower than for the CyPd results.

6.3 XPS RESULTS FOR CYPD_2 ON AG(110)

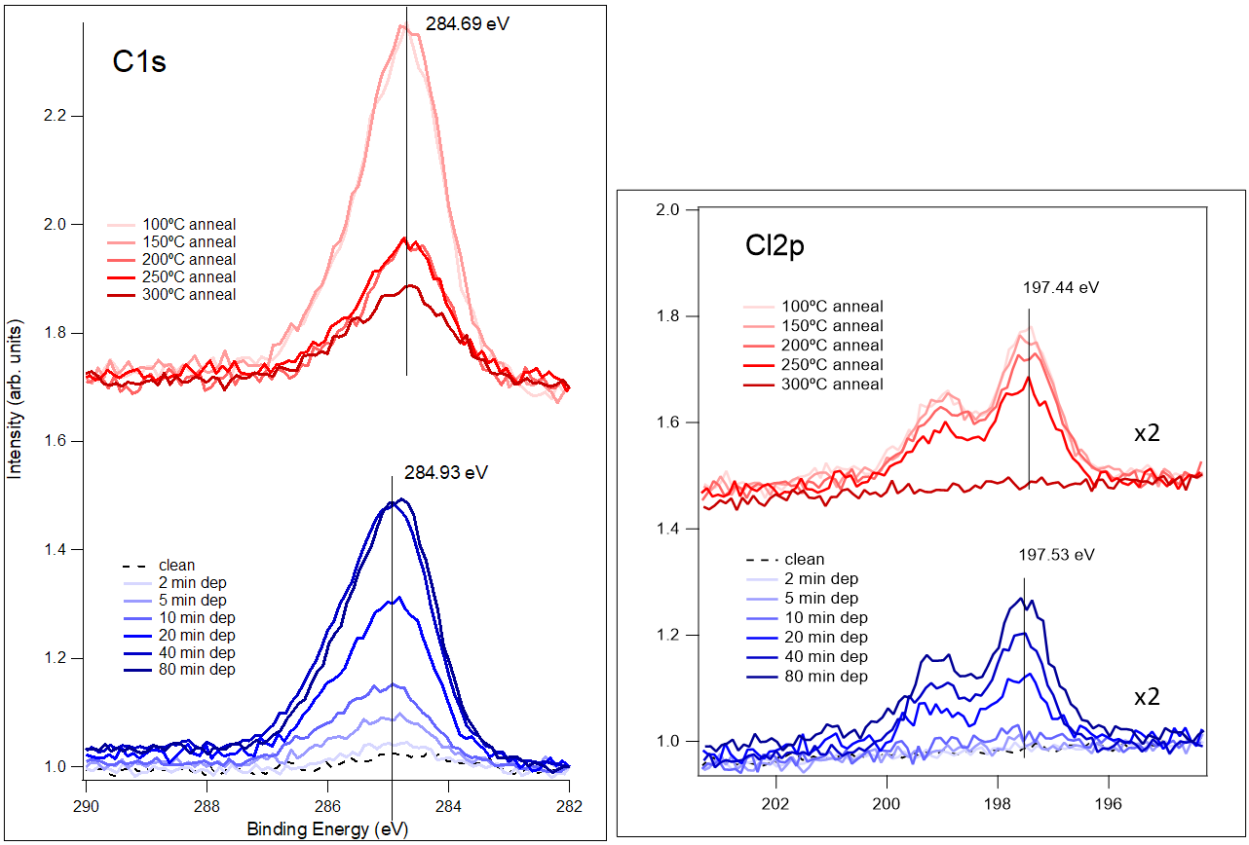

Figure 55.Uptake (blue traces) and annealing (red traces) of carbon and chlorine for CyPd_2. Cl2p signal is given a x2 multiplier for visualization

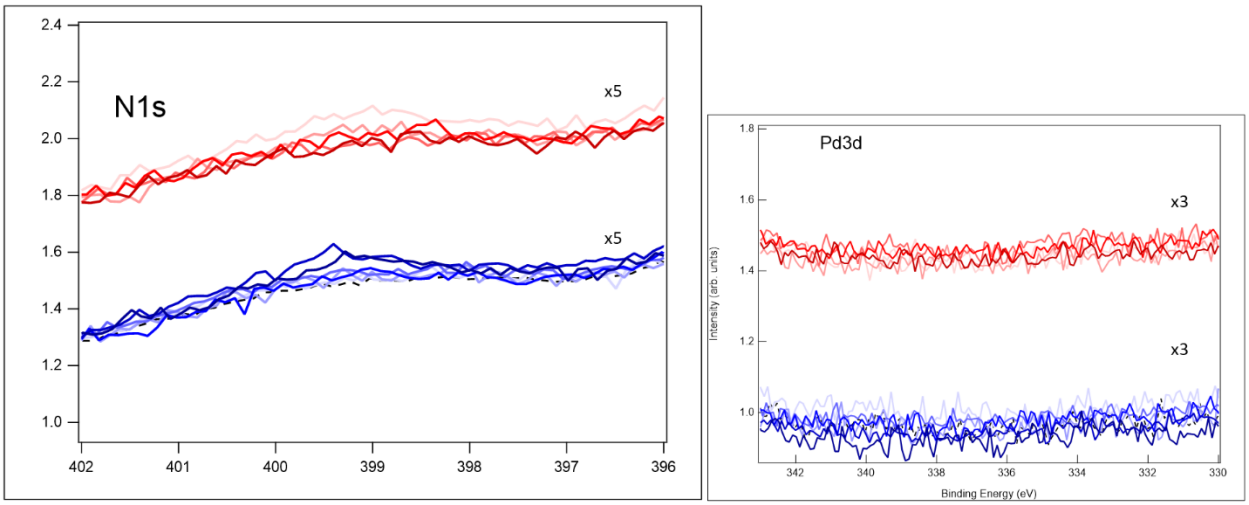

Figure 56. Uptake (blue traces) and annealing (red traces) of nitrogen and palladium for CyPd_2. N1s signal is given a x5 multiplier while Pd3d was given a x3 multiplier for visualization

I first looked at the uptake/deposition of CyPd_2 on Ag(110) at RT and subsequent annealing using XPS. Figure 55 shows the C 1s, Cl 2p and Figure 56 shows Pd 3d and N 1s regions recorded during an uptake experiment (bottom, blue traces) and following step-annealing (top, red traces). Just like with CyPd, there is a slight shift in the C1s spectra to lower binding energy after annealing and the overall shape of the C1s spectra suggests multiple components as well. Te position of the Cl2p suggests a metal-Cl bond just like like in CyPd. Finally, Pd is also absent here. This absence points to possible fragmentation similar to what happened to CyPd.

In Figure 57 I report the total C and Cl intensity during the uptake. I notice that the saturation coverage is achieved after 80 minutes deposition time. However, the peak growth with exposure is not the same for carbon and chlorine. Indeed, the uptake for carbon increases faster than the one of chlorine and reaches the maximum already after 40 minutes deposition. Chlorine on the ot her hand does not have a well-defined point of saturation. The stochiometric ratio of carbon to chlorine varies depending on the deposition time, being much in favor of C for short doses and moving close to the ratio of 11:1, which reflects the composition of the molecule, after 80 minutes exposure. It was not possible to effectively detect a Cl2p signal until after 5 minutes of deposition time.

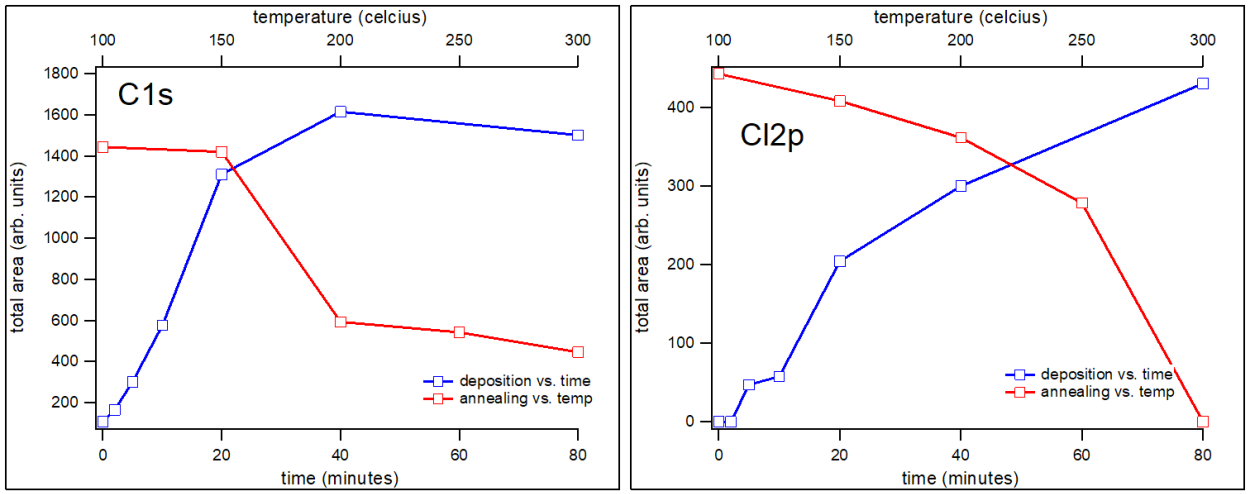

Figure 57. Uptake and thermal evolution following the concentration of carbon and chlorine on the surface

The excess of C in the intermediate doses could be due some contamination of the substrate, since C segregation may easily occur. Degradation of the molecule upon heating has been ruled out for the same reasons discussed for CyPd. Furthermore, since Cl is lighter than Phe-Pyr units, if fragmentation occurred into the crucible, I would expect an excess of Cl rather than of C on the surface.

Annealing the CyPd_2 layer in steps of 50°C increments shows a different behaviour for carbon and chlorine, which reproduces what already observed for CyPd. The C 1s signal drops significantly above 150°C and then it remains roughly stable up to 300°C. On the other hand, initially chlorine decreases much more slowly than carbon, and it drops in intensity above 250°C. In my previous experiments on CyPd/Ag(110), I observed that the halogens desorb last upon annealing the system (Figure 31) while the organic fragment desorbs sharply above 150 °C. This behavior is consistent with the one reported here for CyPd_2 and strongly suggests that also CyPd_2 dissociates upon interaction with the metal surface. Similarly, also the Pd signal is absent, indicating that it diffuses into the crystal.

I performed follow up experiments with the intention of passivating the surface of Ag(110), which might prevent the migration of Pd into the bulk material. As a first attempt, I tried to increase the Cl coverage at the surface. To do that, I deposited CyPd_2 at saturation coverage (80 minutes) and desorbed only the organic part by annealing to 250°C. Then I performed a subsequent deposition for another 80 minutes. XPS spectra reveal that the organic component was successfully desorbed by the almost complete disappearance of the C 1s signal while the Cl 2p intensity reduced by approximately a factor of two. However, also after the second dose, Pd was not seen again (spectra not shown).

6.4 STM Results for CyPd_2 on Ag(110)

I also checked CyPd_2 on Ag(110) just like what was done previously with CyPd. Given the behavior I observed in XPS, it would be interesting how CyPd_2 compares with CyPd morphologically. Figure 58 shows CyPd_2 on Ag(110) after annealing at 100°C. Some familiar structures appear on the surface such as a self-assembly on the upper terrace and extensive Ag reconstruction on the lower terraces. The presence of reconstruction is significant because this meant that for this system, chlorine was predominantly responsible for the reconstruction. Also, upon closer inspection, the self-assembled structures on the upper terrace have a different morphology than CyPd. I suspect that CyPd_2 not having bromine, and therefore fewer dangling bonds after possible dehalogenation, changes the interaction of CyPd_2 with the substrate and the resulting self-assembly. It should be noted that this interpretation is still preliminary and as of the time of writing, more possible models are being considered.

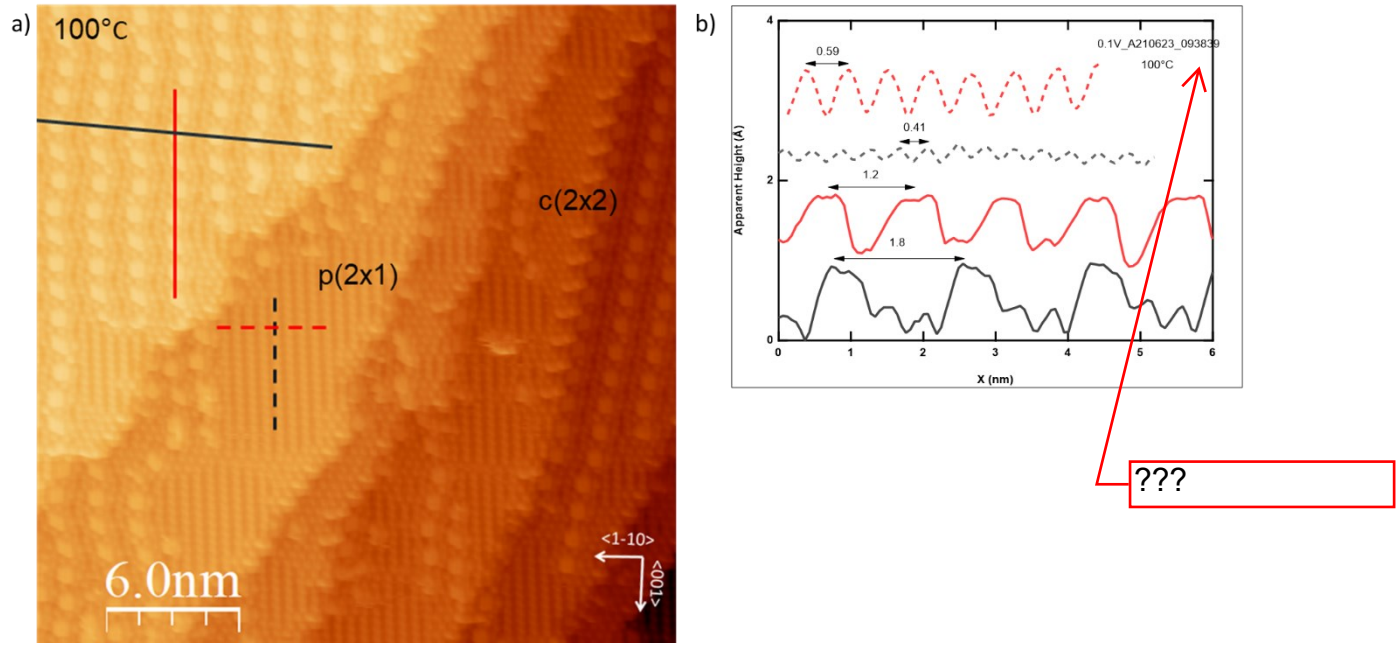

Figure 58. a) Overview of CyPd_2 on Ag(110) deposited at RT and subsequently annealed to 100C and b) corresponding linescans of the self-assembled structures and surface reconstruction.

7 APPENDIX

I would like to add a section of this dissertation detailing the work that I did with the Nanophysics Laboratory group in the Centro de Física de Materiales (CFM) located in the University of the Basque Country (UPV), Donostia-San Sebastian, Spain. I got involved in one of their projects as part of my internship for 10 weeks (two and a half months). The project in question concerns the synthesis and characterization by LT-STM of TM-coordinated cyano functionalized chiral graphene nanoribbons (Co+CN-chGNRs).

The context for the study is similar to what I have already enumerated in this dissertation and elsewhere. The group also investigates other types of graphene nanoribbons grown by means of a bottom-up approach and using different precursor molecules to form ribbons with different geometries and therefore edge sites and electronic structure. They have previously studied chiral GNRs that has a (3,1) edge site configuration (3 zigzag 1 armchair) synthesized using a DBBA precursor on Au(111) [103,104]. Previously, they investigated the pristine GNRs using LT-STM and XPS (morphology, electronic band structure, etc.) and also the stability of these GNRs when exposed to a controlled oxygen atmosphere and in air. [38,105] A logical progression of this study was to look at similar structures with additional functionalization and depending on the functional group, possible coordination with metal atoms. I entered the project specifically when they would be investigating cyano-DBBA based chiral GNRs coordinated to Co^{2+} atoms on Au(111). The investigation includes inspecting the morphology of the nanoribbons, determining the electronic structure of each type (pristine, mono, and double Co^{2+}coordinated ribbons) and if the coordinated and un-coordinated structures interact with oxygen. It should be mentioned that the results stated here are preliminary and further experiments could be conducted like XPS or ARPES to compliment the STM and STS data.

7.1 PROCEDURE

The experimental procedure for producing the nanoribbons is the same as in other experiments involving the formation of extended 2D carbon nanostructures by a bottom-up approach on a metallic substrate. The precursor molecule selected here is 2,2'-dibromo-9,9'-bianthracene (see Figure 59). The pristine/unfunctionalized molecule has been previously used to synthesize 3,1 chiral GNRs taking advantage of the same surface-assisted Ullmann coupling reaction as before [38]. The resulting pristine GNRs in this paper have been thoroughly studied regarding their morphology and band structure, as well as investigated for any interaction with oxygen. These GNRs are stable only up to certain exposure conditions to oxygen and react readily when exposed to air. [38]

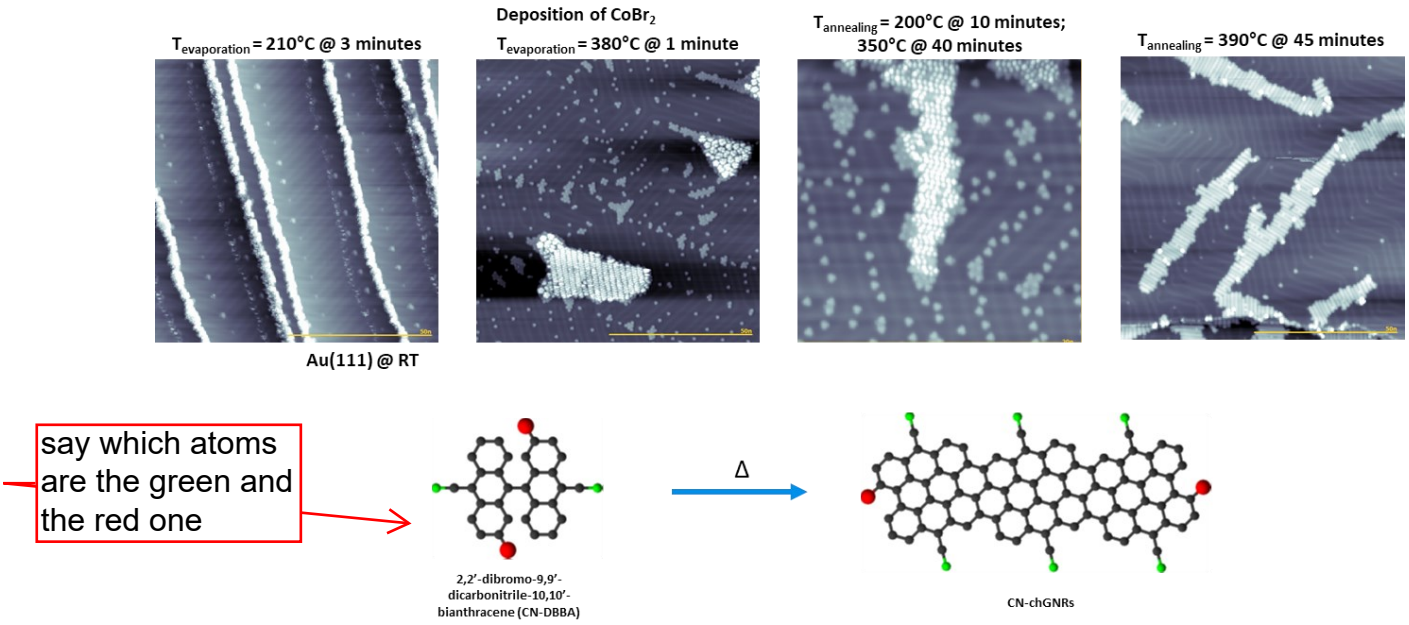

Figure 59. Synthetic procedure to form Co-coordinated CN-chGNRs on Au(111). The DBBA precursor molecules were deposited on the substrate that was kept at RT, the metal salt (CoBr2) deposited right after. The whole system was step annealed to facilitate the polymerization of the precursors, the CN-chGNRs formation and the Co coordination between the ribbons (seen in more detail in section 7.2.1).

The precursor molecules used in this work are functionalized with two cyano groups at the edges. The idea is that the cyano groups would act as ligands coordinating to the Co ions on the substrate. To begin, the molecules were evaporated (T=210°C) on Au(111). Just like in the previous experiments, the substrate was held at RT. The total deposition time for DBBA was 3 minutes. After inspecting the surface to confirm the deposition of DBBA, $CoBr_2$ was evaporated on the substrate (T_{evap}=380°C) for 1 minute, keeping the substrate at RT. The system was then step annealed with the following protocol: 200°C for 10 minutes (polymerization step), 350°C for 40 minutes (cyclodehydrogenation step), and finally 390°C for 45 minutes to clean up the substrate removing possible contamination from the preparation chamber as seen in Figure 59. It was previously established that the nanoribbons were stable above 400°C. We investigated the system using STM (morphology) and STS (electronic states). The system was then exposed to oxygen with the sample at RT. O_2 was dosed to 1e-7 mbar and the system was exposed for 30 minutes (xxx Langmuirs). We investigated the system again using STM and STS to figure out any changes in the GNRs electronic structure.

7.2 PRELIMINARY RESULTS

In this section I will briefly discuss the general results obtained from the measurements on the Co+CN-chGNRs system. The methodology presented earlier yielded three different species on the surface. We were able to see "pristine" CN-chGNRs, GNRs that are coordinated to Co only on one side, and GNRs coordinated with Co on both sides. Images and spectra shown here are taken with a CO-functionalized tip.

Functionalizing the tip takes advantage of the fact that the p orbitals on a molecule such as CO has a much narrower cross section and effectively "becomes the tip." A CO tip is much more sensitive to the valence and conduction bands of molecules on the surface for example. This is achieved by dosing the STM chamber with CO while under LHe (4K). After dosing and before scanning the molecules, a

CO can be picked up by scanning a clean area at a low bias (-500 mV) until a change in contrast is observed. The molecules were then imaged as one would with a metallic tip.

7.2.1 Co-coordinated CN-chGNRs on Au(111) – STM

It is possible to see all three species in one self-assembly of nanoribbons on Au(111) as shown in Figure 60. An easy way to spot each one is by measuring the separation of the nanoribbons. The Co coordination induces a significant separation between two GNRs that is noticeable even just by visual inspection. Bond-resolved STM (BR-STM) images show the internal bonding structure of the nanoribbons and further highlight the difference between each of them. Figure 60 shows BR-STM images of the different types of nanoribbons.

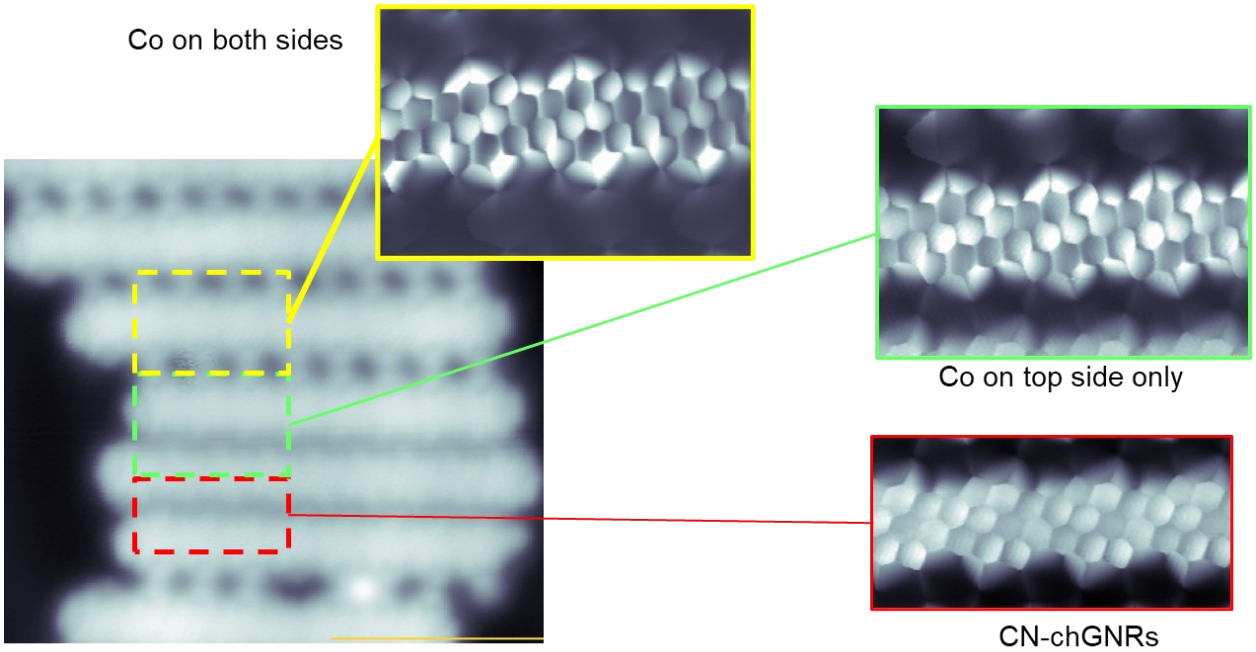

Figure 60. Bond-resolved (BR) STM images of the GNRs: CN-chGNRs (no Co coordination) in red, CN-chGNRs with Co coordination on one side only in green, and CN-chGNRs with Co coordination on both sides in yellow.

We investigated the electronic band structure of each nanoribbon type using STS in order to identify the positions of the valence and conduction band and define their band gap value. Pristine CN-chGNRs have a band gap of ~980 mV while coordination with a TM like Co shrinks the band gap considerably. The band structure of the mono-coordinated GNR in Figure 61c shows a state at -400 mV, which could be assigned to the valence band (HOMO) and a state at +70 mV, which could correspond to the conduction band (LUMO), leading to a bandgap of 470 mV. In comparison, CN-chGNRs were found to have a VB at -713 mV and CB at +273 mV. The dI/dV maps taken at constant height (Figure 61) confirm that the LDOS for the mono coordinated GNRs correspond to the assigned VB and CB.

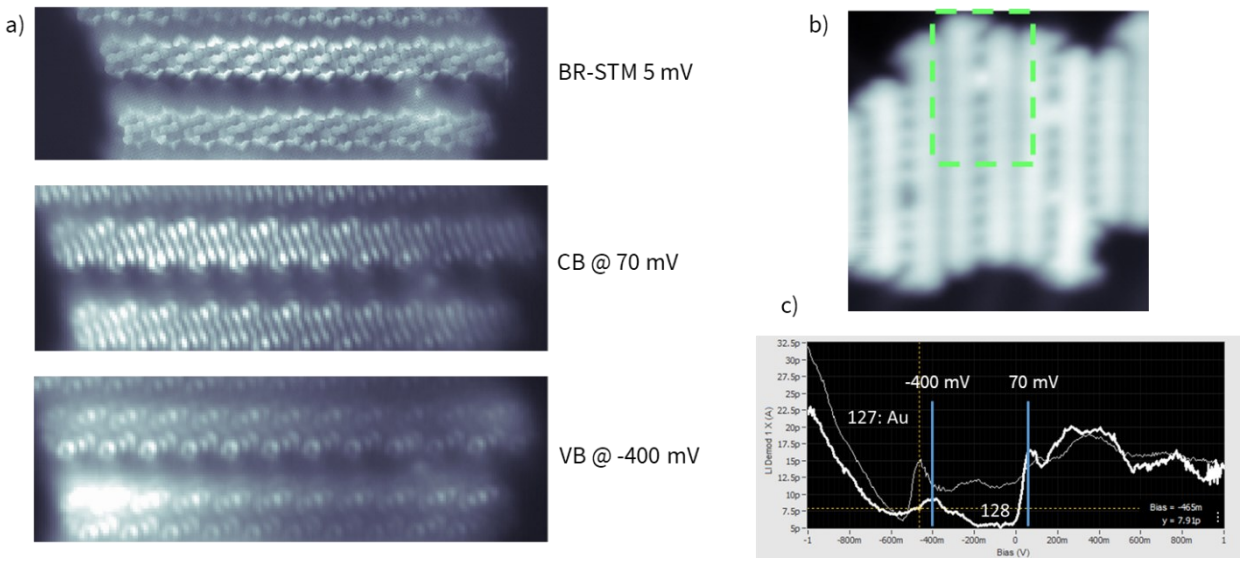

Figure 61. a) BR STM and dI/dV maps of the conduction and valence bands of the mono coordinated GNRs taken at constant height and with a CO functionalized tip, b) the same nanoribbons in a) in normal mode (morphology) with the dI/dV maps taken on the ribbons enclosed by the green outline and c) the spectra on the right mark the local density of states suggesting the position of the energy gap for the GNR.

7.2.2 Reactivity of Co+CN-chGNRs on Au(111) with oxygen

After oxygen exposure, we did not observe any changes in the morphology of all three species of GNRs. We noticed though that taking dI/dV spectra and dI/dV maps of the GNRs became more difficult. The electronic structure of pristine CN-chGNRs remains unaffected as expected given the level of oxygen exposure. In the case of mono coordinated GNRs we measured a downshift of the VB from -400 mV to -710 mV, equal to the VB of the pristine CN-chGNRs.

Double coordinated GNRs seem also to be unaffected, but due to the difficulty of measuring dI/dV spectra, eventual changes induced by oxygen could not be tracked.

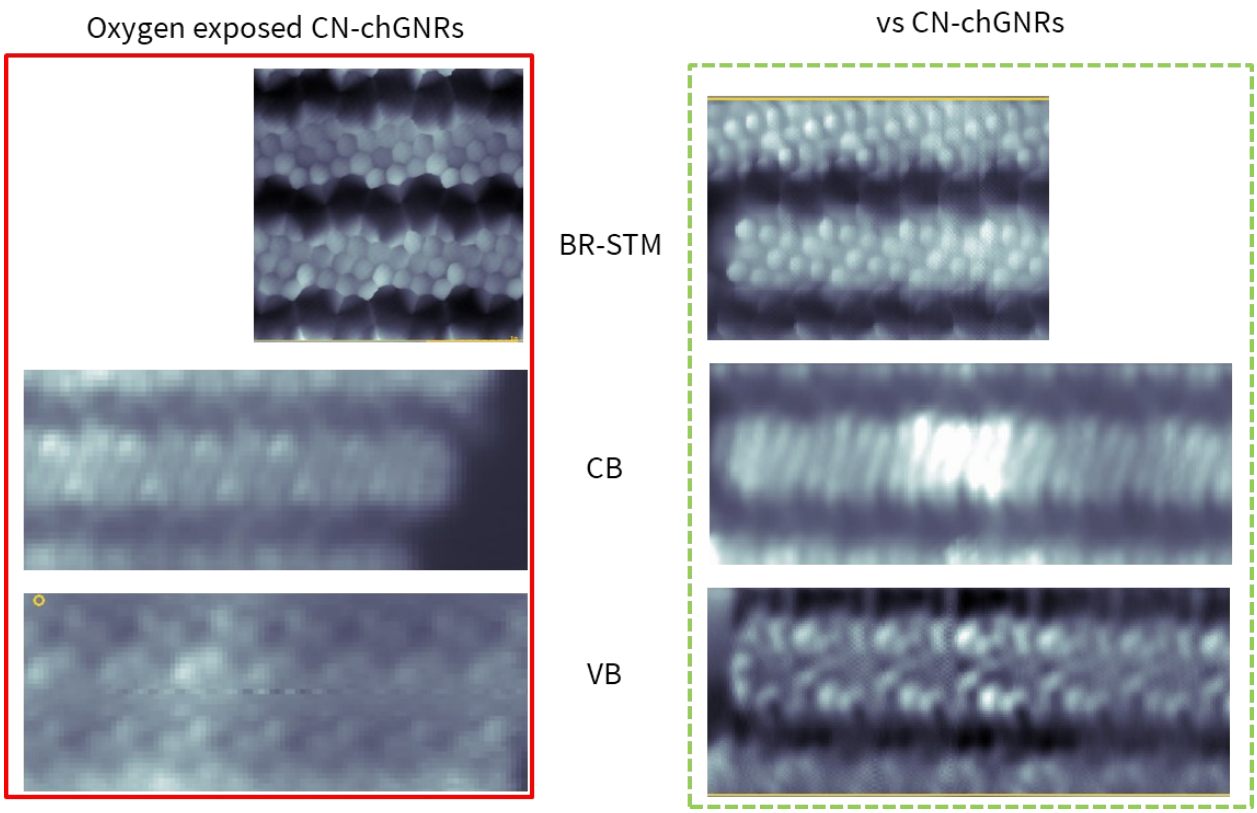

Figure 62. BR-STM and dI/dV maps taken with a CO functionalized tip in constant height mode comparing oxygen exposed (left) to not exposed (right) CN-chGNRs without Co-coordination. Notice that the dI/dV maps show no clear difference in the CB and VB before and after exposure to oxygen.

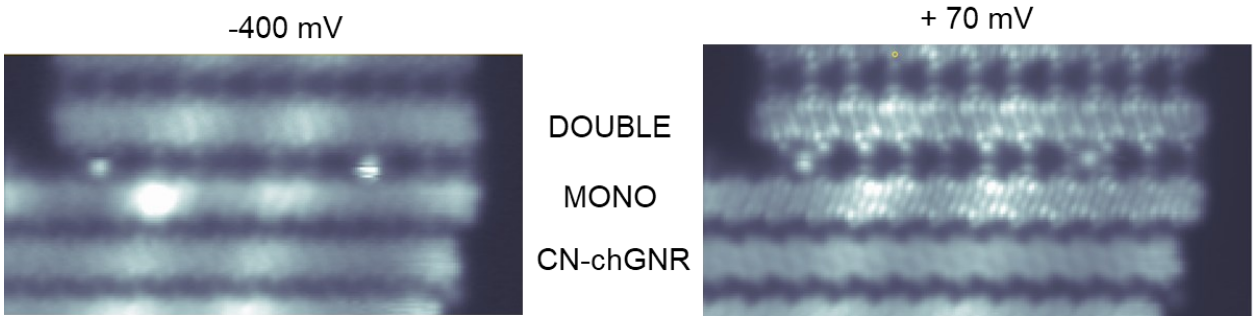

Figure 63. dI/dV maps taken after oxygen exposure on CN-chGNRs, mono and double coordinated CN-chGNRs. Notice how the VB of the mono coordinated GNRs seems to disappear after exposure while the CB appears to be unaffected.

To summarize, for the entire duration of my internship, I, with the rest of the Nanophysics group successfully synthesized Co-coordinated CN-chGNRs using CN-DBBA on Au(111). The electronic band structure of all possible species of Co-coordination were determined with noticeable differences with the pristine GNRs. Changes in the GNRs upon oxygen exposure were not observed at first. However, some evidence points to a shift in the VB of mono coordinated GNRs. More experiments are required to reliably observe any changes induced by oxygen as well as to observe the system under more realistic conditions such as in air.

8 CONCLUSIONS AND PERSPECTIVES

At the end of my doctorate as stated in this dissertation, I have investigated multiple C-based nanostructures in terms of their morphology and chemical behaviour on a metal substrate. To achieve this, I studied these systems under UHV conditions both with the LT-STM and XPS. Because of the diverse nature of the carbon nanostructures studied, the goals for each experiment were slightly different. That being said, the overall intended outcome is the same. I studied the self-assemblies and other thermally-activated products of DBP, CyPd, and CyPd_2 on Ag(110) with the aim of correlating the structure observed on the surface with the precursor molecules. For DBP, which forms GNRs with a special edge-site sequence (two zig-zag and one armchair sites), I studied also the stability in a controlled oxygen environment.

All of the systems were studied by first depositing the precursor molecules on Ag(110) kept at RT and subsequently subjected to step annealing. The combined information provided by STM and XPS gave me a more complete picture of what was happening to each carbon nanostructure. In the case of CyPd, the experimental data were also used to model what was happening on the surface using DFT calculations. The DFT calculations provided by our partners corroborated the model that I proposed for CyPd on Ag.

With all the findings in the past three years, I conclude the following:

I have shown that graphene nanoribbons synthesized from 1,6 DBP on Ag(110) reacts with oxygen under controlled conditions. I have shown that the GNRs/Ag(110) system undergoes significant modification upon oxygen exposure, especially at higher temperatures (300°C). Specifically, the GNRs appear more disordered and separated and the surface contains Ag-O complexes positioned in between the GNRs and at clean Ag patches. These results suggest that care must be taken due the modification of supported GNRs and the substrate upon exposure to reactive gases. This insight opens important perspectives for the optimization of the transfer procedure of the nanoribbons on a different substrate, as well as for operating nanostructure-based devices under realistic conditions. These results, along with other characterizations such as the electronic band structure of these GNRs, were published in ref. [37].

Next, I was able to present the first investigation of the self-assembly of Pd-cyclometallated compounds deposited on a noble metal surface. The **CyPd**/Ag(110) system exhibited an unexpected and peculiar behavior. I reported an ordered self-assembled layer of paired rows of lozenge-shaped features with interstitial dots in between them. A deeper analysis and a mechanistic study, based on density functional theory calculations and corroborated by the experimental findings, indicate that the molecule dissociates due to the interaction with the metal substrate. The halogen atoms bind to the surface; the two phe-pyr fragments saturate towards an Ag adatom and, under certain experimental conditions, may undergo cross coupling and form diphenyl-bipyridine molecules; the Pd atoms diffuse inside the Ag substrate. Therefore, the formation of a C-based network at the surface occurs upon a drastic modification of the system. The atomistic details of reaction steps reveal the active role played by the metal substrate in promoting the chemistry of the deposited Pd cyclometallates. The first pat of this research is published in ref.[84]. In a second publication [102], I focus on what happens to the Phe-Pyr fragments when, following CyPd deposition at higher flux and achievement of a full ML coverage, undergo the cross coupling reaction. The model developed with the help of DFT suggests that, initially, Ag atoms form the organometallic complexes $(Phe\text{-}Pyr)_2$-Ag. Eventually, a cross

part

coupling reaction occurs between the two equivalent fragments originating from the precursor molecule to produce $(Phe\text{-}Pyr)_2$. This process is thermally activated and competes with desorption of the organic fragments. I propose that it occurs through and intermediate step in which one Phe-Pyr unit of the organometallic complex flips into cis-position. The very good agreement between the simulated STM images of the initial and final configurations and the experimental ones supports the validity of our conclusions. I also discovered that the Ag substrate is deeply perturbed by CyPd adsorption. Halogen atoms released by the molecules bind to the substrate and promote a reconstruction, which is c(2x2) around the isolated $(Phe\text{-}Pyr)_2$ units and p(2x1) in areas where complete desorption of the organic part has occurred. This behavior suggests an active role of halogen species in the reorganization of the surface morphology.

I also performed complementary experiments on the parent molecule CyPd_2 for comparison. XPS spectra suggest a similar behaviour of CyPd_2 and CyPd. I observed similar desorption temperatures for the organic and halogen fragments and similar spectral shapes. This suggests that also CyPd_2 fragments upon interaction with the surface. The similar behaviour from the chemical point of view does no correspond to similar self-assembled geometries when observed with STM. Though my STM data are very preliminary and do not allow me to draw any conclusions yet, I hypothesize that the difference is related to the slightly different composition of the two molecules. In fact, CyPd_2 does not possess 2 bromination sites so that the Phe-Pyr fragments anchor to the Ag surface with only two bonds instead of three. This difference aside, significant surface reconstruction was also observed. This could be due to the remaining halogens in the system (Cl) continuing to modify the substrate like before. It must be stated that the observations for CyPd_2 are deemed preliminary results and require further investigation.

I believe that my findings open new perspectives for the potential uses of these carbon nanostructures. On one hand, we continue to see promise of GNRs in nanoelectronics applications even though their reactivity to oxygen needs to be considered. On the other hand, more complex systems like that of cyclometallated complexes CyPd and CyPd_2 exhibit unexpected chemistry that require further investigation. This is especially true if we imagine this class of molecules utilized as part of an on-surface catalytic or sensoristic structure. I see the possibility of further refinement of the GNRs by the possible introduction of functional groups or tweaking the morphology of the GNRs by forming products with different edge site configurations. For CyPd and CyPd_2, it would be reasonable to explore alternative substrates to observe the self-assembled molecules and to explore similar molecules like a cyclometallated complex with a different TM center or halogenation at a different position in the complex.

ACKNOWLEDGEMENTS

I would like to take the time to thank all the people who have been a part of my journey as a PhD student and researcher. It has been an even crazier three years since I finished my graduate studies and began my doctorate and looking back, there were those along the way who made the journey worthwhile. Since it would be impossible to mention everyone, I would like to acknowledge the people who have been most important in my career and in my life.

That said, I would like to thank:

Dr. Letizia Savio, for being my mentor and supervisor. She has been the driving force of our laboratory, keeping everything running smoothly and always checking up on us. I am grateful for her patience and understanding even during those times when I am not at my best. I am honored to have worked under her for over four years now. As I plan on moving on to different projects, I am thankful for all the support she has given me.

Dr. Marco Smerieri, for being my original mentor and one that I could credit as the one that got me into what I specialize in right now. I am thankful for everything that I had learned and experienced during my time in our lab.

Prof. Mario Rocca, for his continued support. Even though he is no longer my professor, he still invites us alumni to join activities with the current group of graduate students whether it is going out of town or watching an opera. I will always remember him looking out for us above and beyond what is expected.

Prof. Gianangelo Bracco and Prof. Luca Vattuone, for being a mentor like Dr. Savio even in your busy schedules. It was always nice to hear prof. Vattuone greet us every time he could pass by in the morning and makes time to discuss with us when we need his opinion.

Dr. Giovanni Carraro, for being the most reliable and dependable person behind the scenes in the laboratory. I am thankful for all of the times he stepped in and helped fix difficult problems, from interpreting and analysing data to fixing instruments. I also learned a lot from him from the tricks that could be useful in our experiments and his demonstration of managerial skills. There are a lot that would not work if not for his efforts as a part of the laboratory.

My colleagues: Simone, Ola, and Clement for all the times we spent together. I am thankful for them keeping up with my eccentricities.

My friends Kenneth and Yomki, for keeping in touch after all these years despite the distance and time difference. I wish them success in their careers and lives moving forward.

To Japhet, Tao, Paula, Profs. Corso and Oteyza and all the wonderful people I met during my time in San Sebastian. I learned a lot from the short time I spent there and I had an amazing time in the beautiful Basque country. I hope to see everyone again soon.

To my auntie Jaybee, her husband Robert and Jose for their continued support and being there for me to this day. I would not be in my position right now if not for them and I am eternally grateful for that.

To my uncle, grandmother and the rest of my family for their continued support and understanding even when I have been away for so long.

To my dad, to whom I am grateful for raising me to be the person I am today. I know I do not say much, but I am thankful and proud that I am your son. It has been different since mom passed away, but you remain strong and supportive all these years. I am also thankful for the time you finally visited and got to see the life I have made here so far and I am where I am now also because of you.

To Marija Stojkovska, for being my best friend and family away from my home. I honestly cannot imagine how my life could have been if I had not met you. We have been through so much all these years, moving from two countries, changing houses sometimes multiple times a year, going through and laughing over each other's heartbreaks, finding love and friendship everywhere we went, exploring new places, going to conferences together and of course, going through doctorate and finally making it at the same time. We share everything together and you really are like a sister I never had. I will never forget all the times we supported each other through our lowest points and celebrated each other's successes. I will never forget your patience and understanding even when I failed to be the friend that I should be. It breaks my heart knowing that at least for now, we are going to follow different paths in the coming years. But I do know that this is temporary and we will be reunited again. There are so many more things that can describe our relationship, but life would not be the same if not for that time we first got to know each other. I love you and I am looking forward to all the (mis)adventures ahead with you.

And finally, to my mom, for all the care and sacrifice that you had given out of love. I am who I am because of you. Even though life has other plans and you are not with us anymore, I know that you are here with us still. I dedicate this work to you and everything you had done for me.

I love you, ma. This is for you. Hanggang sa muli.

BIBLIOGRAPHY

[1] X. Li, X. Wang, L. Zhang, S. Lee, H. Dai, Chemically derived, ultrasmooth graphene nanoribbon semiconductors, Science (80-.). 319 (2008) 1229–1232. https://doi.org/10.1126/science.1150878.

[2] K. Nakada, M. Fujita, G. Dresselhaus, M.S. Dresselhaus, Edge state in graphene ribbons: Nanometer size effect and edge shape dependence, Phys. Rev. B. 54 (1996) 954–961. https://doi.org/10.1103/PhysRevB.54.17954.

[3] Y.C. Chen, D.G. De Oteyza, Z. Pedramrazi, C. Chen, F.R. Fischer, M.F. Crommie, Tuning the band gap of graphene nanoribbons synthesized from molecular precursors, ACS Nano. 7 (2013) 6123–6128. https://doi.org/10.1021/nn401948e.

[4] X. Wang, Y. Ouyang, X. Li, H. Wang, J. Guo, H. Dai, Room-temperature all-semiconducting sub-10-nm graphene nanoribbon field-effect transistors, Phys. Rev. Lett. 100 (2008) 100–103. https://doi.org/10.1103/PhysRevLett.100.206803.

[5] J. Baringhaus, M. Ruan, F. Edler, A. Tejeda, M. Sicot, A. Taleb-Ibrahimi, A.P. Li, Z. Jiang, E.H. Conrad, C. Berger, C. Tegenkamp, W.A. De Heer, Exceptional ballistic transport in epitaxial graphene nanoribbons, Nature. 506 (2014) 349–354. https://doi.org/10.1038/nature12952.

[6] C.N.R. Rao, K. Gopalakrishnan, A. Govindaraj, Synthesis, properties and applications of graphene doped with boron, nitrogen and other elements, Nano Today. 9 (2014) 324–343. https://doi.org/10.1016/j.nantod.2014.04.010.

[7] H. Chen, Y. Li, S. Liu, Q. Xiong, R. Bai, D. Wei, Y. Lan, On the mechanism of homogeneous Pt-catalysis: A theoretical view, Coord. Chem. Rev. 437 (2021) 213863. https://doi.org/10.1016/j.ccr.2021.213863.

[8] P. Sehnal, R.J.K. Taylor, L.J.S. Fairlamb, Emergence of palladium(IV) chemistry in synthesis and catalysis, Chem. Rev. 110 (2010) 824–889. https://doi.org/10.1021/cr9003242.

[9] A. Biffis, P. Centomo, A. Del Zotto, M. Zecca, Pd Metal Catalysts for Cross-Couplings and Related Reactions in the 21st Century: A Critical Review, Chem. Rev. 118 (2018) 2249–2295. https://doi.org/10.1021/acs.chemrev.7b00443.

[10] M. Mauro, A. Aliprandi, D. Septiadi, N.S. Kehr, L. De Cola, When self-assembly meets biology: Luminescent platinum complexes for imaging applications, Chem. Soc. Rev. 43 (2014) 4144–4166. https://doi.org/10.1039/c3cs60453e.

[11] M. Fanelli, M. Formica, V. Fusi, L. Giorgi, M. Micheloni, P. Paoli, New trends in platinum and palladium complexes as antineoplastic agents, Coord. Chem. Rev. 310 (2016) 41–79. https://doi.org/10.1016/j.ccr.2015.11.004.

[12] F. De Castro, E. De Luca, M. Benedetti, F.P. Fanizzi, Platinum compounds as potential antiviral agents, Coord. Chem. Rev. 451 (2022) 214276. https://doi.org/10.1016/j.ccr.2021.214276.

[13] V.W.W. Yam, V.K.M. Au, S.Y.L. Leung, Light-Emitting Self-Assembled Materials Based on d8 and d10 Transition Metal Complexes, Chem. Rev. 115 (2015) 7589–7728. https://doi.org/10.1021/acs.chemrev.5b00074.

[14] J. Kalinowski, V. Fattori, M. Cocchi, J.A.G. Williams, Light-emitting devices based on organometallic platinum complexes as emitters, Coord. Chem. Rev. 255 (2011) 2401–2425. https://doi.org/10.1016/j.ccr.2011.01.049.

[15] D.C. Powers, T. Ritter, Palladium(III) in synthesis and catalysis, Top. Organomet. Chem. 503 (2011) 129–156. https://doi.org/10.1007/978-3-642-17429-2_6.

[16] R. Mosteiro, A. Fernández, D. Vázquez-García, M. Lõpez-Torres, A. Rodríguez-Castro, N. Gõmez-Blanco, J.M. Vila, J.J. Fernández, Cyclometallated palladium diphosphane

compounds derived from the chiral ligand (S)-PhCH(Me)NMe2. Michael addition reactions to the vinylidene double bond, Eur. J. Inorg. Chem. (2011) 1824–1832. https://doi.org/10.1002/ejic.201000873.
[17] M.Y. Han, B. Özyilmaz, Y. Zhang, P. Kim, Energy band-gap engineering of graphene nanoribbons, Phys. Rev. Lett. 98 (2007) 1–4. https://doi.org/10.1103/PhysRevLett.98.206805.
[18] L. Jiao, L. Zhang, X. Wang, G. Diankov, H. Dai, Narrow graphene nanoribbons from carbon nanotubes, Nature. 458 (2009) 877–880. https://doi.org/10.1038/nature07919.
[19] D. V. Kosynkin, A.L. Higginbotham, A. Sinitskii, J.R. Lomeda, A. Dimiev, B.K. Price, J.M. Tour, Longitudinal unzipping of carbon nanotubes to form graphene nanoribbons, Nature. 458 (2009) 872–876. https://doi.org/10.1038/nature07872.
[20] X. Yang, X. Dou, A. Rouhanipour, L. Zhi, H.J. Räder, K. Müllen, Two-dimensional graphene nanoribbons, J. Am. Chem. Soc. 130 (2008) 4216–4217. https://doi.org/10.1021/ja710234t.
[21] P. Han, K. Akagi, F. Federici Canova, H. Mutoh, S. Shiraki, K. Iwaya, P.S. Weiss, N. Asao, T. Hitosugi, Bottom-up graphene-nanoribbon fabrication reveals chiral edges and enantioselectivity, ACS Nano. 8 (2014) 9181–9187. https://doi.org/10.1021/nn5028642.
[22] J. Cai, P. Ruffieux, R. Jaafar, M. Bieri, T. Braun, S. Blankenburg, M. Muoth, A.P. Seitsonen, M. Saleh, X. Feng, K. Müllen, R. Fasel, Atomically precise bottom-up fabrication of graphene nanoribbons, Nature. 466 (2010) 470–473. https://doi.org/10.1038/nature09211.
[23] M. Smerieri, I. Píš, L. Ferrighi, S. Nappini, A. Lusuan, C. Di Valentin, L. Vaghi, A. Papagni, M. Cattelan, S. Agnoli, E. Magnano, F. Bondino, L. Savio, Synthesis of graphene nanoribbons with a defined mixed edge-site sequence by surface assisted polymerization of (1,6)-dibromopyrene on Ag(110), Nanoscale. 8 (2016) 17843–17853. https://doi.org/10.1039/c6nr05952j.
[24] G. Franc, A. Gourdon, Covalent networks through on-surface chemistry in ultra-high vacuum: State-of-the-art and recent developments, Phys. Chem. Chem. Phys. 13 (2011) 14283–14292. https://doi.org/10.1039/c1cp20700h.
[25] S. Hla, L. Bartels, G. Meyer, K. Rieder, Inducing All Steps of a Chemical Reaction with the Scanning Tunneling Microscope Tip: Towards Single Molecule Engineering, Phys. Rev. Lett. 85 (2000) 2777–2780.
[26] A. Lafferentz, M. Wenderoth, S. Lounis, P. Zahn, N. Quaas, R.G. Ulbrich, P.H. Dederichs, S. Blugel, Conductance of a Single Conjugated Polymer as a Continuous Function of Its Length, Science (80-.). 323 (2009) 1190–1193. https://doi.org/10.1126/science.1168738.
[27] X. Zhou, G. Yu, Modified Engineering of Graphene Nanoribbons Prepared via On-Surface Synthesis, Adv. Mater. 32 (2020) 1–24. https://doi.org/10.1002/adma.201905957.
[28] J. Liu, B.W. Li, Y.Z. Tan, A. Giannakopoulos, C. Sanchez-Sanchez, D. Beljonne, P. Ruffieux, R. Fasel, X. Feng, K. Müllen, Toward Cove-Edged Low Band Gap Graphene Nanoribbons, J. Am. Chem. Soc. 137 (2015) 6097–6103. https://doi.org/10.1021/jacs.5b03017.
[29] Q. Fan, J.M. Gottfried, J. Zhu, Surface-Catalyzed C–C Covalent Coupling Strategies toward the Synthesis of Low-Dimensional Carbon-Based Nanostructures, Acc. Chem. Res. 48 (2015) 2484–2494. https://doi.org/10.1021/acs.accounts.5b00168.
[30] P. Ruffieux, S. Wang, B. Yang, C. Sanchez-Sanchez, J. Liu, T. Dienel, L. Talirz, P. Shinde, C.A. Pignedoli, D. Passerone, T. Dumslaff, X. Feng, K. Müllen, R. Fasel, On-surface synthesis of graphene nanoribbons with zigzag edge topology, Nature. 531 (2016) 489–492. https://doi.org/10.1038/nature17151.
[31] K.A. Simonov, N.A. Vinogradov, A.S. Vinogradov, A. V. Generalov, E.M. Zagrebina, N. Mårtensson, A.A. Cafolla, T. Carpy, J.P. Cunniffe, A.B. Preobrajenski, Effect of substrate chemistry on the bottom-up fabrication of graphene nanoribbons: Combined core-level spectroscopy and STM study, J. Phys. Chem. C. 118 (2014) 12532–12540. https://doi.org/10.1021/jp502215m.
[32] K.A. Simonov, N.A. Vinogradov, A.S. Vinogradov, A. V. Generalov, E.M. Zagrebina, G.I.

Svirskiy, A.A. Cafolla, T. Carpy, J.P. Cunniffe, T. Taketsugu, A. Lyalin, N. Mårtensson, A.B. Preobrajenski, From Graphene Nanoribbons on Cu(111) to Nanographene on Cu(110): Critical Role of Substrate Structure in the Bottom-Up Fabrication Strategy, ACS Nano. 9 (2015) 8997–9011. https://doi.org/10.1021/acsnano.5b03280.

[33] Y. Li, W. Zhang, M. Morgenstern, R. Mazzarello, Electronic and magnetic properties of zigzag graphene nanoribbons on the (111) surface of Cu, Ag, and Au, Phys. Rev. Lett. 110 (2013) 1–5. https://doi.org/10.1103/PhysRevLett.110.216804.

[34] P. Liljeroth, L. Yan, Engineered electronic states in atomically precise artificial lattices and graphene nanoribbons, Adv. Phys. X. 4 (2019). https://doi.org/10.1080/23746149.2019.1651672.

[35] M. Smerieri, I. Píš, L. Ferrighi, S. Nappini, A. Lusuan, L. Vattuone, L. Vaghi, A. Papagni, E. Magnano, C. Di Valentin, F. Bondino, L. Savio, Synthesis of corrugated C-based nanostructures by Br-corannulene oligomerization, Phys. Chem. Chem. Phys. 20 (2018) 26161–26172. https://doi.org/10.1039/c8cp04791j.

[36] I. Píš, L. Ferrighi, T.H. Nguyen, S. Nappini, L. Vaghi, A. Basagni, E. Magnano, A. Papagni, F. Sedona, C. Di Valentin, S. Agnoli, F. Bondino, Surface-Confined Polymerization of Halogenated Polyacenes: The Case of Dibromotetracene on Ag(110), J. Phys. Chem. C. 120 (2016) 4909–4918. https://doi.org/10.1021/acs.jpcc.5b12047.

[37] J.E. Barcelon, M. Smerieri, G. Carraro, P. Wojciechowski, L. Vattuone, M. Rocca, S. Nappini, I. Pis, E. Magnano, F. Bondino, L. Vaghi, A. Papagni, L. Savio, Morphological characterization and electronic properties of pristine and oxygen-exposed graphene nanoribbons on Ag(110), Phys. Chem. Chem. Phys. 23 (2021) 7926–7937.

[38] A. Berdonces-Layunta, J. Lawrence, S. Edalatmanesh, J. Castro-Esteban, T. Wang, M.S.G. Mohammed, L. Colazzo, D. Peña, P. Jelínek, D.G. De Oteyza, Chemical Stability of (3,1)-Chiral Graphene Nanoribbons, ACS Nano. 15 (2021) 5610–5617. https://doi.org/10.1021/acsnano.1c00695.

[39] G. Borin Barin, A. Fairbrother, L. Rotach, M. Bayle, M. Paillet, L. Liang, V. Meunier, R. Hauert, T. Dumslaff, A. Narita, K. Müllen, H. Sahabudeen, R. Berger, X. Feng, R. Fasel, P. Ruffieux, Surface-Synthesized Graphene Nanoribbons for Room Temperature Switching Devices: Substrate Transfer and ex Situ Characterization, ACS Appl. Nano Mater. 2 (2019) 2184–2192. https://doi.org/10.1021/acsanm.9b00151.

[40] A. Fairbrother, J.R. Sanchez-Valencia, B. Lauber, I. Shorubalko, P. Ruffieux, T. Hintermann, R. Fasel, High vacuum synthesis and ambient stability of bottom-up graphene nanoribbons, Nanoscale. 9 (2017) 2785–2792. https://doi.org/10.1039/c6nr08975e.

[41] S. Lee, Y.W. Lee, D.H. Kwak, J.Y. Lee, S.B. Han, J.I. Sohn, K.W. Park, Three-dimensional porous metal–nitrogen doped carbon nanostructure as a superior non-precious electrocatalyst in oxygen reduction reaction, J. Ind. Eng. Chem. 43 (2016) 170–176. https://doi.org/10.1016/j.jiec.2016.08.004.

[42] P. Sarkar, A. Hazra Chowdhury, S. Biswas, A. Khan, S.M. Islam, 2D covalent organic framework: a photoactive heterogeneous catalyst for chemical fixation of CO2 over propargyl amines in water under sunlight, Mater. Today Chem. 21 (2021) 100509. https://doi.org/10.1016/j.mtchem.2021.100509.

[43] M. Smerieri, I. Píš, L. Ferrighi, S. Nappini, A. Lusuan, L. Vattuone, L. Vaghi, A. Papagni, E. Magnano, C. Di Valentin, F. Bondino, L. Savio, Synthesis of corrugated C-based nanostructures by Br-corannulene oligomerization, Phys. Chem. Chem. Phys. 20 (2018) 26161–26172. https://doi.org/10.1039/c8cp04791j.

[44] G. Binnig, H. Rohrer, C. Gerber, E. Weibel, Surface Studies by Scanning Tunneling Microscopy, Phys. Rev. Lett. 49 (1982) 57–60.

[45] G. Binnig, H. Rohrer, C. Gerber, E. Weibel, Tunneling through a controllable vacuum gap, Appl. Phys. Lett. 40 (1982) 178–180. https://doi.org/10.1063/1.92999.

[46] G. Binnig, H. Rohrer, C. Gerber, E. Weibel, 7 x 7 Reconstruction on Si(111) Resolved in Real Space, Phys. Rev. Lett. 50 (1983) 120–123.
[47] B. Voigtländer, Scanning Probe Microscopy, Springer-Verlag, Berlin, 2016. https://doi.org/10.1016/B978-0-12-803224-4.00274-0.
[48] J. Bardeen, Tunneling from a many-particle point of view, Phys. Rev. Lett. 6 (1961) 57–59. https://doi.org/10.1103/PhysRev.131.1083.
[49] I. Horcas, R. Fernández, J.M. Gómez-Rodríguez, J. Colchero, J. Gómez-Herrero, A.M. Baro, WSXM: A software for scanning probe microscopy and a tool for nanotechnology, Rev. Sci. Instrum. 78 (2007). https://doi.org/10.1063/1.2432410.
[50] R. Costantini, M. Stredansky, D. Cvetko, G. Kladnik, A. Verdini, P. Sigalotti, F. Cilento, F. Salvador, A. De Luisa, D. Benedetti, L. Floreano, A. Morgante, A. Cossaro, M. Dell'Angela, ANCHOR-SUNDYN: A novel endstation for time resolved spectroscopy at the ALOISA beamline, J. Electron Spectros. Relat. Phenomena. 229 (2018) 7–12. https://doi.org/10.1016/j.elspec.2018.09.005.
[51] Joachim Stöhr, NEXAFS spectroscopy by Joachim Stöhr (z-lib, NEXAFS Spectrosc. 25 (1992) 114–161. https://doi.org/10.1007/978-3-662-02853-7.
[52] K. Lee, É.D. Murray, L. Kong, B.I. Lundqvist, D.C. Langreth, Higher-accuracy van der Waals density functional, Phys. Rev. B - Condens. Matter Mater. Phys. 82 (2010). https://doi.org/10.1103/PhysRevB.82.081101.
[53] I. Hamada, M. Otani, Comparative van der Waals density-functional study of graphene on metal surfaces, Phys. Rev. B - Condens. Matter Mater. Phys. 82 (2010) 1–4. https://doi.org/10.1103/PhysRevB.82.153412.
[54] I. Píš, L. Ferrighi, T.H. Nguyen, S. Nappini, L. Vaghi, A. Basagni, E. Magnano, A. Papagni, F. Sedona, C. Di Valentin, S. Agnoli, F. Bondino, Surface-Confined Polymerization of Halogenated Polyacenes: The Case of Dibromotetracene on Ag(110), J. Phys. Chem. C. 120 (2016) 4909–4918. https://doi.org/10.1021/acs.jpcc.5b12047.
[55] L. Ferrighi, I. Píš, T.H. Nguyen, M. Cattelan, S. Nappini, A. Basagni, M. Parravicini, A. Papagni, F. Sedona, E. Magnano, F. Bondino, C. Di Valentin, S. Agnoli, Control of the intermolecular coupling of dibromotetracene on Cu(110) by the sequential activation of C-Br and C-H bonds, Chem. - A Eur. J. 21 (2015) 5826–5834. https://doi.org/10.1002/chem.201405817.
[56] A. Basagni, L. Ferrighi, M. Cattelan, L. Nicolas, K. Handrup, L. Vaghi, A. Papagni, F. Sedona, C. Di Valentin, S. Agnoli, M. Sambi, On-surface photo-dissociation of C-Br bonds: Towards room temperature Ullmann coupling, Chem. Commun. 51 (2015) 12593–12596. https://doi.org/10.1039/c5cc04317d.
[57] J.D.P. Hendrik J. Monkhorst, Special points for Brillonin-zone integrations*, Phys. Rev. B. 13 (1976) 5188–5192. https://doi.org/doi:10.1103/physrevb.13.5188.
[58] D.R. Tersoff, J. and Hamann, Theory of the scanning tunneling microscope, Phys. Rev. B. 31 (1985) 805--813. https://doi.org/10.1103/PhysRevB.31.805.
[59] D. Nečas, P. Klapetek, Gwyddion: An open-source software for SPM data analysis, Cent. Eur. J. Phys. 10 (2012) 181–188. https://doi.org/10.2478/s11534-011-0096-2.
[60] G. Henkelman, B.P. Uberuaga, H. Jónsson, Climbing image nudged elastic band method for finding saddle points and minimum energy paths, J. Chem. Phys. 113 (2000) 9901–9904. https://doi.org/10.1063/1.1329672.
[61] B. Kim, Y. Park, J. Lee, D. Yokoyama, J.H. Lee, J. Kido, J. Park, Synthesis and electroluminescence properties of highly efficient blue fluorescence emitters using dual core chromophores, J. Mater. Chem. C. 1 (2013) 432–440. https://doi.org/10.1039/c2tc00185c.
[62] F.C. Henn, M.E. Bussell, C.T. Campbell, A simple means for reproducibly dosing low vapor pressure and/or reactive gases to surfaces in ultrahigh vacuum, J. Vac. Sci. Technol. A Vacuum, Surfaces, Film. 9 (1991) 10–13. https://doi.org/10.1116/1.577108.

[63] L. Savio, M. Smerieri, L. Vattuone, A. Gussoni, C. Tassistro, M. Rocca, STM study of hydroxyl formation at O/Ag (110), Phys. Rev. B - Condens. Matter Mater. Phys. 74 (2006) 1–6. https://doi.org/10.1103/PhysRevB.74.235412.
[64] L. Dong, P.N. Liu, N. Lin, Surface-Activated Coupling Reactions Confined on a Surface, Acc. Chem. Res. 48 (2015) 2765–2774. https://doi.org/10.1021/acs.accounts.5b00160.
[65] C. Riedl, C. Coletti, T. Iwasaki, A.A. Zakharov, U. Starke, Quasi-free-standing epitaxial graphene on SiC obtained by hydrogen intercalation, Phys. Rev. Lett. 103 (2009) 2–5. https://doi.org/10.1103/PhysRevLett.103.246804.
[66] S.L. Kovalenko, B. V. Andryushechkin, K.N. Eltsov, STM study of oxygen intercalation at the graphene/Ni(111) interface, Carbon N. Y. 164 (2020) 198–206. https://doi.org/10.1016/j.carbon.2020.03.054.
[67] T.B. Rawal, M. Smerieri, J. Pal, S. Hong, M. Alatalo, L. Savio, L. Vattuone, T.S. Rahman, M. Rocca, Deciphering complex features in STM images of O adatoms on Ag(110), Phys. Rev. B. 98 (2018) 35405. https://doi.org/10.1103/PhysRevB.98.035405.
[68] R. Larciprete, S. Ulstrup, P. Lacovig, M. Dalmiglio, M. Bianchi, F. Mazzola, L. Hornekær, F. Orlando, A. Baraldi, P. Hofmann, S. Lizzit, Oxygen switching of the epitaxial graphene-metal interaction, ACS Nano. 6 (2012) 9551–9558. https://doi.org/10.1021/nn302729j.
[69] R. Blume, P.R. Kidambi, B.C. Bayer, R.S. Weatherup, Z.J. Wang, G. Weinberg, M.G. Willinger, M. Greiner, S. Hofmann, A. Knop-Gericke, R. Schlögl, The influence of intercalated oxygen on the properties of graphene on polycrystalline Cu under various environmental conditions, Phys. Chem. Chem. Phys. 16 (2014) 25989–26003. https://doi.org/10.1039/c4cp04025b.
[70] P. Sutter, P. Albrecht, X. Tong, E. Sutter, Mechanical Decoupling of Graphene from Ru(0001) by Interfacial Reaction with Oxygen, J. Phys. Chem. C. 117 (2013) 6320–6324. https://doi.org/10.1055/sos-sd-032-00583.
[71] L. Vattuone, M. Rocca, C. Boragno, U. Valbusa, Initial sticking coefficient of O2 on Ag(110), J. Chem. Phys. 101 (1994) 713–725. https://doi.org/10.1063/1.468127.
[72] Y.C.G. Kwan, G.M. Ng, C.H.A. Huan, Identification of functional groups and determination of carboxyl formation temperature in graphene oxide using the XPS O 1s spectrum, Thin Solid Films. 590 (2015) 40–48. https://doi.org/10.1016/j.tsf.2015.07.051.
[73] A. Ganguly, S. Sharma, P. Papakonstantinou, J. Hamilton, Probing the thermal deoxygenation of graphene oxide using high-resolution in situ X-ray-based spectroscopies, J. Phys. Chem. C. 115 (2011) 17009–17019. https://doi.org/10.1021/jp203741y.
[74] U. Zielke, K.J. Hüttinger, W.P. Hoffman, Surface-oxidized carbon fibers: I. Surface structure and chemistry, Carbon N. Y. 34 (1996) 983–998. https://doi.org/10.1016/0008-6223(96)00032-2.
[75] J. Matthew, Surface analysis by Auger and x-ray photoelectron spectroscopy. D. Briggs and J. T. Grant (eds). IMPublications, Chichester, UK and SurfaceSpectra, Manchester, UK, 2003. 900 pp., ISBN 1-901019-04-7, 900 pp, Surf. Interface Anal. 36 (2004) 1647. https://doi.org/10.1002/sia.2005.
[76] J. Eichhorn, D. Nieckarz, O. Ochs, D. Samanta, M. Schmittel, P.J. Szabelski, M. Lackinger, On-surface ullmann coupling: The influence of kinetic reaction parameters on the morphology and quality of covalent networks, ACS Nano. 8 (2014) 7880–7889. https://doi.org/10.1021/nn501567p.
[77] R. Gutzler, L. Cardenas, J. Lipton-Duffin, M. El Garah, L.E. Dinca, C.E. Szakacs, C. Fu, M. Gallagher, M. Vondráček, M. Rybachuk, D.F. Perepichka, F. Rosei, Ullmann-type coupling of brominated tetrathienoanthracene on copper and silver, Nanoscale. 6 (2014) 2660–2668. https://doi.org/10.1039/c3nr05710k.
[78] G.M. National Institute of Standards and Technology, NIST X-ray Photoelectron Spectroscopy Database, (2000). https://doi.org/doi:10.18434/T4T88K.

[79] Y. Zubavichus, M. Zharnikov, Y. Yang, O. Fuchs, E. Umbach, C. Heske, A. Ulman, M. Grunze, X-ray photoelectron spectroscopy and near-edge X-ray absorption fine structure study of water adsorption on pyridine-terminated thiolate self-assembled monolayers, Langmuir. 20 (2004) 11022–11029. https://doi.org/10.1021/la047980b.
[80] F. Orlando, P. Lacovig, M. Dalmiglio, A. Baraldi, R. Larciprete, S. Lizzit, Synthesis of nitrogen-doped epitaxial graphene via plasma-assisted method: Role of the graphene-substrate interaction, Surf. Sci. 643 (2016) 214–221. https://doi.org/10.1016/j.susc.2015.06.017.
[81] R.H. Temperton, A.J. Gibson, K. Handrup, J.N. O'Shea, Adsorption and charge transfer interactions of bi-isonicotinic acid on Ag(111), J. Chem. Phys. 147 (2017). https://doi.org/10.1063/1.4996746.
[82] R. Costantini, H. Ustunel, Z. Feng, M. Stredansky, D. Toffoli, G. Fronzoni, C. Dri, G. Comelli, D. Cvetko, G. Kladnik, G. Bavdek, L. Floreano, A. Morgante, A. Cossaro, Methylamine terminated molecules on Ni(1 1 1): A path to low temperature synthesis of nitrogen-doped graphene, FlatChem. 24 (2020) 100205. https://doi.org/10.1016/j.flatc.2020.100205.
[83] M. Bowker, K.C. Waugh, Chlorine adsorption and chloridation of Ag(110), Surf. Sci. 155 (1985) 1–14. https://doi.org/10.1016/0039-6028(85)90399-1.
[84] M. Stojkovska, D. Perilli, J.E. Barcelon, M. Smerieri, G. Carraro, T.H. Dinh, L. Vattuone, M.A. Rocca, G. Bracco, M. Dell'Angela, R. Costantini, A. Cossaro, L. Vaghi, A. Papagni, C. Di Valentin, L. Savio, Well-Ordered Surface Metal Atoms Complexation by Deposition of Pd Cyclometallated Compounds on Ag (110), Appl. Surf. Sci. 606 (2022). https://doi.org/10.2139/ssrn.4158267.
[85] M. Di Giovannantonio, M. El Garah, J. Lipton-Duffin, V. Meunier, L. Cardenas, Y. Fagot Revurat, A. Cossaro, A. Verdini, D.F. Perepichka, F. Rosei, G. Contini, Insight into organometallic intermediate and its evolution to covalent bonding in surface-confined ullmann polymerization, ACS Nano. 7 (2013) 8190–8198. https://doi.org/10.1021/nn4035684.
[86] C. Kolczewski, R. Püttner, O. Plashkevych, H. Ågren, V. Staemmler, M. Martins, G. Snell, A.S. Schlachter, M. Sant'Anna, G. Kaindl, L.G.M. Pettersson, Detailed study of pyridine at the C 1s and N 1s ionization thresholds: The influence of the vibrational fine structure, J. Chem. Phys. 115 (2001) 6426–6437. https://doi.org/10.1063/1.1397797.
[87] O. Adak, G. Kladnik, G. Bavdek, A. Cossaro, A. Morgante, D. Cvetko, L. Venkataraman, Ultrafast Bidirectional Charge Transport and Electron Decoherence at Molecule/Surface Interfaces: A Comparison of Gold, Graphene, and Graphene Nanoribbon Surfaces, Nano Lett. 15 (2015) 8316–8321. https://doi.org/10.1021/acs.nanolett.5b03962.
[88] C.M. Doyle, J.P. Cunniffe, S.A. Krasnikov, A.B. Preobrajenski, Z. Li, N.N. Sergeeva, M.O. Senge, A.A. Cafolla, Ni-Cu ion exchange observed for Ni(II)-porphyrins on Cu(111), Chem. Commun. 50 (2014) 3447–3449. https://doi.org/10.1039/c3cc48913b.
[89] K. Shen, B. Narsu, G. Ji, H. Sun, J. Hu, Z. Liang, X. Gao, H. Li, Z. Li, B. Song, Z. Jiang, H. Huang, J.W. Wells, F. Song, On-surface manipulation of atom substitution between cobalt phthalocyanine and the Cu(111) substrate, RSC Adv. 7 (2017) 13827–13835. https://doi.org/10.1039/c7ra00636e.
[90] F.R. de Boer, R. Boom, W.C.M. Mattens, A.R. Miedema, A.K. Niessen, Cohesion in Metals, Amsterdam, 1988.
[91] F. Baletto, C. Mottet, R. Ferrando, Growth of Three-Shell Onionlike Bimetallic Nanoparticles, Phys. Rev. Lett. 90 (2003) 4. https://doi.org/10.1103/PhysRevLett.90.135504.
[92] W. Xiaoyong, G. Zijian, Targeting and delivery of platinum-based anticancer drugs, Chem. Soc. Rev. 42 (2013) 202–224. https://doi.org/10.1039/c2cs35259a.
[93] M. Inagaki, M. Toyoda, Y. Soneda, T. Morishita, Nitrogen-doped carbon materials, Carbon N. Y. 132 (2018) 104–140. https://doi.org/10.1016/j.carbon.2018.02.024.
[94] M. Abyazisani, J.M. MacLeod, J. Lipton-Duffin, Cleaning up after the Party: Removing the

Byproducts of On-Surface Ullmann Coupling, ACS Nano. 13 (2019) 9270–9278. https://doi.org/10.1021/acsnano.9b03812.
[95] C. Bronner, J. Björk, P. Tegeder, Tracking and removing br during the on-surface synthesis of a graphene nanoribbon, J. Phys. Chem. C. 119 (2015) 486–493. https://doi.org/10.1021/jp5106218.
[96] B. V. Andryushechkin, T. V. Pavlova, K.N. Eltsov, Adsorption of halogens on metal surfaces, Surf. Sci. Rep. 73 (2018) 83–115. https://doi.org/10.1016/j.surfrep.2018.03.001.
[97] C. Benndorf, B. Kruger, Adsorption and reaction of bromine with Ag(110), Surf. Sci. 151 (1985) 271–288.
[98] G. Bracco, A.C. Levi, Roughening Transition: Theories and Experiments, in: M. Rocca, T.S. Rhaman, L. Vattuone (Eds.), Springer Handb. Surf. Sci., Springer series in surface sciences, 2020: pp. 3–44. https://doi.org/https://doi.org/10.1007/978-3-030-46906-1.
[99] T. Zambelli, J. Barth, J. Wintterlin, Formation mechanism of the O-induced added-row reconstruction on Ag(110): A low-temperature STM study, Phys. Rev. B - Condens. Matter Mater. Phys. 58 (1998) 12663–12666. https://doi.org/10.1103/PhysRevB.58.12663.
[100] B.E. Hayden, K.C. Prince, P.J. Davie, G. Paolucci, A.M. Bradshaw, Alkali metal-induced reconstruction of Ag(110), Solid State Commun. 48 (1983) 325–328. https://doi.org/10.1016/0038-1098(83)90732-9.
[101] R. Bernard, T. Leoni, A. Wilson, T. Lelaidier, H. Sahaf, E. Moyen, L. Assaud, L. Santinacci, F. Leroy, F. Cheynis, A. Ranguis, H. Jamgotchian, C. Becker, Y. Borensztein, M. Hanbücken, G. Prévot, L. Masson, Growth of Si ultrathin films on silver surfaces: Evidence of an Ag(110) reconstruction induced by Si, Phys. Rev. B - Condens. Matter Mater. Phys. 88 (2013) 2–6. https://doi.org/10.1103/PhysRevB.88.121411.
[102] J.E. Barcelon, M. Stojkovska, D. Perilli, G. Carraro, M. Smerieri, L. Vattuone, M. Rocca, G. Bracco, M. Dell'Angela, R. Costantini, A. Cossaro, L. Vaghi, A. Papagni, C. Di Valentin, L. Savio, Formation of diphenyl-bipyridine units by surface assisted cross coupling in Pd-cyclometalled complexes, Appl. Surf. Sci. 609 (2023) 155307.
[103] D.G. De Oteyza, A. García-Lekue, M. Vilas-Varela, N. Merino-Díez, E. Carbonell-Sanromà, M. Corso, G. Vasseur, C. Rogero, E. Guitián, J.I. Pascual, J.E. Ortega, Y. Wakayama, D. Peña, Substrate-Independent Growth of Atomically Precise Chiral Graphene Nanoribbons, ACS Nano. 10 (2016) 9000–9008. https://doi.org/10.1021/acsnano.6b05269.
[104] N. Merino-Díez, J. Li, A. Garcia-Lekue, G. Vasseur, M. Vilas-Varela, E. Carbonell-Sanromà, M. Corso, J.E. Ortega, D. Peña, J.I. Pascual, D.G. De Oteyza, Unraveling the Electronic Structure of Narrow Atomically Precise Chiral Graphene Nanoribbons, J. Phys. Chem. Lett. 9 (2018) 25–30. https://doi.org/10.1021/acs.jpclett.7b02767.
[105] J. Lawrence, A. Berdonces-Layunta, S. Edalatmanesh, J. Castro-Esteban, T. Wang, A. Jimenez-Martin, B. de la Torre, R. Castrillo-Bodero, P. Angulo-Portugal, M.S.G. Mohammed, A. Matěj, M. Vilas-Varela, F. Schiller, M. Corso, P. Jelinek, D. Peña, D.G. de Oteyza, Circumventing the stability problems of graphene nanoribbon zigzag edges, Nat. Chem. (2022). https://doi.org/10.1038/s41557-022-01042-8.